MOLECULAR SCALE INTERACTIONS BETWEEN HYDRATED CEMENT PHASES AND
RADIONUCLIDES USING MOLECULAR DYNAMICS MODELING

By

Jingjing Bu

Dissertation

Submitted to the Faculty of the

Graduate School of Vanderbilt University

in partial fulfillment of the requirements

for the degree of

DOCTOR OF PHILOSOPHY

in

Environmental Engineering

May 11, 2018

Nashville, Tennessee

Approved:

Kevin G. Brown, Ph.D

James H. Clarke, Ph.D

David S. Kosson, Ph.D

Florence Sanchez, Ph.D

Hans A. van der Sloot, Ph.D

ACKNOWLEDGEMENTS

I would like to thank my committee members, Dr. Kevin G. Brown, Dr. James H. Clarke, Dr. David S. Kosson, Dr. Hans A. van der Sloot for their time and valuable suggestions. I would like to especially thank my advisor and committee chair, Dr. Florence Sanchez, for her advice and encouragement during my Ph.D. career and in other areas of life as well. She gave me the confidence to raise a family while pursuing my Ph.D. and career goals. I am also deeply grateful for the friendships I have formed during my time at Vanderbilt with fellow graduate students and staff, including too many to name.

TABLE OF CONTENTS

LIST OF FIGURES

LIST OF TABLES

NOMENCLATURE

Abbreviation/Symbol	Description
β-C_2S	β-dicalcium silicate
ε	Permittivity
θ	Bond angle
σ	Charge density
ψ	Electrostatic potential
$(CaO)_{0.83}\,(SiO_2)_1\cdot(H_2O)_{1.3}$	14Å tobermorite
$(CaO)_{1.67}(SiO_2)_1\cdot(H_2O)_{2.1}$	Jennite
$[SiO_2(OH)_2]^{2-}$	Monomeric silicate anion
A	Area of overlap of two plates
AFm	Alumino-ferrite-mono
ANSI/ANS	American National Standards Institute/American National Standards
B	Bridging tetrahedron
BFS	Blast furnace slag
C	Capacitance
C/S	Calcium oxide/silicate ratio
$C_2SH(II)$	Calcium silicate hydrate type 2
C_3S	Tricalcium silicate
$Ca[SiO_2(OH)_2][Ca(OH)_2]_x[H_2O]_y$	Hydrated calcium silicates
$Ca_5Si_6O_{16}(OH)_2\cdot7H_2O$	14Å tobermorite
CaO-Al2O3-SiO2	Calcium oxide-aluminate-silicate
C-A-S-H	Stratlingite
ClayFF	Clay forcefield
CN	Coordination number
CsCl	Cesium chloride
C-S-H	Calcium silicate hydrate

CSH(I)	Calcium silicate hydrate type 1
d	Separation between the plates
D	Dipole moment
D_{eff}	Effective diffusion coefficient
DFT	Density function theory
EDL	Electrical double layer
H/S	Water/silicate ratio
IR	Infrared radiation
k_1, k_2	Force constant
K_d	Distribution coefficient
KTcO4	Potassium pertechnetate
LI	Leachability index
MD	Molecular dynamics
M-S-H	Magnesium-Silicate-Hydrate
MSD	Mean square displacement
NEA	National education association
NHL	Nosé-Hoover-Langevin
NMR	Nuclear magnetic resonance
NPT	Isothermal-isobaric ensemble
NVT	Canonical ensemble
Ob	Bridging oxygen
Obts	Bridging oxygen with tetrahedral substitution
Oh	Hydroxyl oxygen
Otc	Pertechnetate oxygen
P	Paired tetrahedra
PBC	Periodic boundary condition
PC	Portland cement
q	Partial charge
RDF	Radial distribution function

RMSD	Root mean square deviation
RMSF	Root mean square fluctuations
SAMMS	Self-assembled monolayers on mesoporous supports
TLM	Triple layer model
vdW	van der Waals
XRD	X-ray diffraction

CHAPTER 1

1 Introduction

1.1 Overview

Cementitious materials are regarded as good candidates for the encapsulation and immobilization of nuclear wastes. They have been used as encapsulation matrices for the geological disposal of intermediate level radioactive wastes at nuclear fuel reprocessing plants in many countries [1]. Nuclear wastes are by-products of various activities (*e.g.*, military, nuclear power generation, medicine) that contain a variety of radionuclides such as, cesium-137 (^{137}Cs), iodine-129 (^{129}I), plutonium-241 (^{241}Pu), strontium-90 (^{90}Sr), and technetium-99 (^{99}Tc) [2]. ^{137}Cs and ^{99}Tc alone represent about 13% of fission product yield in nuclear wastes [3]. ^{137}Cs is a high radiation fission product with β and γ emissions [4], and ^{99}Tc is a β-emission fission product with a long half-life (211,000 years) [5]; both radionuclides present significant problems for nuclear waste management.

Several physical and chemical interaction mechanisms between radionuclides and cementitious materials have been reported in the literature [6,7]: (i) precipitation as simple salts in the pores of the cement matrix; (ii) formation of complexes and colloids in the aqueous pore water solution; (iii) lattice incorporation in the major cement hydration products; and (iv) sorption at cement hydrate surfaces (*i.e.* physical and chemical adsorption). The specific mechanisms of immobilization, however, depend on the radionuclide type, concentration of radionuclides, and binding capacity of the cement phases. While experimental studies have been performed to investigate radionuclide ion interaction mechanisms and cement matrix uptake potential [8,9], the fundamental mechanisms of interaction of radionuclides with the cement phases remain not well understood. At the molecular scale, current experimental techniques are challenged by various limiting factors, including instrument resolution [10,11]. Particularly, the interaction mechanisms of ^{137}Cs and ^{99}Tc with important cement phases, including crystalline C-S-H phases and ettringite, have only been addressed by a few studies [12,13]. A fundamental understanding of the adsorption mechanisms of radionuclides on different cement phases is thus important to evaluate the immobilization processes of ^{137}Cs and ^{99}Tc to cement phases and to design cement waste forms with better performance.

Hypothesis: *The chemical performance of cement waste forms is related to the chemical composition of cementitious materials. Different hydrated cement phases are expected to provide different adsorption capacities for radionuclides. It is hypothesized that calcium-silicate-hydrate (C-S-H) and calcium aluminate phases (e.g., ettringite), two main products of Portland Cement (PC) hydration, play a critical role in the immobilization of cesium and technetium through adsorption.*

1.2   Objectives and Approach

The overall objective of the research was to develop a fundamental understanding on an atomic-scale level of the interaction mechanisms of Cs^+ and TcO_4^- ions with Calcium-Silicate-Hydrate (C-S-H) and calcium-aluminate-sulfate hydrate (*i.e.* ettringite), two main products of cement hydration. Three crystalline structures were used as mineral analogs for C-S-H: tobermorite 9Å, tobermorite 14Å, and jennite. This work is significant both because the topics have not been studied in detail and because of the depth at which this work will look into the interaction mechanisms.

To date, interactions between Cs^+ ions and cement pastes have been mainly investigated by experimental methods [14–18]. Although it has been agreed that C-S-H plays an important role in the adsorption of Cs^+ ions on cement paste, the mechanisms of interaction and adsorption onto the different cement phases are not yet fully understood. A variety of interaction mechanisms have been suggested in the literature [19–21], and studies concerning the Cs retention capacity of PC paste have indicated conflicting or different results [22–26]. Studies concerning the interactions between Cs^+ ions and C-S-H phases have indicated that the interaction mechanisms depend on the type of ions, as well as the properties of the solid phases [12,27]. The adsorption capacity of different cementitious materials for ^{137}Cs, with respect to K_d, ranged from 0.1 to 34,000 mL/g. The estimated K_d values for C-S-H ranged from 7 to 6,900 mL/g [14,28]. The large variation of K_d values for ^{137}Cs on the hydrated cement were influenced by the chemical composition of the cementitious materials, the chemical composition of the solution (*i.e.* the initial concentration of [99]Cs in the solution, the type of the contact solution and the pH of the system), and the equilibration time [14,28]. In addition, most research concerning ^{99}Tc immobilization by cementitious materials has been focused on the interaction between less mobile Tc(IV) (Tc^{4+}) ions and cementitious materials in reducing environments [29,30]. Only a few researchers have studied the interaction

between pertechnetate (TcO$_4^-$) ions and cement pastes [31,32]. The adsorption capacity of different cementitious materials for ^{99}Tc, with respect to K_d, ranged from 0.7 mL/g for Tc(VII) to 6,000 mL/g for Tc(IV) [28,33,34]. Cementitious materials showed lower adsorption capacity of ^{99}Tc under oxidizing conditions, and the valence state of ^{99}Tc was a key parameter of its sorption behavior on cementitious materials. The fundamental interaction mechanisms between Cs$^+$, TcO$_4^-$ ions, and cement phases need to be investigated systematically at an atomic level, so that knowledge can be provided to design waste forms with better performance.

Molecular dynamic simulation has been widely used to investigate the interaction mechanisms between a variety of ions and cement phases, or clay minerals. Results have indicated that tobermorites and jennite were capable of adsorbing ions such as Na$^+$, K$^+$ and Sr^{2+} [35–37]. Cs$^+$ ions can be adsorbed on the surfaces of some clay minerals as inner-sphere and outer-sphere complexes [38–43]. Although a classic forcefield for TcO$_4^-$ ions has been developed, calculations have only been performed to investigate the hydration energy and aqueous interaction between TcO$_4^-$ ions with other ions [44]. Little to no research exists on the interfacial interaction between TcO$_4^-$ ions and cement phases. The three specific objectives addressed in this dissertation are:

1. Develop a framework for evaluating the adsorption mechanisms of radionuclides onto cement phases. This framework includes monitoring convergence of the simulations to equilibrium and developing a data analysis methodology.
2. Investigate the adsorption mechanisms, including interaction energy and structural and dynamical properties of Cs$^+$ ions on the surfaces of 9Å tobermorite, 14Å tobermorite, and jennite.
3. Investigate the adsorption mechanisms, including interaction energy and structural and dynamical properties of TcO$_4^-$ ions on the surfaces of 14Å tobermorite, jennite, and ettringite.

MD simulations were used to investigate the fundamental interaction mechanisms of Cs$^+$ ions (*i.e.* 0.5M CsCl) with 9Å tobermorite, 14Å tobermorite, and jennite and the interaction mechanisms of TcO$_4^-$ ions (*i.e.* 0.2M KTcO$_4$) with 14Å tobermorite, jennite, and ettringite. Although the concentrations of radionuclides in nuclear waste tanks (0.00002 to 0.00019M for Cs$^+$ [45] and 0.00005M for TcO$_4^-$ [46]) are higher than those used in the present research, chemical interactions

are not involved in MD simulations; therefore, the interaction mechanisms between radionuclides and cement phases were not affected by the concentration of radionuclides in the models. The atomic-scale energetic, structural, and dynamic properties of the interface between the aqueous solution containing Cs^+ ions or TcO_4^- ions and the cement phases were analyzed by using relative atomic density profiles, radial distribution function (RDF), coordination number (CN), atomic density contour maps, diffusion coefficient, adsorption energy and hydration energy, and local structure analysis.

1.3   Structure of the Dissertation

This dissertation is organized into six chapters. Chapter 2 contains a review of relevant literature pertaining to the research in this dissertation. Chapter 3 discusses the methodology used for evaluating the adsorption mechanisms of Cs^+ ions and TcO_4^- ions onto cement phases using MD simulations, including evaluation of the convergence of the simulations to equilibrium and the data analysis methodology used, in particular the determination of the location of the inner-sphere and outer-sphere regions. Chapter 4 discusses the interaction mechanisms of Cs^+ ions with the basal surfaces of 9Å tobermorite, 14Å tobermorite, and jennite. Chapter 5 discusses the interaction mechanisms of TcO_4^- ions with the basal surfaces of 14Å tobermorite, jennite, and ettringite. Chapter 6 summarizes the results and presents recommendation for future work.

CHAPTER 2

2 Background

2.1 ^{137}Cs and ^{99}Tc

^{137}Cs, among the many radioactive fission products, has drawn special attention because of its unique physical and chemical properties. It is commonly produced through nuclear fission of uranium-235 (^{235}U) and other fissionable isotopes in nuclear reactors and nuclear weapons testing [47]. ^{137}Cs has a half-life of 30.17 years [48]. Most ^{137}Cs first decays to a metastable nuclear isomer of barium, barium-137m (^{137m}Ba), through beta emission. This then decays through γ emission to stable barium-137 (^{137}Ba) [49]. ^{137}Cs is highly soluble in water, and it efficiently travels through the air. ^{137}Cs binds strongly to soil and concrete, and plants growing in or nearby contaminated soil can readily take up ^{137}Cs [47]. ^{137}Cs is not typically found in the environment in large quantities; significant ^{137}Cs contamination often results from mishandling of an industrial source of ^{137}Cs, a nuclear detonation, or a major nuclear accident [47]. While it is used in medical devices and industrial gauges [47], external and internal exposure to ^{137}Cs in humans can cause a variety of adverse health effects, including dermal injuries, radiation sickness and even death, depending on the radiation dose [50].

^{99}Tc naturally occurs in the earth's crust in very small amounts, and most of ^{99}Tc is produced through nuclear fission [51]. ^{99}Tc is a key radionuclide in spent nuclear fuel (SNF) and high-level waste (HLW) [52]. ^{99}Tc is also a byproduct of nuclear weapons explosions [51]. The half-life of ^{99}Tc is 210,000 years [52]. A short-lived form of ^{99}Tc (with a half-life of 6 hours), technetium-99m (^{99m}Tc), is also a component of nuclear reactor gaseous and liquid effluent. ^{99m}Tc is can be found as a component of industrial and medical wastes, and it is used as a medical diagnostic tool [51]. The environment naturally contains very low concentrations of ^{99}Tc, although some plants and aquatic life can concentrate ^{99}Tc and fix mobile ^{99}Tc into less mobile ^{99}Tc organics, oxides, and sulfides [53–55]. Exposure to ^{99}Tc from the environment under normal circumstances is unlikely. However, higher concentrations of ^{99}Tc may be found close to contaminated facilities, including federal weapons facilities and nuclear fuel cycle facilities [51], which may increase the probability of exposure. Once in the human body, ^{99}Tc is readily transferred to the bloodstream and concentrates in in soft tissues. As with any other radioactive

material, exposure to radiation can result in cancer or other adverse health effects [51]. However, the body constantly excretes ^{99}Tc once it is ingested [51].

2.2   Cementitious Materials and the Hydrated Phases

The chemical composition of cementitious materials can be represented on the $CaO-Al_2O_3-SiO_2$ ternary diagram [56]. PCs are generally characterized by higher calcium content and lower silica and aluminum content than supplementary cementitious materials, with exception of fine limestone [56]. The silica-to-alumina and silica-to-calcium weight ratios in supplementary cementitious materials can be extended to 2, which is higher than those in PC [56–58].

Due to the wide range of chemical composition of cementitious materials, different hydrate phases are generated during the hydration process (Figure 2.1) [56]. The large field of compositions of the C-S-H phase in the hydrated $CaO-Al_2O_3-SiO_2$ ternary diagram indicates that C-S-H is the most important phase in cement paste. Cement paste generated by blending of PC with supplementary cementitious materials will lead to the formation of C-S-H with a lower CaO/SiO_2 (C/S) ratio, and the formation of other cement phases, such as alumino-ferrite-monosulfate (AFm). Because the limits of the hydrate phases possibly generated are not well known, especially with respect to the amount of alumina which can be incorporated, the boundaries shown in Figure 2.1 are only an approximation [56].
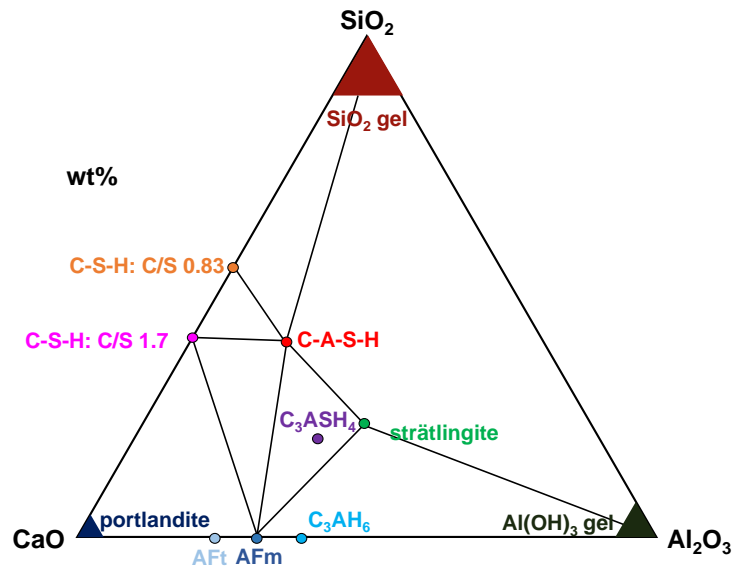
Figure 2.1. Hydrated phases in the $CaO-Al_2O_3-SiO_2$ system (adapted from [56]).

2.2.1   Crystalline Calcium Silicate Hydrates (C-S-H)

C-S-H phases are the most abundant phases in PC paste [59–62]. C-S-H phases are formed by the hydration of tricalcium silicate (C_3S) or β-dicalcium silicate (β-C_2S), which together constitute about 75% of a PC paste by weight [63]. The structure of C-S-H has been widely studied but is still poorly understood, because it has a wide range of chemical compositions [64–67]. Single phase C-S-H has C/S ratios of 0.41-1.85 [65]. The C/S ratios of C-S-H in PC paste are in the range of 1.2 to 2.1 [68]. In most cases, the C/S ratio is near 1.7 [59,68]. If a paste contains supplementary cementitious materials such as silica fume, fly ash, and ground granulated blast-furnace slag, the mean value of the C/S ratio is much reduced, to less than 1 in some cases [68]. The molar H_2O/SiO_2 (H/S) ratios are in the range of 0.5-2.5 [69], and these values are influenced by the mechanism of C-S-H formation [59].

Given the fact that concrete is the most widely used building material in the world, the structural and mechanical properties of cement paste have been intensively studied, and various models have been proposed for the nanostructure of C-S-H gel. Two categories of models have been proposed: one category included monomer-based models, where the silicate anions were entirely monomeric; the other category included dreierkette-based models, which were primarily derived from the structure of 14Å tobermorite (and a variety of other minerals) [70].

Monomer-based models were suggested by some researchers during the 1950s and 1960s, when people first began developing models for C-S-H [71]. Bernal [71] studied a series of cement types and suggested that a greater part of the hydrated phases includes monomeric silicate anion $[SiO_2(OH)_2]^{2-}$. Two hydrated calcium silicates, with the general formula $Ca[SiO_2(OH)_2][Ca(OH)_2]_x[H_2O]_y$ were proposed, where x is between 0 and 0.5 for CSH(I) and held at 1 for $C_2SH(II)$. However, while monomeric hydrated silicate species were the only observed species during the induction period of hydrating cement, monomer-based models were not consistent with the experimentally observed distribution of linear silicate chains for the C-S-H that formed afterwards [66].

Linear silicate chain structures for the C-S-H have been more widely accepted, and a variety of dreierkette-based models have been proposed since the 1950s [71–73]. In dreierkette-based structures, silicate tetrahedra are coordinated to the central Ca-O sheet on both sides and repeat every three units in linear kinked chains. Two of the three tetrahedra, which share O-O

7

edges with the Ca-O part of the central layer, are referred to as 'paired' tetrahedra (P). The third tetrahedron, which shares an O atom at the pyramidal apex of a CaO_x polyhedron and connects the two paired tetrahedra, is referred as a 'bridging' tetrahedron (B) [70].

Most of dreierkette-based models include tobermorite-like structures; however, the C/S ratio in an intact 14Å tobermorite structure is 0.83 [72], which is lower than the value observed experimentally in C_3S or neat PC pastes, *i.e.*, 1.7–1.8 [68]. This issue was addressed in dreierkette-based models by incorporating defective silicate chains: some of the bridging tetrahedra are replaced by interlayer Ca^{2+} ions so that the C/S ratio was raised above 0.83. Two categories of dreierkette-based models were proposed based on this method of raising the C/S ratio: the first category is characterized by tobermorite-like structures interstratified with layers of calcium hydroxide [74,75]; the second category is characterized by tobermorite-like structures intermixed with those of a jennite-like structure [61].

A classic dreierkette-based model of C-S-H is Taylor's 1986 model that classified C-S-H into C-S-H(I) and C-S-H(II) [61]. The former is structurally similar to 14Å tobermorite, and the latter is structurally similar to jennite [61]. This C-S-H system is described by an ideal solid solution with hybrids jennite $(CaO)_{1.67}(SiO_2)_1 \cdot (H_2O)_{2.1}$ and 14Å tobermorite $(CaO)_{0.83}$ $(SiO_2)_1 \cdot (H_2O)_{1.3}$. Although C-S-H gel is amorphous, at the nanoscale it presents a short range ordered structure [76]. A sequence of finite silicate chains containing up to 3n-1 tetrahedra (where n= 1, 2, 3, …) is generated by removing bridging tetrahedra intermediated between none (infinite length chains) and all (dimers) [70]. This finite chain structure is consistent with the silicate chain structure observed in hardened C_3S and PC pastes [68,70]. The length of silicate chains for C-S-H in PCs vary from 2 in young pastes to about 5 in mature pastes. The silicate chains with length of 20 or greater can be found in blended cement pastes cured at high temperatures [70,77].

The crystalline structure of 14Å tobermorite $(Ca_5Si_6O_{16}(OH)_2 \cdot 7H_2O)$ is built up of complex layers [78] (Figure 2.2). In each layer, seven-fold coordinated calcium cations form a central CaO_2 sheet on both sides with dreierketten arrangement (*i.e.* silicate chains with periodicity of three tetrahedra). The distance between two CaO_2 sheets is 14Å. The interlayer spaces between two complex layers are occupied by calcium cations and water molecules [70,78].

Jennite ($Ca_9Si_6O_{18}(OH)_8 \cdot 8H_2O$) (Figure 2.3) is another crystalline C-S-H that has dreierkette silicate chains with a much higher C/S ratio (C/S ratio of 1.5) [79]. Jennite has a similar structure to tobermorite; the main difference is that about half of the oxygen sites on the CaO polyhedra sheets are not linked to silicate chains but to OH^- groups [79].

Beyond the 14Å tobermorite and jennite discussed in Taylor's model, 9Å tobermorite [80] has also been widely accepted as a useful model to study amorphous C-S-H gel [13]. 9Å tobermorite has a similar crystalline structure to 14Å tobermorite, but with two main differences: the basal space between two complex layers is 9Å, and it does not contain interlayer water molecules.
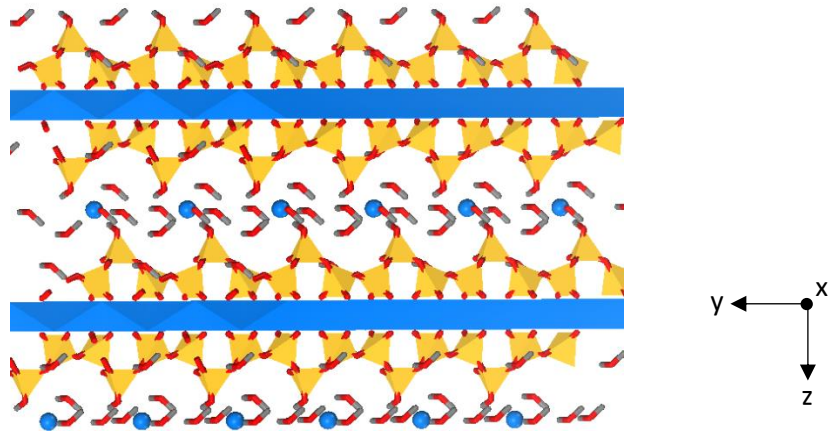
Figure 2.2. Schematic diagram showing dreierkette chains present in 14Å tobermorite along (1 0 0) as described in [78]. Blue balls and octahedra – Ca; yellow tetrahedral – Si; grey lines – H; red lines – O.
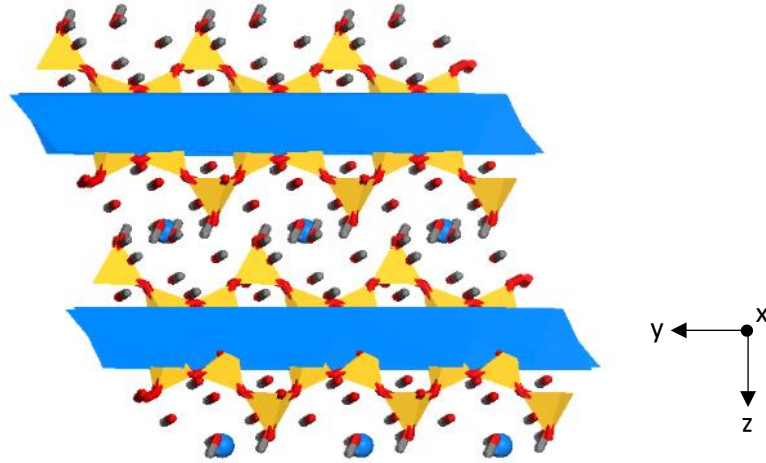
Figure 2.3. A projection of the jennite crystalline structure as viewed along (1 0 0) as described in [79]. Blue balls and octahedra – Ca; yellow tetrahedral – Si; grey lines – H; red lines – O.

2.2.2 *Calcium-aluminate-sulfate Hydrate (Ettringite)*

Ettringite $(Ca_6[Al(OH)_6]_2(SO_4)_3 \cdot \sim 26H_2O)$ represents ~10% of weight at the early hydration stage of PC paste [81] and is also of interest because the formation of ettringite can cause expansion and cracking, eventually affecting the durability of cement paste [82]. Ettringite can be found at the early hydration stages of PC [19]. Ettringite in cement is formed mainly through two interactions: (1) gypsum and other sulfate compounds interact with calcium aluminate; (2) portlandite and monosulfoaluminate interact with sulfate [83]. The crystal structure of ettringite was first proposed by Moore and Taylor [84]: ettringite has a column-based structure with empirical composition $[Ca_3[Al(OH)_6] \cdot 12H_2O]^{3+}$, with sulfate ions and remaining water molecules between columns (Figure 2.4).
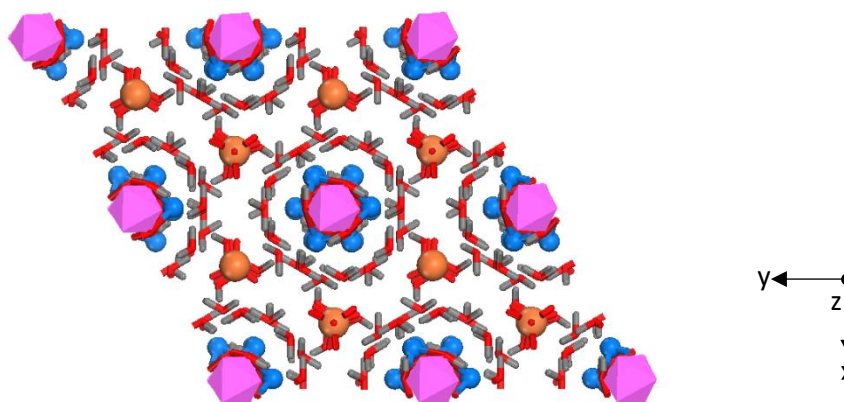
Figure 2.4. A projection of the ettringite crystalline structure as viewed down along (0 0 1) as described in [84]. Blue balls – Ca; pink octahedral - Al; orange balls - S; grey lines – H; red lines – O.

2.3 ^{137}Cs immobilization in Cementitious Materials

Immobilization of cesium ions (Cs^+) in cement pastes has been studied by using a variety of experimental methods, including batch sorption experiments [14–16], high resolution ^{133}Cs solid-state nuclear magnetic resonance (NMR) spectroscopy [17,18], and X-ray diffraction spectroscopy [17,22]. The binding capacity of the cement matrix for Cs^+ ions has been shown to be affected by the chemical composition of the cement paste because different cement phases have different binding capacities and mechanisms [9,85,86].

While some research has shown that PC pastes are not very effective in immobilizing Cs^+ ions with the majority of the Cs^+ ions found as free ions in the interstitial cement pore water [22–25], other research has indicated that the diffusivity of Cs^+ ions in PC was significantly lower than that of Na^+ ions, which suggested the binding of Cs^+ ions onto PC paste [26]. On the other hand, it was generally agreed that Cs^+ ions adsorbed on PC have a high leaching rate [87]. The leaching tests, which were carried out according to the American National Standards Institute/American National Standards (ANSI/ANS), provided only qualitative information and indicated that PC had "acceptable" to "good performance" in capturing Cs^+ ions [88–92].

The interaction mechanisms between Cs^+ ions and cement phases are still not well understood. It has been reported in the literature that Cs^+ ions are highly adsorbed by calcium silicate compounds and hydroxide and that electrostatic adsorption of Cs^+ ions can occur on the

surface of cement phases [19,20]. It has also been suggested that the adsorption of Cs^+ ions increased at lower C/S ratios [19], and that a decrease of pH was concomitant with a decrease of the C/S ratio and a corresponding increase in surface sites with high affinity for Cs^+ ions [14]. However, the opposite effect was found by other researchers. The adsorption of Cs^+ ions has been found to increase with increasing CaO/Al_2O_3 (C/A) ratio and with increasing C/S ratio [15]. A matrix composition low in Al_2O_3 and nearly equimolar in SiO_2 and CaO content proved to be the best for Cs retention [15].

Supplementary cementitious materials have been shown to improve Cs binding capacity and decrease the leachability of Cs^+ ions [93]. Blends of PC and blast furnace slag can effectively immobilize Cs^+ ions because of the generation of Magnesium-Silicate-Hydrate (M-S-H) gel, which is a principal adsorbent of large ionic radii alkali ions, such as Cs^+ ions [94,95]. Silica fume can improve the retention of Cs^+ ions because silica fume react with other oxides and generated stratlingite ($2CaO\text{-}Al_2O_3\text{-}SiO_2\text{-}8H_2O$ or C_2ASH_8 or C-A-S-H), which can help Cs trapping [96]. Cs^+ ions were found chemically bound to the C-A-S-H with low C/S ratio or aluminosilicate gel [97]. Cationic exchange between Cs^+ ions and Ca^{2+} ions ($Cs^+ \text{-} Si^{4+} <\text{-}> Ca^{2+} \text{-} Al^{3+}$) was proposed for the adsorption of Cs^+ ions in C-A-S-H [98]. Particularly, densified silica fume agglomerates blended in cement pastes contained unreacted silica that adsorbed Cs and increased the immobilization of Cs^+ ions [99].

2.3.1 Interactions of ^{137}Cs with Amorphous C-S-H

Batch adsorption experimental data suggested that electrostatic interactions occurred between Cs^+ ions and C-S-H gel [14,17,18]. The C-S-H surface was negatively charged due to the ionization of silanol groups (Si-OH) [8,17,18]. The interaction mechanism between Cs^+ ions and C-S-H was regarded as an ion-exchange process between Cs^+ ions and alkali ions (Na^+, K^+) on negatively charged sites [100], or acidic silanol (Si–OH) sites [8]. Cs^+ ions adsorbed to C-S-H were suggested to form two types of sites with weak and strong affinities. At both sites, Si-OH groups interacted with Cs^+ ions to generate Si-OCs. However, the adsorption of Cs^+ ions to C-S-H gel was dominated by adsorption to strong sites. Therefore, the two-site adsorption model could be simplified to a one-site model, except at high Cs concentrations, at which the strong sites have become saturated [18]. The desorption experiment results showed that the adsorption of Cs^+ ions

12

onto C-S-H gel involved a shortening of silicate chains, and that hydroxide played an important role in this process [67].

X-ray microanalysis indicated that a large portion of Cs^+ ions can be captured by C-S-H [17]. Some research has suggested physical interaction between Cs^+ ions and C-S-H, due to the amorphous property of C-S-H, and C-S-H intermolecular channels can contribute to the physical entrapment of Cs^+ ions [22]. Other research suggested that Cs^+ ions substituted the interlayer sites of C-S-H [68,101,102]. NMR results have indicated that Cs^+ was highly adsorbed on C-S-H; Cs^+ ions directly interacted with the oxygen atoms carried by the bridging silicon to form inner-sphere complexes [103,104].

2.3.2 *Interactions of ^{137}Cs with Tobermorites*

The interactions between Cs^+ ions and tobermorites have been mainly studied by using experimental methods [12,27,105–107]. The interaction mechanisms have been shown to depend on the structure of the solid phase. For example, the mechanisms for the interactions between Cs^+ ions and 11Å tobermorite were found to be different from the interaction between Cs^+ ions with 14Å tobermorite [105,106].

Experimental data indicated that the uptake of Cs^+ ions to 11Å tobermorite might be attributed to the crystallo-chemical incorporation of Cs^+ in a layered lattice framework [27]. The Cs^+ fixation in the layered lattice framework of the 11Å tobermorite was also confirmed by the expansion of the *d* spacing from 11.336Å to 11.596Å. Other experimental data indicated that the uptake of Cs^+ ions in 11Å tobermorite was partly due to the breaking of bonds from planar and edge surface sites of the layered lattice [107].

14Å tobermorite showed a smaller ion exchange capacity with Cs^+ ions than 11Å tobermorite [12]. It was suggested that the uptake of Cs^+ to 14Å tobermorite resulted from the exchange of surface Ca^{2+} cations and the exchange of protons from broken bonds of silicate chains. The small exchange capacity of 14Å tobermorite and small Cs^+ exchange distribution coefficient (K_d) indicated that there were no Ca^{2+} ions present in the interlayer space and exchange was not taking place. The K_d for Cs^+ ions and 14Å tobermorite was smaller than that for Cs^+ ions and 11Å tobermorite (10 and 12 meq/100g, respectively).

Although the interactions between Cs^+ ions and cementitious materials, as well as some specific phases in cement paste, have been widely studied, the interaction mechanisms are still not well understood. This is most likely due to the multi-phase nature of cement paste, and the fact that the interaction mechanisms were significantly affected by the experimental conditions (temperature, concentration of liquid phases, etc.). Therefore, it is important to find a way to study the fundamental interaction mechanisms between Cs^+ ions and cement phases of interest in an environment without intervening external factors.

2.4 ^{99}Tc immobilization in Cementitious Materials

2.4.1   Speciation of ^{99}Tc in the Cement Matrix

The stable form of ^{99}Tc under aerobic conditions is TcO_4^- [108,109]. The speciation of Tc is very sensitive to the redox potential, Eh, of the system, and it also depends on the pore water chemistry, which is characterized by high amounts of alkaline earth metal and hydroxyl ions (pH > 12) in most cements [110].

The solubility of ^{99}Tc is significantly lowered under reducing conditions compared to oxidizing conditions. Low Eh values in cementitious waste forms can be imposed by blending specific additives, *e.g.*, iron blast furnace slag (BFS), and/or the corrosion of the steel containers, which leads to the formation of magnetite [110]. pH values as low as 11 and Eh values as low as −400 mV have been measured in blended PCs [111]. In a low pH-Eh environment, ^{99}Tc is present as hydrous oxide (Tc^{4+}) (Figure 2.5).

PC and fly ash pastes both have high pH and Eh values (pH ~ 13.5 and Eh ~ 250mV for PC, pH ~12 and Eh ~ 50mV for fly ash) [111], and theoretical calculations indicated that under these pH-Eh conditions, the dominant redox species of ^{99}Tc is TcO_4^- [110] (Figure 2.5).
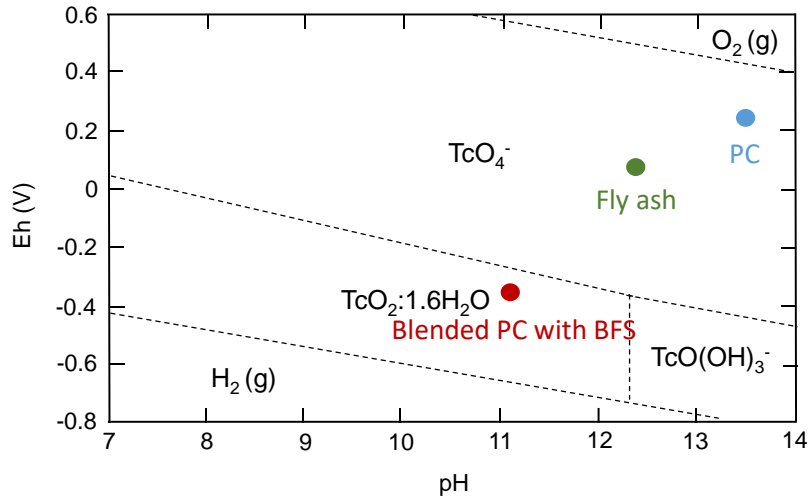
Figure 2.5. Solubility limits for Tc according to the national education association (NEA) database，[Tc] = 1e-7M (adapted from [110]).

2.4.2 Retention of ^{99}Tc in the Cement Matrix

PC and fly ash grouts have been shown to be marginally acceptable for retention of radioactive TcO_4^- [32]. Experimental data have indicated that the primary adsorption mechanism was anion exchange, and that the exchange with Ca^{2+} ions was weak; the distribution coefficient K_d ranged from 0.8 to 96 mL/g [32].

Leaching tests have shown that ground blast furnace slag could improve the leach resistance of cement-based waste forms for [99]Tc [29,32,109]. Compared to PC paste, cement materials made with blast furnace slag or solidified slag had fewer and smaller pores, which slowed ^{99}Tc from leaching. Moreover, the resulting reducing environment could convert TcO_4^- ions to a less soluble Tc^{4+} species and effectively immobilize ^{99}Tc as TcS_x or $TcO_2 \bullet xH_2O$ [29,30]. When ground blast furnace slag was added to the grout, the uptake performance of ^{99}Tc was significantly improved: the leachability index (*LI*) of ^{99}Tc was reduced by several units from 10.5 to 6.1 [109,112]; the effective diffusion coefficient (D_{eff}) of ^{99}Tc was 10 times smaller than that in ordinary grout [29]; and the K_d was greater than 1000 mL/g, which was much higher than that under aerobic conditions (*i.e.*, $K_d = 0.8 – 96$ mL/g) [32].

2.5   Molecular Dynamics (MD) Modeling of the Interactions between Ions and Clay Minerals/ Cement Phases

2.5.1   MD Studies of Adsorption onto Cement Phases

Although tobermorite, jennite and ettringite have been studied using MD simulations, most studies to date have focused on structural and mechanical properties of cement phases [113–122]. Those studies concerning dynamic properties either focused on the interactions between cement phases and other ions or molecules, such as Na^+, Sr^{2+} ions, and H_2O molecules [13,35–37,123,124], or used forcefields other than the ClayFF forcefield that was used in this work [117,118,125,126]. Results from the literature have shown that tobermorites and jennite were capable of adsorbing and incorporating ions. Alkali ions such as Na^+ and K^+ ions can be adsorbed both on the surface and penetrate into the silicate channels of 9Å tobermorite and jennite to interact with oxygen atoms on the silicate chains, and interactions in the silicate channels were suggested to be chemical bonding [35]. The alkali ions associated with the solid phase had low diffusion coefficients, which were much lower than the ions in bulk solution [35,36]. H_2O molecules in the silicate channels and above the surface developed integrated H-bond networks with surface sites and demonstrated the following features: large density, layered arrangement, preferred orientation, and low diffusion coefficient [35,36]. Sr^{2+} exchanged with interlayer Ca^{2+} in the 9Å tobermorite structure and was bonded to the solid phase while the integrity of the silicate chains was maintained. The 9Å tobermorite structure has been shown to be a good candidate for immobilizing radioactive ^{90}Sr [37]. 14Å tobermorite adsorbed Ca^{2+} due to the negative interfacial charge, and Ca^{2+} ions interacted with hydroxyl O through strong electronic attraction. However, the stability of surface adsorbed Ca^{2+} can be disturbed by counterions, such as Cl^- ions in the solution, and eventually diffuse away from the surface [124].

2.5.2   MD Studies of Adsorption of Radionuclides onto Clay Minerals

The interactions between Cs^+ ions and clay minerals — mica, illite, smectite (such as montmorillonite, bentonite, hectorite and beidellite) — have been studied by using MD simulations. The results suggested that the interactions were thermodynamically favorable and that Cs^+ ions formed both inner-sphere and outer-sphere complexes while interacting with these clay minerals. Cs^+ ions competed with other ions present in the solution, such as Na^+ ions, as well as water molecules to adsorb on the solid phases [38–42,127–130]. The results indicated Cs^+ ions mainly formed a single type of inner-sphere complex on basal surfaces while interacting with illite

16

and mica [127,129,130]. Different edge sites were observed in illite, and Cs^+ ions adsorbed primarily at edge sites where cleaved pockets were exposed at the edge surface [127].

When Cs^+ ions interacted with smectite, inner-sphere complexes coexisted with outer-sphere complexes, and inner-sphere complexes were preferentially formed [38–42]. For smectite hydrates, partially hydrated Cs^+ ions generally formed two different types of inner-sphere complexes with the basal surface: above the center of the surface (ditrigonal or hexagonal) cavities, and above surface Si tetrahedral [39–41]. The surface of smectite contained various hexagonal cavity sites (H-sites) and tetrahedral Si sites (T-sites), which were capable of coordinating Cs^+ ions. The preference of Cs^+ ions interacting with different sites was illustrated by the following sequence: tetrahedrally substituted H-sites > nonsubstituted H-sites > tetrahedrally substituted T-sites > nonsubstituted T-sites [40,41]. Especially, on the surface of montmorillonite, Cs^+ ions adsorbed on tetrahedrally substituted H-sites and formed exclusively inner-sphere complexes. Cs^+ ions adsorbed on other sites formed both inner-sphere and outer-sphere complexes with roughly equal probability [40]. Cs^+ ions were found strongly coordinated to bridging O on the clay surface, and diffused much more slowly than in bulk solution [39,42].

While the mechanical and structural properties of ettringite have been studied using MD simulation [131,132], interaction mechanisms between ettringite and ions have not been studied in detail [13]. However, some of these MD simulations were performed with ClayFF forcefield [13], which has also been used to study the interfacial dynamic properties for other cement phases.

MD simulations and density functional theory (DFT) MD simulations have been applied to study the interactions between TcO_4^- and other ions or water molecules in aqueous solution [133–135]. The adsorption of TcO_4^- ions on a mesoporous amorphous silica known as self-assembled monolayers on mesoporous supports (SAMMS) has also been investigated using MD simulations [136]. The application of MD simulations on the TcO_4^- ions has been drawing more and more attention. The classical forcefield parameters of TcO_4^- ions used in this work have just been developed [44], and the structural and dynamic properties of hydrated TcO_4^- ions in aqueous phase have been studied. The hydration free energy obtained by using the classic forcefield method has been proved to be comparable with the value obtained by using theoretical calculation [137] and a quantum physics simulation [44]. The comparisons indicated that the forcefield parameters were reliable. MD simulation data on the interactions between TcO_4^- ions and cement phases or

17

other clay minerals have not been published yet; therefore, this work is meaningful to both future theoretical and experimental work.

2.6   Conclusions and Literature Gaps

While the interaction of Cs^+ and TcO_4^- ions with cementitious phases have been studied in the literature using mostly experimental methods, the mechanisms of adsorption are still not well understood most likely due to the wide range composition of C-S-H.

The adsorption processes of ions on the basal surface/interface of the cement phases are strongly influenced by the following parameters: (1) the structure and composition of the cement phases substrate; and (2) the composition and structure of the near-surface solution and its dynamics, which are different from that of the bulk liquid phase [39]. MD simulation has been used to study the interfacial adsorption mechanisms between crystalline C-S-H phases and other ions and has also been used to study the interaction between Cs^+ ions and other clay minerals. The adsorption of Cs^+ ions on the surfaces of crystalline C-S-H phases can be envisioned given the fact that Cs^+ ions had strong interaction with smectite.

PC was studied because it is the most widely used cementitious waste form although blast furnace slag blended cementitious waste forms may be more effective to immobilize [99]Tc. Moreover, understanding the interaction mechanisms between PC paste and TcO_4^- is the key to decreasing leaching and designing better waste forms for [99]Tc.

Although MD has been widely used to study the interfacial interactions between ions and solid phases, the interactions between Cs^+ ions and crystalline C-S-H phases have only been briefly studied. Furthermore, the interaction mechanisms between TcO_4^- ions and cement phases have never been addressed using MD simulations. It is necessary to study the fundamental interaction mechanisms between radionuclides (*i.e.* Cs^+ and TcO_4^-) and specific cement phases (*i.e.* crystalline C-S-H and ettringite) at the atomic level with molecular dynamics (MD) simulations, so that this knowledge could be used to improve the performance of future waste forms.

CHAPTER 3

3   MD Simulation and Data Analysis Methods

3.1   Overview and Objectives

The MD simulation results are influenced by the following factors: (1) the equilibrium status of the system, (2) the amount of data used for data analysis, and (3) the methods employed for data analysis. This chapter develops a framework for evaluating the interaction mechanisms of radionuclides with cement phases that includes monitoring convergence of the simulations to equilibrium and developing a data analysis methodology that can provide statistically reliable results.

3.2   Methods Used to Construct the Solid-Liquid Interface Computational Cell

Two different methods to construct the solid-liquid interface computational cells were investigated. In method 1, the liquid and solid phases were first built individually and then stacked on top of each other. In method 2, the water molecules and ions were placed into a vacuum between two layers of solid phases.

Method 1. Method 1 was widely used in the literature in previous MD studies [138–140] to investigate interfacial interactions between liquid and solid phases. To simulate the interaction of 9Å tobermorite with an aqueous solution, the 9Å tobermorite was cleaved parallel to the (0 0 1) and (0 0 -1) crystallographic planes in such a way that only hydroxyl groups were exposed on the surfaces. The (0 0 1) surface was characterized by tetrahedral SiO_4 chains with Si-bonded hydroxyls pointing out, and the (0 0 -1) surface was characterized by an octahedral CaO_6 layer with the Ca-bonded and Si-bonded hydroxyl groups pointing out. Interlayer water molecules were evenly distributed on both surfaces. A layer of liquid phase with the same *a* and *b* length of the solid phase and a thickness of 50Å was built. The thickness of the layer of aqueous solution was large enough to effectively eliminate direct interaction between the two solution/solid interfaces [139]. Cs^+ and Cl^- ions were randomly inserted in the midplane of the aqueous region to avoid biased adsorption. The 9Å tobermorite crystal and solution were kept charge neutral. Periodic boundary conditions were applied in all three dimensions. Each phase was geometry optimized

before the solid-liquid-solid structure was built up. The geometry optimization was then performed on the whole structure.

Method 2. Both layers of 9Å tobermorite used in method 1 were used in method 2 to build the simulation box, with a 50Å thick vacuum in between and the tetrahedral SiO_4 and the octahedral CaO_6 surfaces facing the vacuum. Then H_2O molecules, Cs^+ ions, and Cl^- ions were packed into the vacuum. The concentration of the solution was made to match the data measured by experiment [141]. Periodic Boundary Conditions (PBC) were applied in all three dimensions. Each layer was geometry optimized individually by constraining the other layers. Then geometry optimization was performed on the whole structure.

Evaluation of the two methods described above was conducted by visualizing the computational cell after 1 nanosecond (ns) of MD simulation and comparing the density of the liquid phase before and after MD simulation.

Constructing the solid-liquid interface computational cells with method 1 posed several difficulties: 1) a vacuum layer was automatically placed (by Materials Studio) between the liquid layer and the solid layer to avoid overlap between these two layers, which increased the volume of the liquid phase during the MD simulation (*i.e.* after the MD simulation began, the vacuum layer disappeared and that volume became associated with the liquid layer) and eventually changed the concentration of the solution; 2) a void area was generated in the middle of the solution after equilibration of the system with the canonical ensemble (NVT) (Figure 3.1a); and 3) with Materials Studio, the aqueous phase was only allowed to be built as a cubic, tetragonal, or orthorhombic lattice. As a result, the angle of aqueous lattice had to be changed to match the cell parameters of the solid phase, which would change the concentration of solution.

Compared to method 1, method 2 had several advantages: 1) the space between the liquid phase and the solid phase was eliminated; 2) the dimension of the liquid layer could be matched with that of the solid phase; 3) void areas in the liquid phase were no longer observed after MD equilibration (Figure 3.1b); and 4) the vacuum between the solid layers represented the pore space, which was more realistic.

20
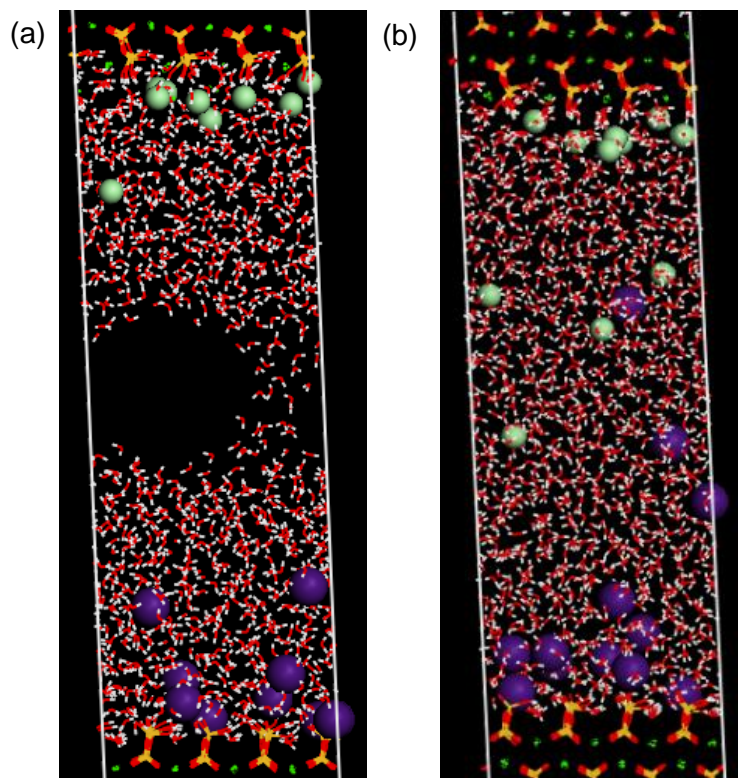
Figure 3.1. Configuration of simulations with two different methods after 1 ns of MD simulation: (a) method 1 and (b) method 2. Void area was seen in the middle section for method 1.

3.3 The Effect of Different Ensembles to Equilibrate the Liquid-Solid Interface Computational Cell

After finishing the geometry optimization of the models and choosing method 2 to construct solid-liquid interface computational cells, MD simulations were performed with different ensembles to equilibrate the systems. Then 13-20ns of MD simulation were performed for further data analysis.

According to the postulate of the ergodic hypothesis, for an isolated system at equilibrium, all the accessible states are equally probable over a long-time period, independently from the initial time, positions, momenta for a given number of atoms (N) in a volume (V) and at a constant energy (E). Thus, the property average over time and the average over all the states (ensemble average) at the equilibrium are the same [101, 102]. However, real physical systems are usually either too small to follow the ergodic hypothesis or contain at least some uncertainty in energy. Therefore, an alternative is to simulate a system, which is coupled with an external thermal bath by applying

canonical ensemble (NVT). In other cases, for systems with unknown parameters, such as the density and the chemical composition of the system, isothermal-isobaric ensemble (NPT) or grand-canonical ensemble (μVT) could provide more useful simulation results. In the present work, the computational cells were equilibrated in two different ways to study the effect of different ensembles on the performance of MD simulation: (i) NVT ensemble; (ii) NPT ensemble was added to NVT ensemble in a cascade manner. NPT ensemble was necessary to relax the solid-liquid-solid system and adjust the size of the simulation cell so that the system could reach the energy minimum point and the physical state of the liquid phase could maintain realistic.

3.4   Convergence Monitoring of the Simulations to Equilibrium

Several techniques for the definition of the equilibrium of a system in MD simulation exist and have been reported in the literature [142], including intramolecular interaction energy, number of hydrogen bonds, root mean square fluctuations (RMSF), torsion angle transition cluster counting [143], structural histograms of cluster [144], principle component analysis [145], and configurational energy [146]. A very common technique is the root mean square deviation (RMSD), which describes the spatial difference between two static structures.

In present work, the NPT MD followed by NVT MD strategy was used to equilibrate the system. This methodology was applied due to the requirement of maintaining the concentration of the liquid phase and the fact that NPT ensemble is closer to experimental conditions. However, after the energy, temperature, pressure and some of the structural properties (size, density of the supercell) of the system become stabilized, NVT ensemble was preferred to continue the MD simulation to decrease simulation time. NPT ensemble MD was performed for 400 picoseconds (ps) even though the energy, temperature, pressure, cell parameters of the supercell and the density of the liquid phase became stable several ps after NPT ensemble MD started. Then 1 ns of NVT ensemble MD was used to continue to equilibrate the system. The trajectory of a second NVT ensemble MD, which was named data acquisition, was recorded every 0.1 ps. The length of data acquisition depended on the dynamic convergence of the system and the requirement of statistic reliability of data analysis [35,124,147,148]. The length of the data acquisition ranged from 13 ns to 20 ns, and the last 5 ns to 6 ns of equilibrated trajectory in data acquisition was used for all the data analysis.

The convergence to equilibrium of the system was evaluated by calculating the Root Mean Square Displacement (RMSD) of ions and the first layer atom on the surface because the purpose of this research was to study the properties of solid-liquid interface. RMSDs were calculated between the starting point of the NVT ensemble MD simulation and all succeeding frames; the plateau of RMSD values was considered equilibrium [149–153]. Particularly, the RMSD values in the z-direction were used as the most important factors to evaluate the adsorption equilibrium because the surfaces were parallel to the xy-plane; the movement of ions on the surface in the z-direction was related to the adsorption-desorption process.

3.4.1   Equilibrium Monitoring of Cs$^+$ Ions on the Surface of Crystalline C-S-H Phases

The first layer of atoms on the SiO_4 tetrahedral surface ((0 0 1) plane) included hydroxyl oxygen, bridging oxygen with tetrahedral substitution, and silica ions at the surface in the first layer of silicate chains, as well as O in the interlayer water molecules and hydroxyl groups at the interface for the 14Å tobermorite and jennite models. Although same types of atoms at the surfaces of crystalline C-S-H phases were selected to calculate the RMSD, the amounts of atoms were different due to the different structures. The total number of atoms in the first layer and thus used for the RMSD calculation were 60 for the 0.5M CsCl/9Å tobermorite system, 69 for the 0.5M CsCl/14Å tobermorite system, and 92 for the 0.5M CsCl/jennite system (Figure 3.2). All systems were assumed to have reached equilibrium at the end of the simulation. The data acquisition trajectories were segmented into a series of 1-ns pieces (10,000 frames) at a running 0.1-ns interval (1,000 frames) backwards. This process generated 140 or 130 pieces of trajectories, which were overlapping. The interval mean and corresponding running mean (*i.e.* the mean calculated from the last frame of the data acquisition trajectory to the first frame of trajectory segment) for the RMSD curves in the z-direction were calculated for each piece of trajectory, then compared. If the running mean and interval mean started to diverge, and the difference was larger than maximum difference between the running mean and interval mean, the system was considered unequilibrated. The RMSD plateaus continued for at least 5 ns (Figure 3.3). The results indicated that at the tetrahedral SiO_4 surfaces, the 0.5M CsCl/9Å tobermorite system reached equilibrium at ~6 ns, 0.5M CsCl/14Å tobermorite model reached equilibrium at ~1 ns, and 0.5M CsCl/jennite model reached equilibrium at ~4.2 ns.

Based on the results from RMSD and analysis of the total number of ions adsorbed per unit area, the last 6-8 ns of all the trajectories (8 ns for tobermorites and 6 ns for jennite) were sampled for structural, statistical, and dynamical analysis. The large sampling was used to ensure statistical reliability of the data.
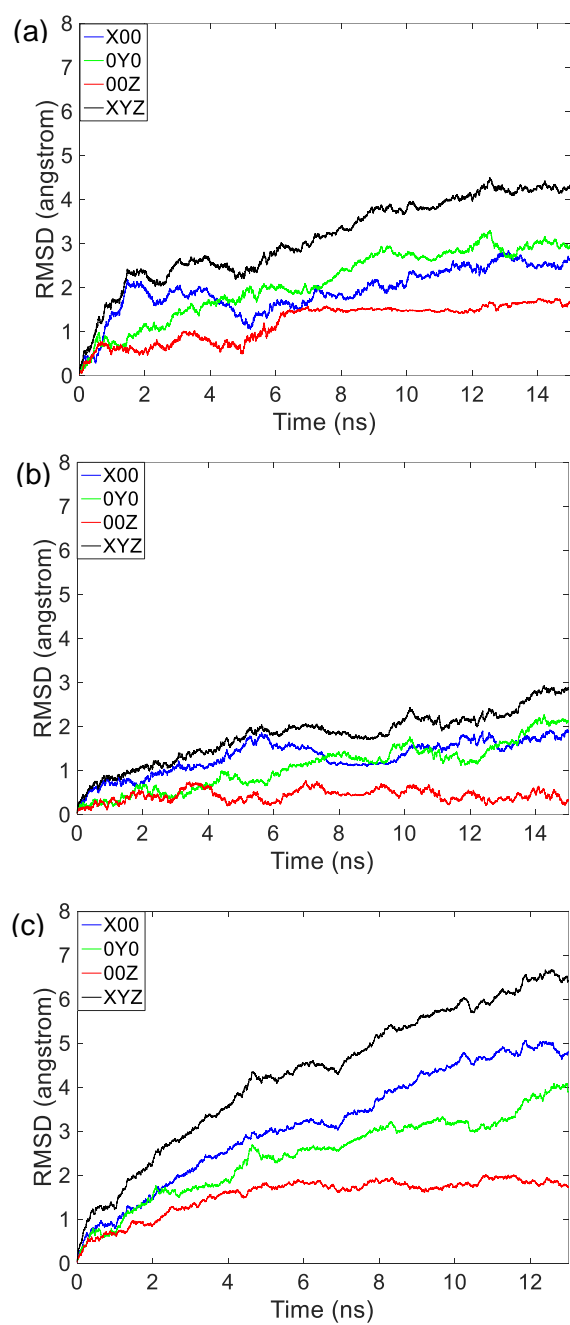
Figure 3.2. The RMSD of Cs^+ ions and the first layer atoms at the tetrahedral SiO_4 surfaces of: (a) 9Å tobermorite, (B) 14Å tobermorite and (c) jennite.
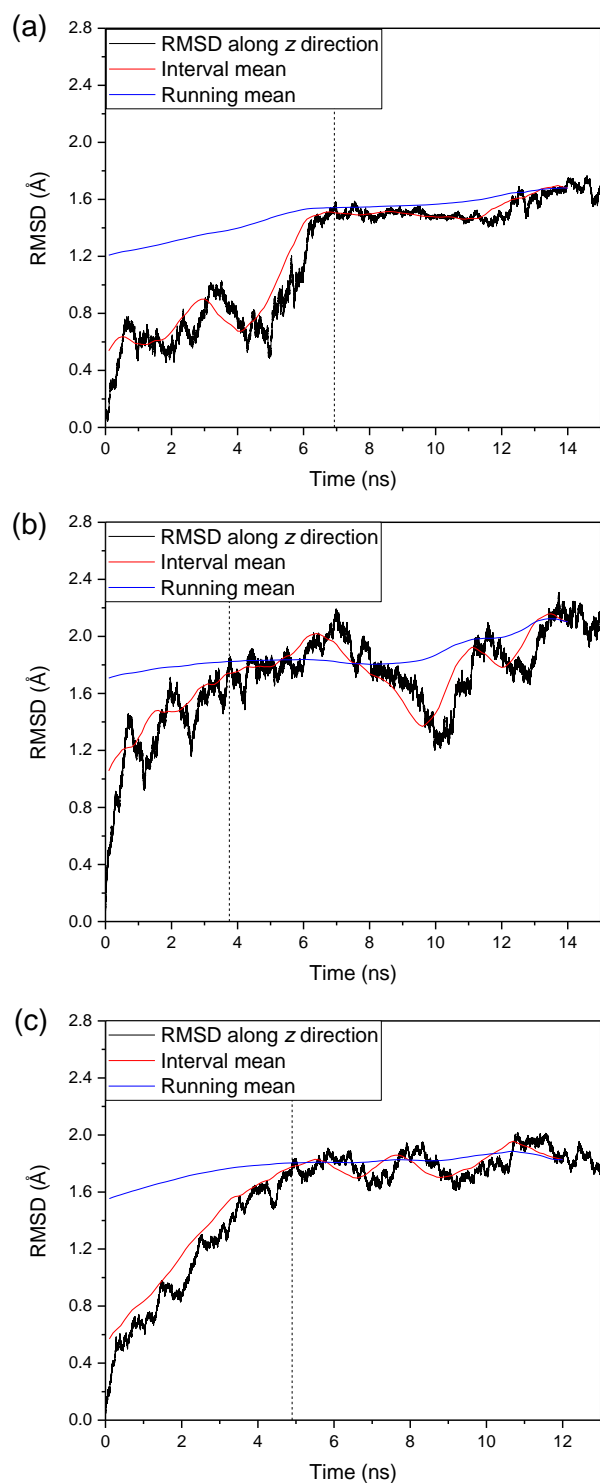
Figure 3.3. Interval mean and running mean for the *z*-direction RMSD of Cs$^+$ ions and the first layer atoms at the at the tetrahedral SiO$_4$ surfaces of: (a) 9Å tobermorite, (b) 14Å tobermorite, and (c) jennite.

3.4.2   Equilibrium Monitoring of TcO_4^- Ions on the Surface of Cement Phases

The equilibrium of TcO_4^- adsorption on the CaO_6 surfaces of cement phases was evaluated with the same methods described in section 3.2.1. The first layer atoms on the CaO_6 surfaces of 14Å tobermorite and jennite included all the hydroxyl oxygen, bridging oxygen with tetrahedral substitution, and silica ions at the surface in the first layer of silicate chains, as well as interlayer Ca ions at the interface. The first layer atoms on the CaO_6 surface of ettringite included all the sulfur and aluminum atoms in the first layer of SO_4 and AlO_6 groups, as well as interlayer Ca ions at the interface. Although same types of atoms at the surfaces of cement phases were selected to calculate the RMSD, the amounts of atoms were different due to the different structures. The number of atoms in the first layer and thus used in the RMSD calculation were 68 for 0.2M $KTcO_4$/14Å tobermorite and 68 for 0.2M $KTcO_4$/jennite, and 61 for 0.2M $KTcO_4$/ettringite, respectively. The data acquisition trajectories were segmented to a series of 1-ns pieces (10,000 frames) at a running 0.1-ns interval (1,000 frames) backwards (Figure 3.4). This process generated 190 pieces of trajectories that were overlapping. By comparing the running mean and the interval mean of the RMSDs in the *z*-direction, the results indicated that 0.2M $KTcO_4$/14Å tobermorite system reached equilibrium at ~11.5 ns, 0.2M $KTcO_4$/jennite system reached equilibrium at ~12.5 ns, and 0.2M $KTcO_4$/ettringite system reached equilibrium at ~11.0 ns (Figure 3.5). For the sake of consistency, only the last 6 ns of trajectories of all the systems were collected for data analysis.
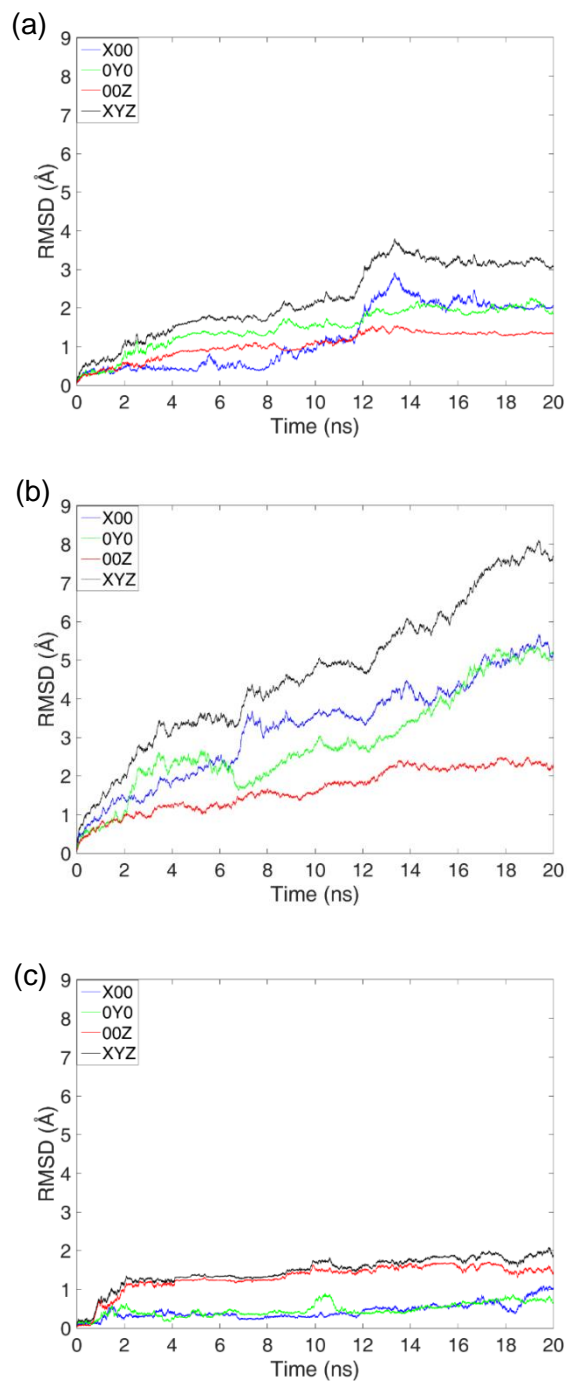
Figure 3.4. RMSD of TcO$_4^-$ ions and the atoms of first layer on the octahedral CaO$_6$ surfaces of: (a) 14Å tobermorite, (b) jennite, and (c) ettringite.
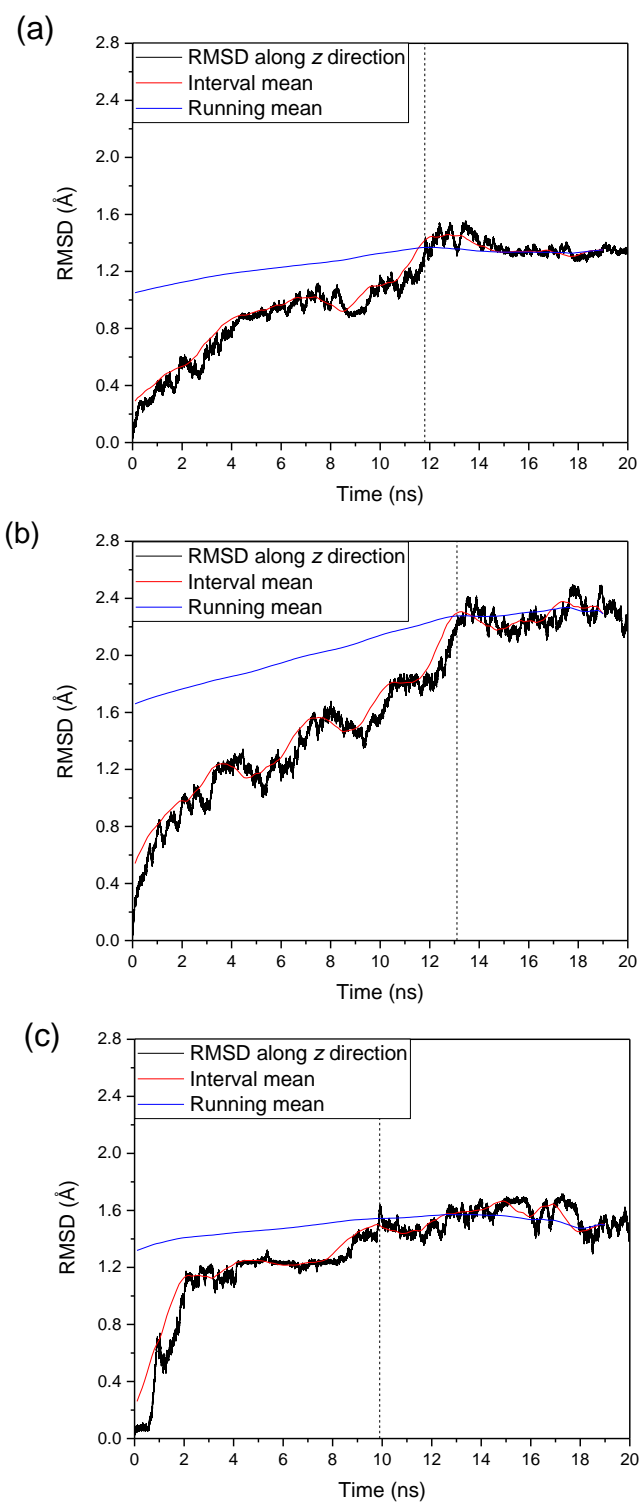
Figure 3.5. RMSD along the *z*-direction, and corresponding interval mean and running mean TcO_4^- ions and the first layer of surface element: a) 14Å tobermorite; b) jennite and c) ettringite.

3.5 Inner-Sphere and Outer-Sphere Regions

The data were analyzed in terms of inner-sphere and outer-sphere complexes.

3.5.1 *Definition of Inner-Sphere and Outer-Sphere Complexes*

An ion binds at the surface of clay minerals either as an inner-sphere complex or an outer-sphere complex. An inner-sphere surface complex has no water molecule interposed between the surface functional group and the small cation or molecule it binds, whereas an outer-sphere surface complex has at least one such interposed water molecule [154]. The inner-sphere and outer-sphere complexes have different configurations and interaction mechanisms with the surface. Therefore, the identification and characterization of inner-sphere and outer-sphere complexes are critical to understand the reactivity of the surface.

Inner-sphere and outer-sphere complexation models have been best described by the triple layer model (TLM), which has been extensively used to characterize the clay minerals/aqueous phase interface interaction [155–158].

The electrical double layer (EDL) is a liquid region developed at the solid-liquid interface due to the surface charge of solid phase. The EDL contains oppositely charged counterions to maintain the electroneutrality of the solid-liquid interface (Figure 3.6). The EDL includes the Stern layer and the diffuse layer. The charge and electrostatic potential distributions within the Stern layer are assumed to be linear [159]. The distribution and electrostatic potential of ions within the diffuse layer is described by the Poisson-Boltzman relation [159]. The TLM includes three planes that divide the Stern layer into two sublayers: the inner-sphere region and the outer-sphere region. The solid surface is defined by the 0-plane, the d-plane is the boundary between the Stern layer and the diffuse layer, and the β-plane is located between the 0-plane and d-plane. The inner-sphere region is located between the 0-plane and β-plane; it includes all the dehydrated ions bound directly to the surface (inner-sphere complexes). The outer-sphere region consists of hydrated counterions (outer-sphere complexes) and is located between the β-plane and d-plane; all diffuse swarm species are located beyond the d-plane. The outer-sphere complexes and the diffuse swarm species exhibit similar physical and chemical properties, as evidenced by some NMR studies of cation adsorption on mineral surfaces, which found out that NMR did not really distinguish outer-sphere complexes from diffuse swarm species [104].

Theoretical studies concerning the TLM described the distance from the surface (0-plane) to the inner edge of the diffuse layer (d-plane) as 1 to 2 counterions, or hydrated counterions, diameters [160–162]. The thickness of a Stern layer ranged from 2 to 10Å depending on the counterion and degree of hydration assumed near the surface [163]. However, these theoretical studies only provide the methods to locate the β-plane and d-plane in MD simulations. Two main methods have been used in the literature to locate the β-plane and d-plane in MD simulations.

Using concentration profiles of oxygen in water molecules. Some researchers have used the concentration profiles of oxygen in water molecules to define the location of β-plane and d-plane [128,164,165]. Marry, *et al*. [128] stated that the distributions of water oxygen and hydrogen atoms were almost independent of the nature of the counterions, because most water molecules did not belong to the solvation shell of counterions. However, this result conflicted with the definition that each counterion has an individual electrostatic plane which depends on the crystallographic radius of the counterion.
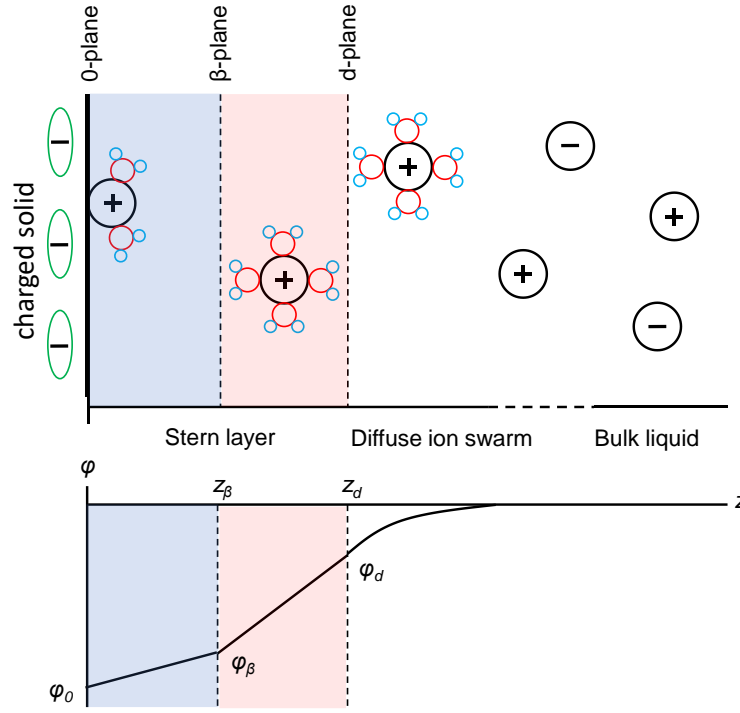
Figure 3.6. Conceptual model of EDL structure and TLM (top) and electrostatic potential $\psi(z)$ (bottom, relative to a reference state in the bulk liquid) as a function of distance from a negatively charged surface according to the TLM [158]. Inner-sphere region is highlighted by blue, outer-sphere region is highlighted by red.

Using concentration profiles of counterions. Another way to define the location of the β-plane and d-plane is to use the concentration profiles of counterions. The electrostatic potential for the Stern layers are explained by the following mathematical formulas:

$$\psi_\beta - \psi_o = \frac{-\sigma_o}{C_1} \tag{1}$$

$$\psi_d - \psi_\beta = \frac{-\sigma_d}{C_2} \tag{2}$$

$$C = \varepsilon \frac{A}{d} \tag{3}$$

Where

σ_o is the surface charge density (solid structural charge plus the charge of all species adsorbed in the 0-plane);

σ_d is the excess charge in the diffuse layer;

ψ_o, ψ_β and ψ_d are the electrostatic potentials at the 0-, β-, and d-planes;

C is the capacitance, in farads; C_1 is the capacitance between 0- and β-planes, C_2 is the capacitance between β- and d-planes;

A is the area of overlap of the two plates, in square meters;

ε is the permittivity (sometimes called the dielectric constant) of the material between the plates;

d is the separation between the plates, in meters;

These formulas imply that the electrostatic potential of each layer depends on the permittivity (ε) of the layer. The permittivity for aqueous solutions depends on the concentration of the solution [166,167]. The TLM assumes that the permittivity is homogeneous in each layer. The change of the slope of electrostatic potential in between the two layers indicates the sudden change of concentration (capacitance and electrostatic potential are related to the concentration of the ions), which can be illustrated by the concentration profiles of counterions. By employing this interpretation, the structure of the TLM could be predicted by the concentration profiles of electrolyte counterions [168].

3.5.2 Identification of Inner-Sphere and Outer-Sphere Regions for Cs^+ Ion Adsorption

For Cs^+ ion adsorption, the method used to define the location inner-sphere and outer-sphere regions consisted of combining the relative atomic density profiles of water molecules and ions (Figure 3.7). The relative atomic density profile was plotted based on the position of nuclei. The relative atomic density profiles of oxygen in water molecules was used as an indicator of the occurrence of inner-sphere complexes and outer-sphere complexes, and the relative atomic density profiles of counterions was used to locate inner-sphere region and outer-sphere region. The boundary between the outer-sphere region and diffuse ion swarm was defined by the shoulder of the second peak in Cs profile due to the smooth transition of electrostatic potential on the d-plane (Figure 3.6). To sum up, the inner-sphere region and the outer-sphere region were defined as:

- The layer where the first peak of Cs^+ ions beyond the surface located was defined as the inner-sphere region if there was not a peak for water O between the surface and the peak of Cs^+ ions;

- If the inner-sphere complexes exist, the lowest point between first and second peak of Cs^+ ions and was the boundary between inner-sphere region and outer-sphere region;

- The layer where the second peak of Cs^+ ions beyond the surface located was defined as the outer-sphere region if there was a peak for water O between the surface and the peak of Cs^+ ions;

- The middle point of the shoulder of the second peak of Cs^+ ions was defined as the boundary between outer-sphere region and diffuse ion swarm.
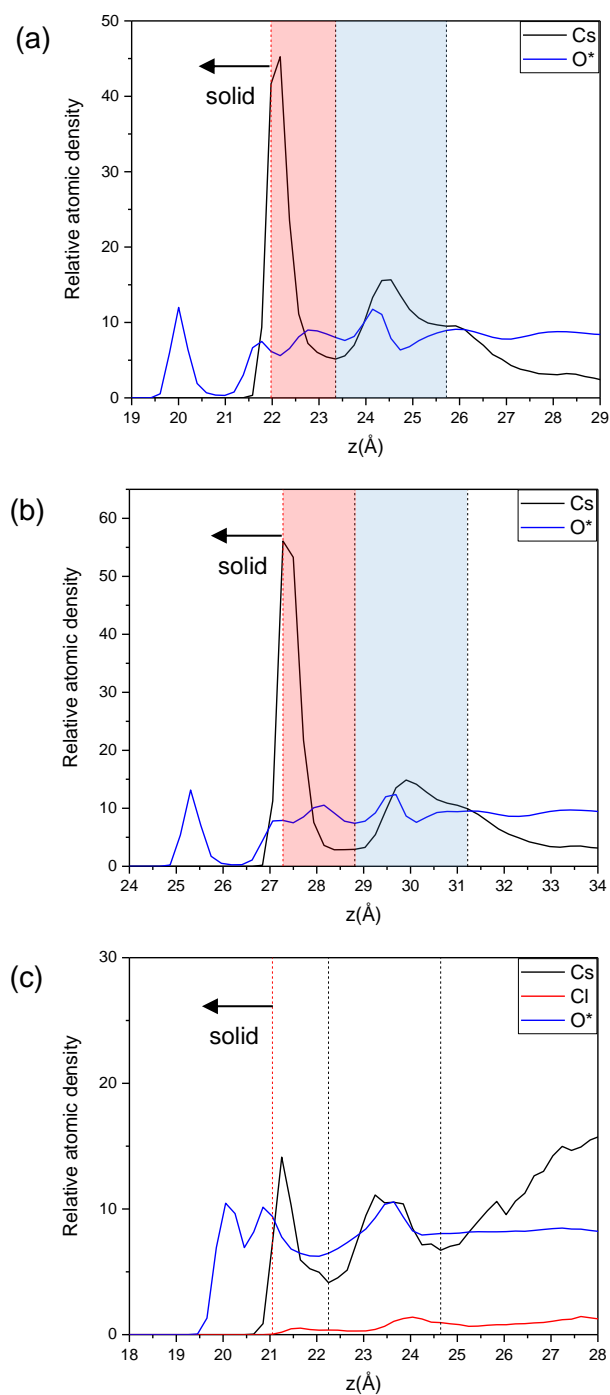
Figure 3.7. Relative atomic density profiles of: (a) 9Å tobermorite/0.5M CsCl, (b) 14Å tobermorite/0.5M CsCl, and (c) jennite/0.5M CsCl. Color code: black – Cs, red – Cl, blue – water O. Inner-sphere region is highlighted in blue, outer-sphere region is highlight. Thickness of inner-sphere region: 1.38Å for 9Å tobermorite, 1.31Å for 14Å tobermorite, respectively; thickness of outer-sphere region: 2.17Å for 9Å tobermorite, 2.63Å for 14Å tobermorite, respectively.

3.5.3 Identification of Inner-Sphere and Outer-Sphere Regions for TcO$_4^-$ Ion Adsorption

For TcO$_4^-$ ion adsorption, the determination of the inner-sphere and outer-sphere regions on the surfaces of 14Å tobermorite, jennite, and ettringite followed the method described in section 3.3.2 (Figure 3.8). The adsorption of TcO$_4^-$ ions was observed on the octahedral CaO$_6$ surfaces of 14Å tobermorite and ettringite. On the octahedral CaO$_6$ surface of 14Å tobermorite and ettringite, relative atomic density profiles of Tc ions were zoomed in and combined with the relative atomic density profiles of O in water molecules to identify the inner-sphere complexes and outer-sphere complexes on the surfaces. The relative atomic density profile of O in water molecules showed no peak between the surface and the first peak of Tc on the surface of 14Å tobermorite. There was at least one peak of water O between the surface and the second major Tc peak, which indicated that near the surface of 14Å tobermorite TcO$_4^-$ ions formed both inner-sphere and outer-sphere complexes. The tails of the Tc profile indicated that surface Tc complexes had the chance to diffuse out of the surface area to the diffuse swarm and even to the bulk solution. On the other hand, on the surface of ettringite, there was an obvious peak of water O between the surface and the Tc profile, which indicated that on the surface of ettringite, TcO$_4^-$ ions only generated outer-sphere complexes.
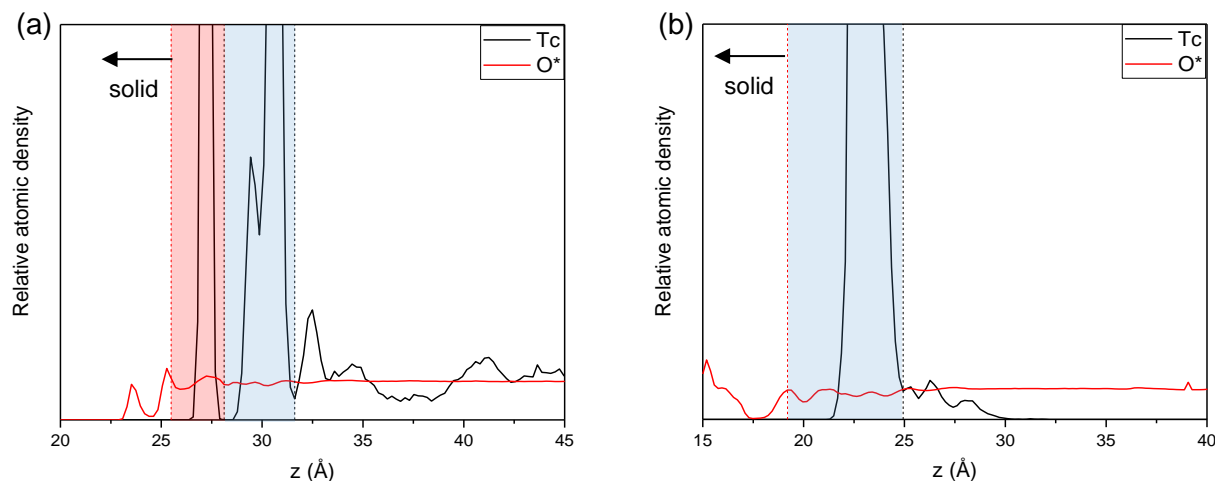
Figure 3.8. Relative atomic density profiles of Tc ion and O in water molecules at the surface of: a) 14Å tobermorite and b) ettringite. Inner-sphere region was highlighted in red, outer-sphere region was highlighted in blue.

3.6 Residence Time and Adsorption Stability

The residence time of the inner-sphere and outer-sphere complexes was used to identify stable adsorption events. An inner-sphere adsorption event was qualified as stable if the Cs^+ ion stayed in the inner-sphere region for at least 0.7 ns for computational efficiency. Previous research indicated [169] that if an ion stayed in the inner-sphere region longer than 0.5 ns, it was a stable inner-sphere adsorption. In the present work, the z-coordinates of each Cs^+ ion were plotted as a function of time to determine the duration of stable inner-sphere adsorption (Figure 3.9, Figure 3.10, and Figure 3.11). The adsorption events of Cs^+ ions that stayed in the inner-sphere region longer than 0.5 ns were summarized (Table 3.1 for the 9Å tobermorite/0.5M CsCl system, and the summary for other systems was provided in Appendix A). The results indicated that most of Cs^+ ions remained in the inner-sphere region for 0.5~1.0 ns; 1.4 ns was the maximum time that Cs^+ ions remained in the inner-sphere region of 9Å tobermorite. The adsorption events of Cs^+ ions that remained in the outer-sphere region longer than 0.25 ns and that of aqueous species that remained in the bulk solution without approaching the surfaces longer than 0.5 ns (*i.e.* stable aqueous species) were also summarized (Table 3.1 for 9Å tobermorite/0.5M CsCl system, and the summary for other systems was provided in Appendix A). To ensure adsorption stability, 0.7 ns was used in this work as the criterion to determine the stable inner-sphere complexes and the stable aqueous species; 0.25 ns was used as the criteria to determine the stable outer-sphere complexes.

The same criteria were used to identify stable TcO_4^- ions adsorption (Figure 3.12, Figure 3.13, and Figure 3.14). The summaries of residence times for TcO_4^- ions in different regions are provided in Appendix A.
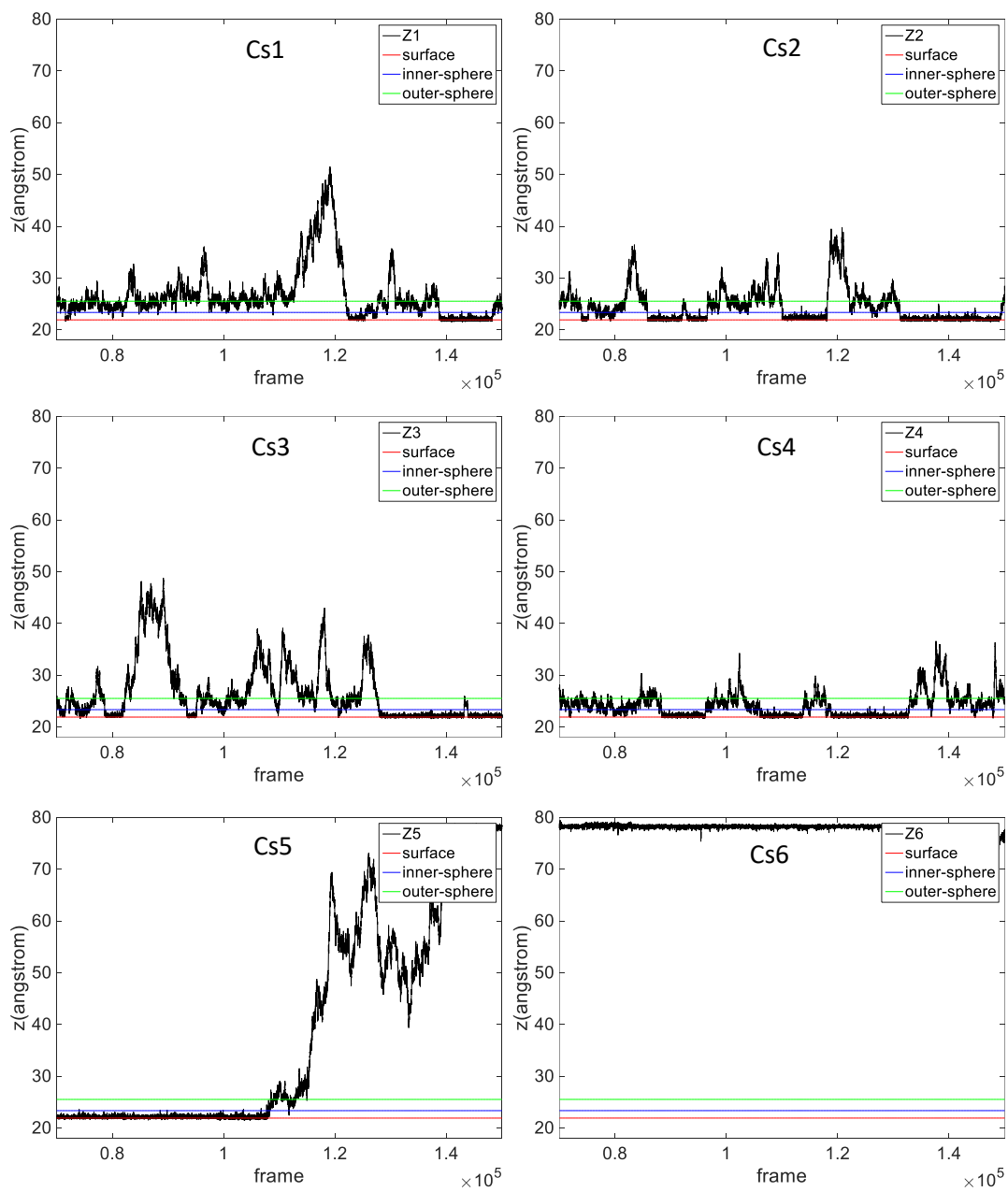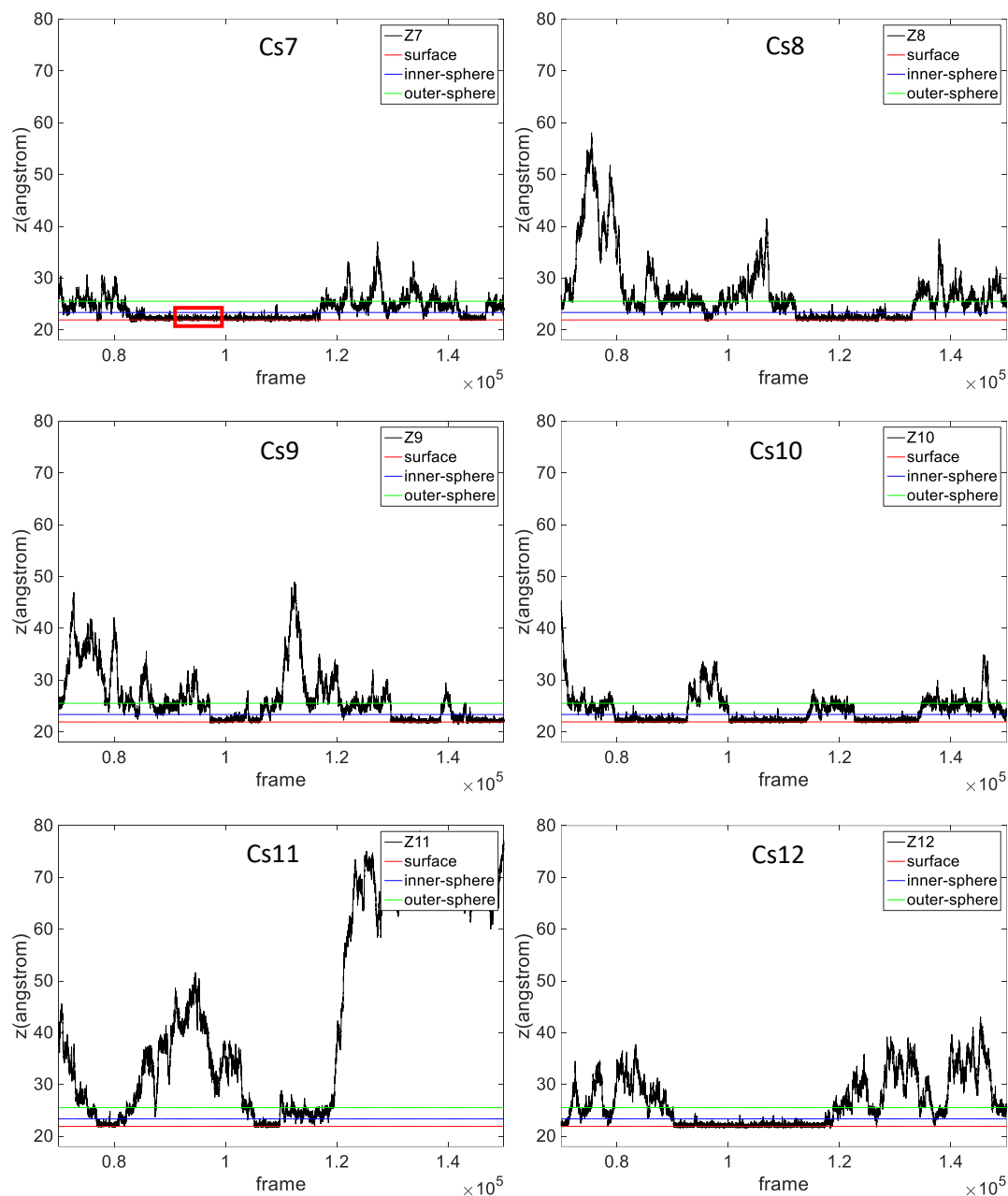
Figure 3.9. The residence time of each Cs^+ ions in inner-sphere and outer-sphere regions at the tetrahedral SiO_4 surface of 9Å tobermorite, as derived from the z-coordinates of Cs^+ ions during the data collection. The Cs^+ ions were numerically labeled, as shown in the legend (*e.g.*, Cs7 represents the 7th Cs^+ ion, Z7 represents the z-coordinates of the 7th Cs^+ ion, one of the stable events was highlighted).

Table 3.1. The duration of Cs^+ ions adsorbed as stable inner-sphere complexes and outer-sphere complexes on the tetrahedral SiO_4 surface of 9Å tobermorite, and diffuse ions in the bulk solution.

Cs^+ ions index	Inner-sphere period (frame number, >5000 frames)	Outer-sphere period (frame number, >2500 frames)	Diffuse ion (frame number, >5000 frames)
Z1	N/A	72500-75000(~0.25ns), 78500-81000(~0.25ns)	112502-120001(0.7ns)
Z2	131181-138079(0.6ns)	N/A	N/A
Z3	127913-143194(1.5ns), 143868-150001(0.6ns)	N/A	83144-91037(0.7ns), 104028-109159(0.5ns)
Z4	88313-96281(0.7ns), 108598-113755(0.5ns), 118790-125363 (0.6ns)	72500-75000(~0.25ns), 145000-148000(~0.3ns)	N/A
Z5	74038-88579(1.4ns), 89840-99891(1.0ns)	N/A	114959-139063(2.4ns)
Z6	N/A	N/A	N/A
Z7	90020-98415(0.8ns), 109247-115661(0.6ns)	138000-141000(~0.3ns)	N/A
Z8	N/A	N/A	72074-81243(0.9ns)
Z9	133459-138677(0.5ns), 122956-131255(0.8ns)	87000-89500(~0.25ns)	70958-78312(0.8ns)
Z10	108948-114460(0.5ns), 122956-131255(0.8ns)	146800-149300(~0.25ns)	N/A
Z11	N/A	116500-119000(~0.25ns),	70000-75086(0.5ns), 87454-103001(1.5ns), 118807-130025(1.0ns)
Z12	94190-102075(0.7ns), 112270-117774(0.5ns)	N/A	79543-85239(0.5ns), 127758-134002(0.6ns), 139317-147419(0.8ns)

N/A: not available
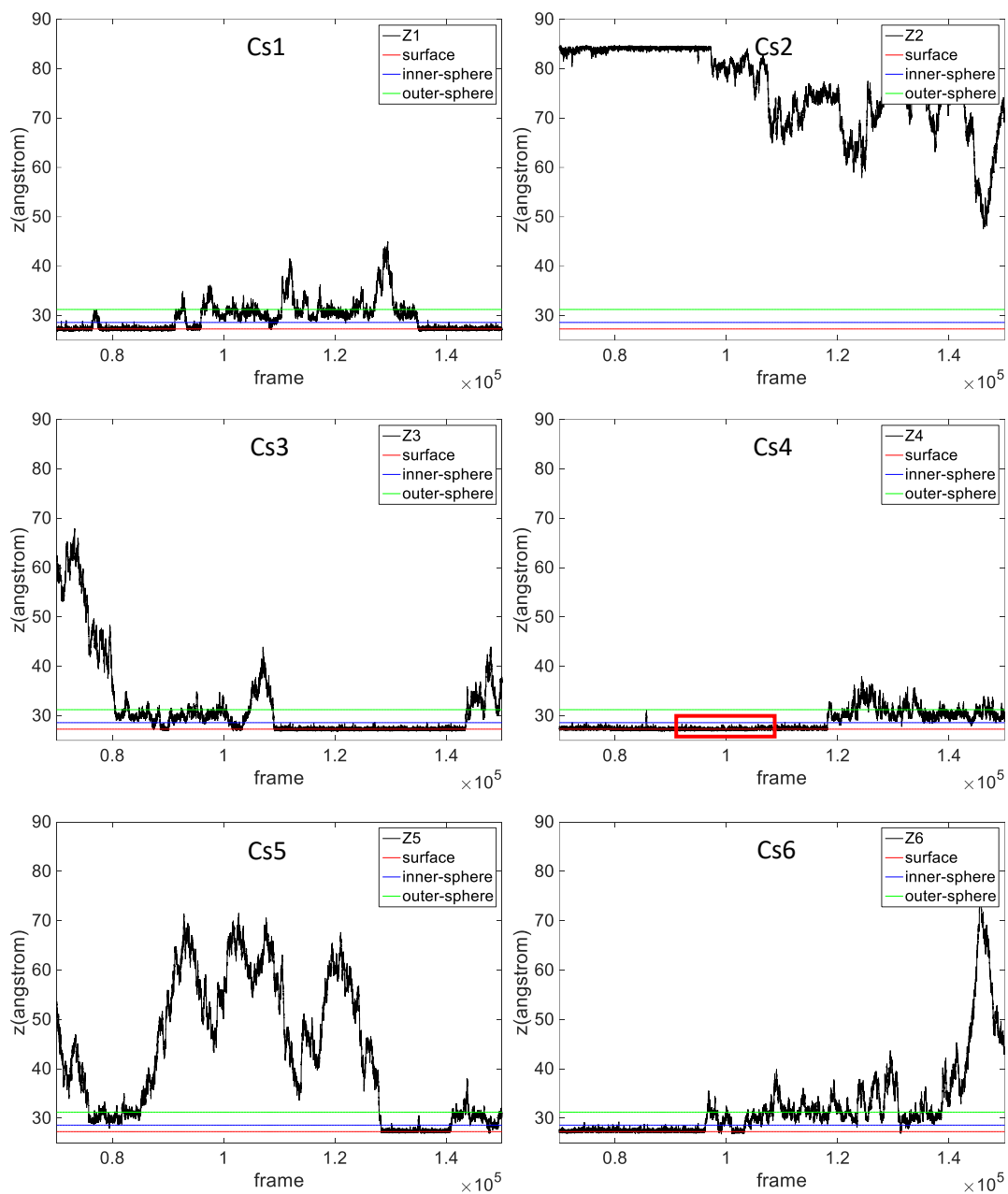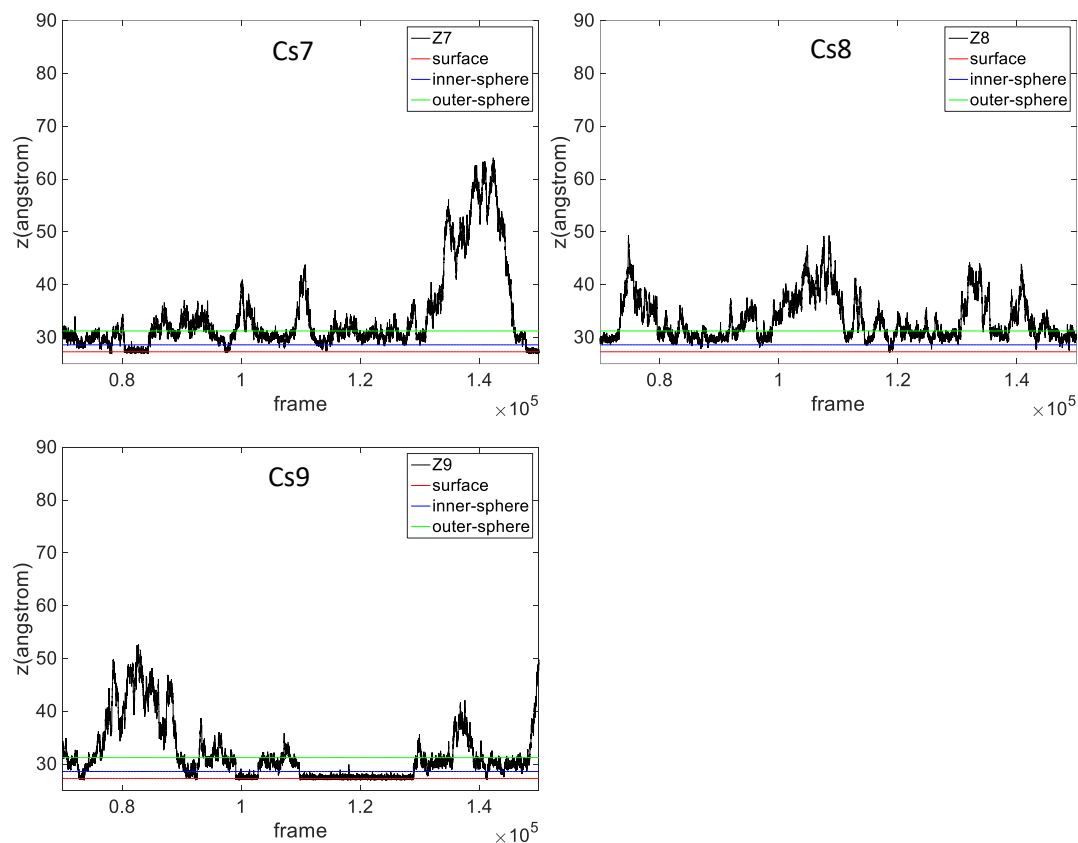
Figure 3.10. The residence time of each Cs^+ ions in inner-sphere and outer-sphere regions at the tetrahedral SiO_4 surface of 14Å tobermorite was derived from the z-coordinates of Cs^+ ions during the data collection. The Cs^+ ions were numerically labeled, as shown in the legend (*e.g.*, Cs4 represents the 4th Cs^+ ion, Z4 represents the z-coordinates of the 4th Cs^+ ion, one of the stable events was highlighted).
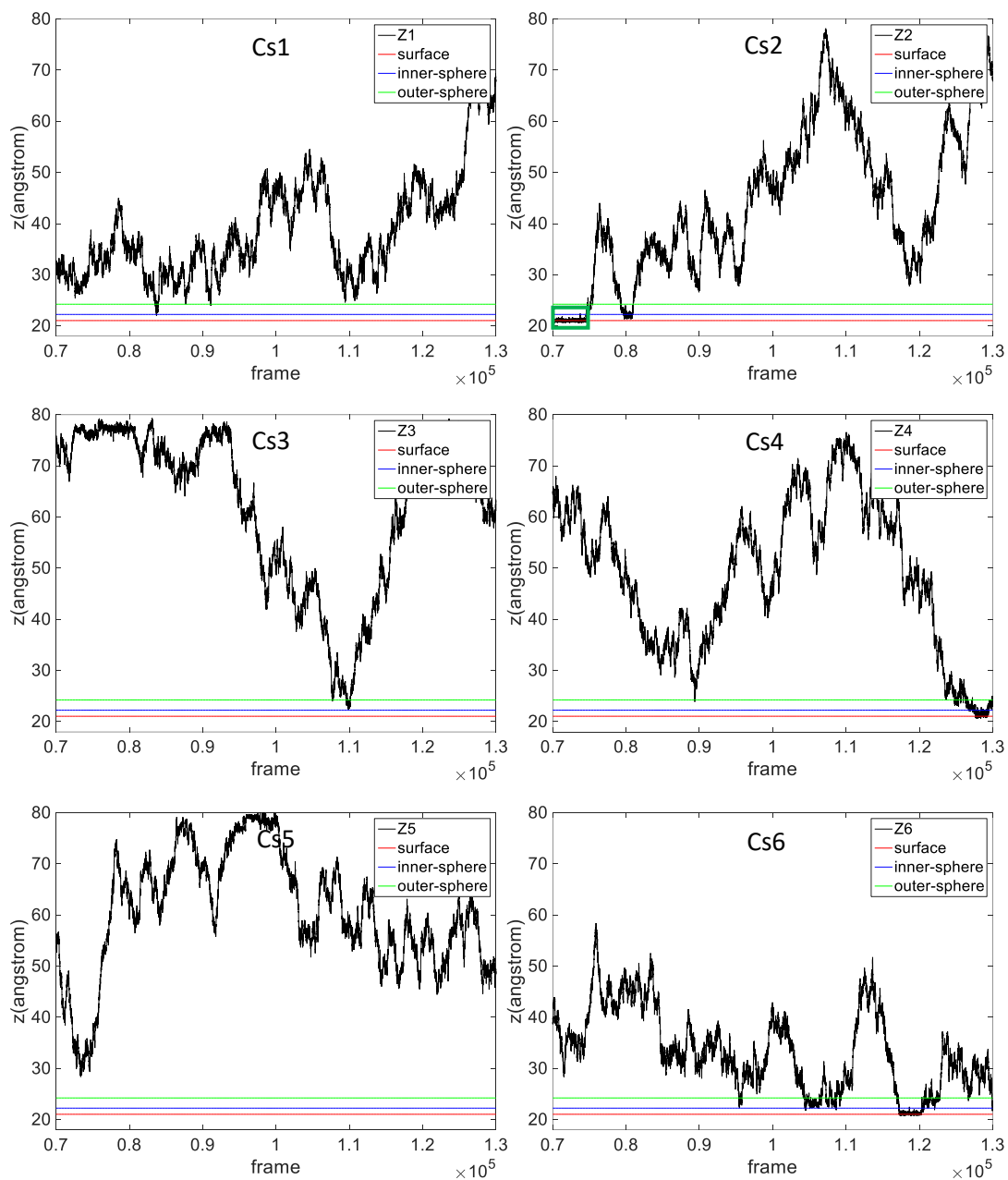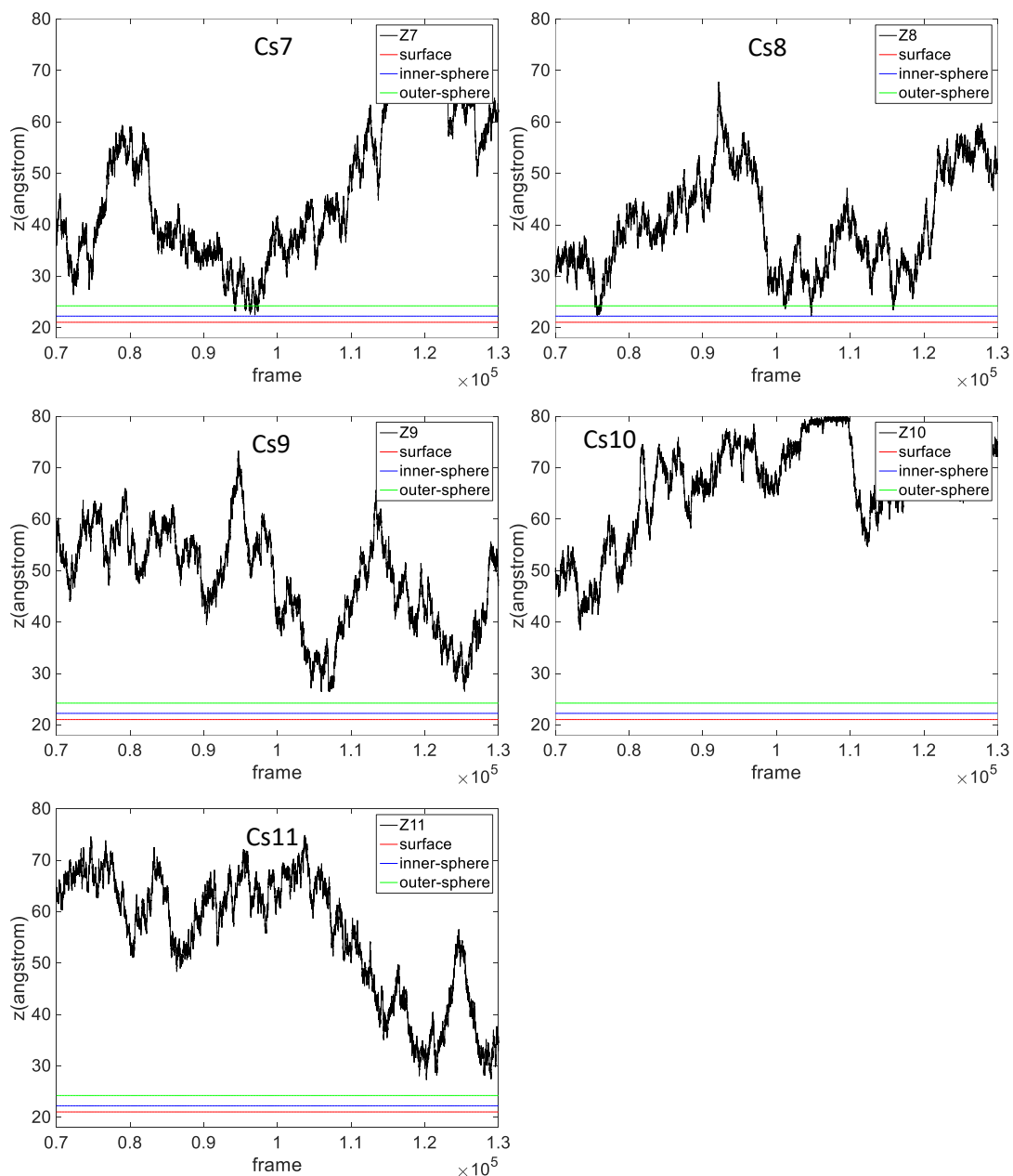
Figure 3.11. The residence time of each Cs$^+$ ion in inner-sphere and outer-sphere regions at the tetrahedral SiO$_4$ surface of jennite was derived from the z-coordinates of Cs$^+$ ions during the data collection. The Cs$^+$ ions were numerically labeled, as shown in the legend (*e.g.*, Cs2 represents the 2nd Cs$^+$ ion, Z2 represents the z-coordinates of the 2nd Cs$^+$ ion, no stable adsorption event was observed. One inner-sphere interaction event was highlighted with a green box, this event was used to calculate inner-sphere interaction energy).
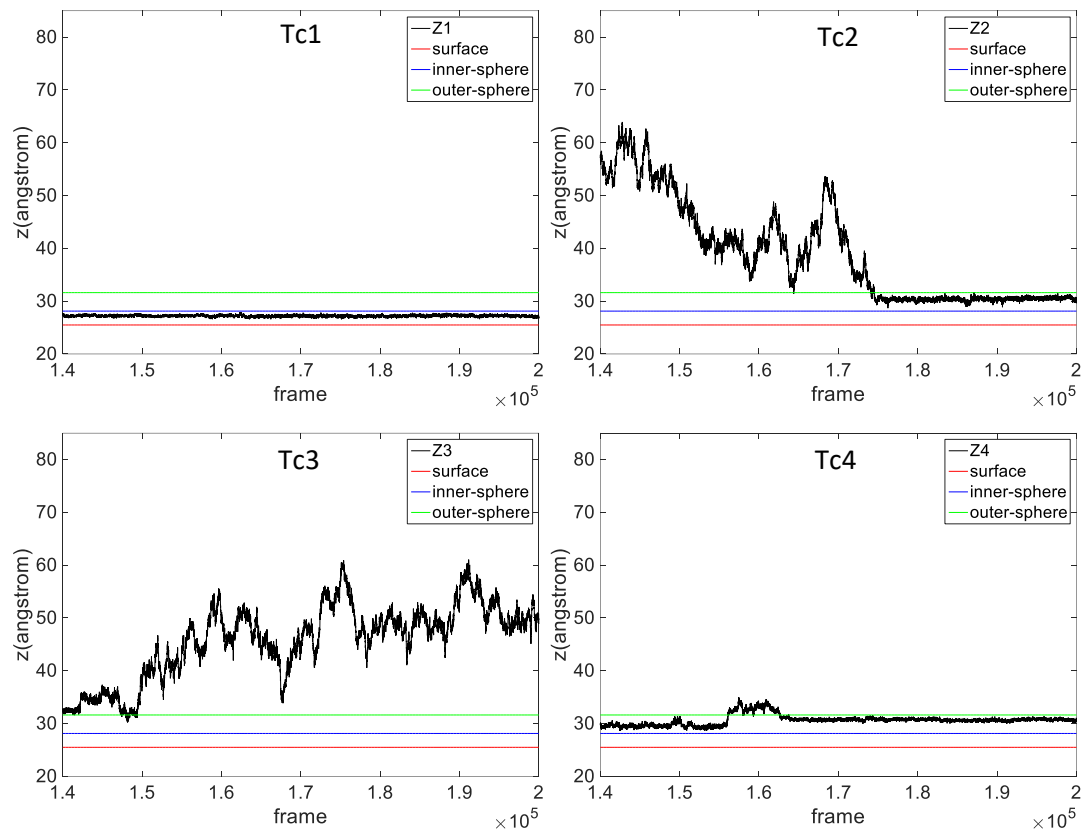
Figure 3.12. The residence time of Tc^{7+} in inner-sphere and outer-sphere regions at the octahedral CaO_6 surface of 14Å tobermorite was derived from the z-coordinates of Tc^{7+} ions during the data collection. The Tc^{7+} ions were numerically labeled, as shown in the legend (*e.g.*, Tc4 represents the 4th Tc^{7+} ion, Z4 represents the z-coordinates of the 4th Tc^{7+} ion).

45
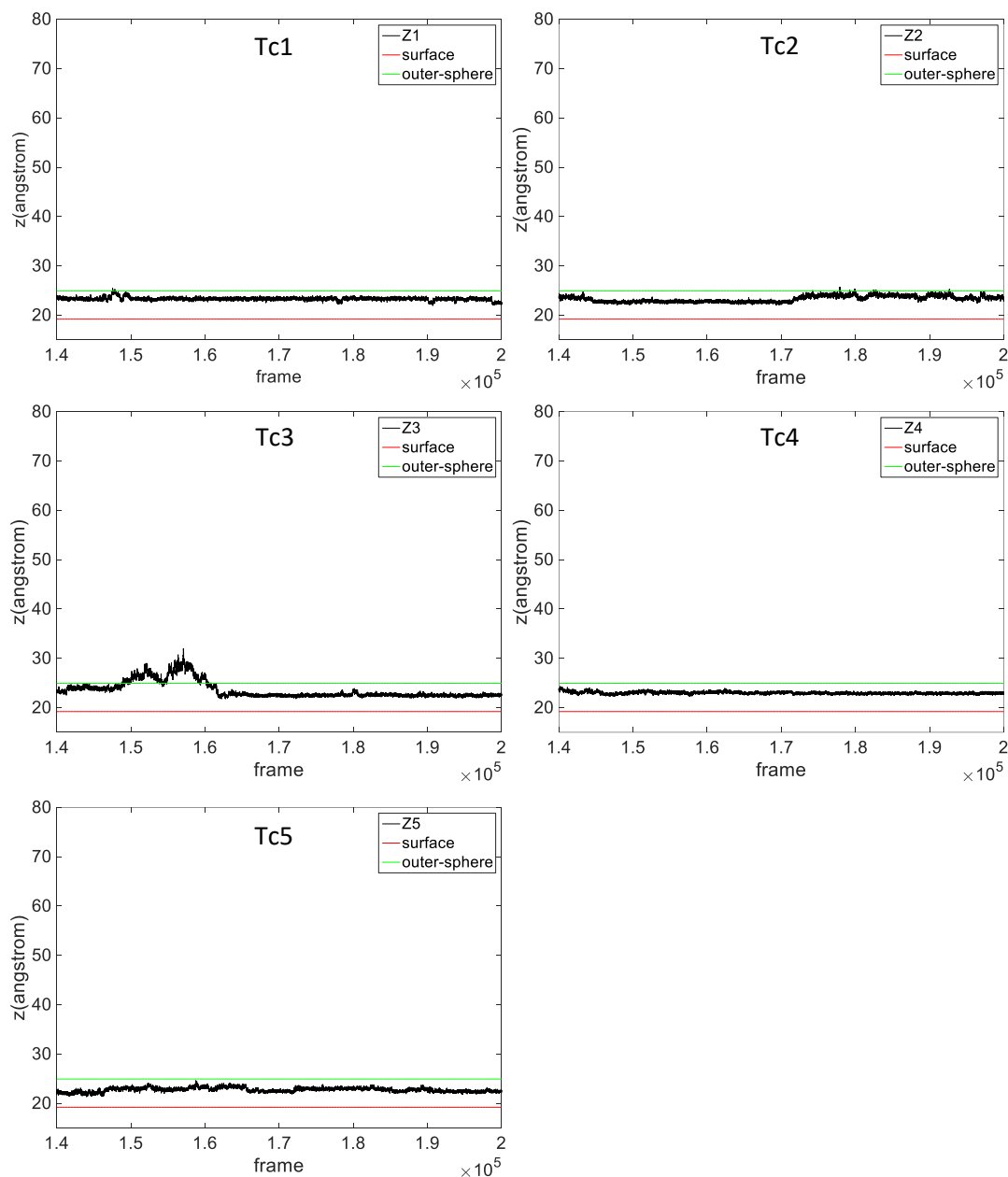
Figure 3.13. The residence time of Tc^{7+} in inner-sphere and outer-sphere regions at the octahedral CaO_6 surface of ettringite was derived from the z-coordinates of Tc^{7+} ions during the data collection. The Tc^{7+} ions were numerically labeled, as shown in the legend (*e.g.*, Tc4 represents the 4th Tc^{7+} ion, Z4 represents the z-coordinates of the 4th Tc^{7+} ion).
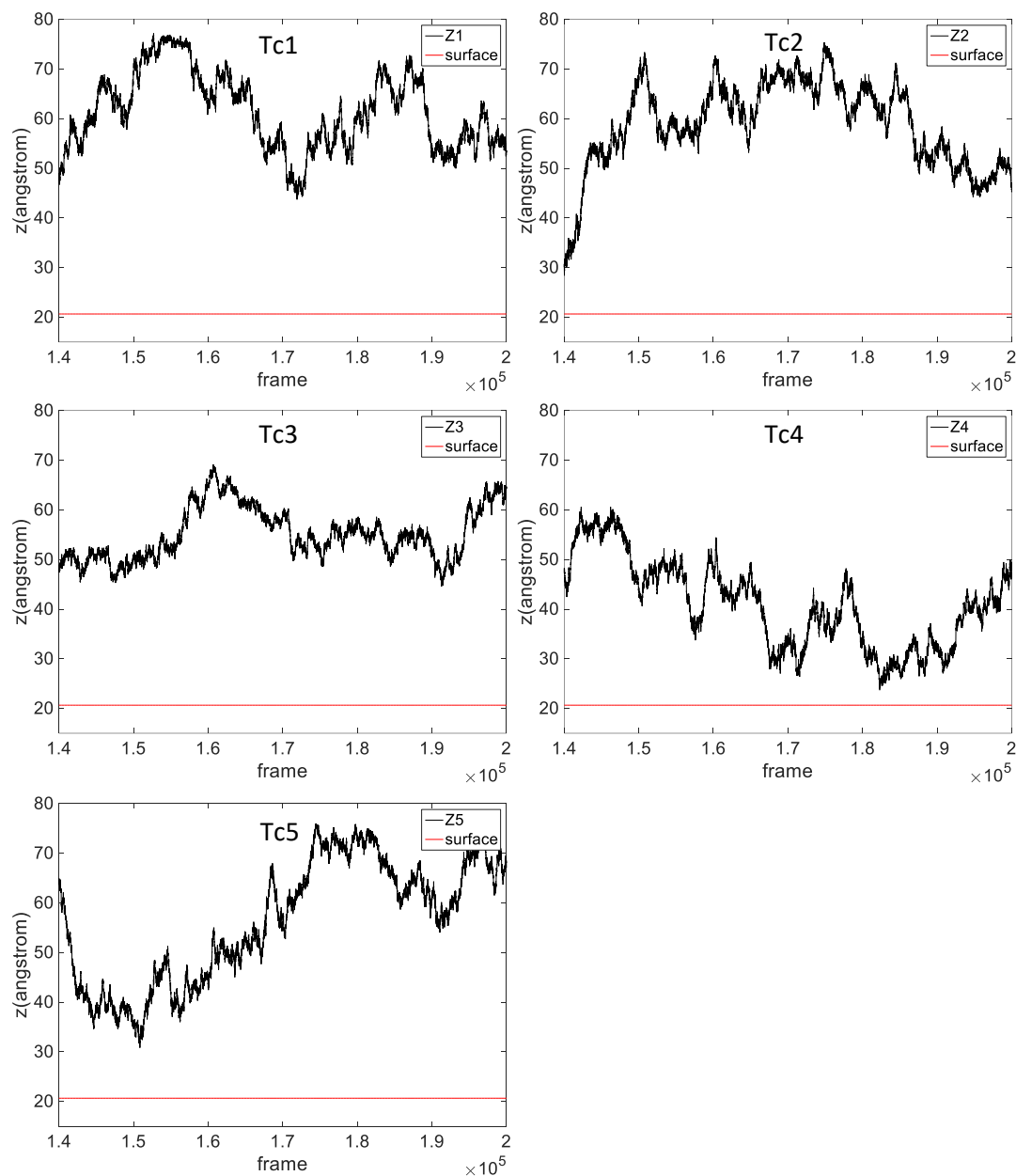
Figure 3.14. The residence time of Tc^{7+} in inner-sphere and outer-sphere regions at the octahedral CaO_6 surface of jennite was derived from the z-coordinates of Tc^{7+} ions during the data collection. The Tc^{7+} ions were numerically labeled, as shown in the legend (*e.g.*, Tc4 represents the 4th Tc^{7+} ion, Z4 represents the z-coordinates of the 4th Tc^{7+} ion).

3.7   Adsorption Energy Evaluation

The calculation of the adsorption energy was computationally expensive. For statistical reliability, a 1-ns inner-sphere adsorption event was sampled, and the adsorption energy was calculated for each frame. Over this period of data collection, 10,000 points were collected. To determine how many points must be sampled from this data set to yield a representative population, a series of Monte Carlo analyses were performed for this data set. A 100 out of 10,000 points sampling strategy was proposed. Monte Carlo analyses were performed by randomly sampling 100 points from this data set for 10,000 times. For the adsorption of Cs^+ or TcO_4^- ions on surface of cement phases, the results indicated that for all the random samplings, the difference of the average of each random sampling comparing to the overall averaged interaction energy ranged from 1% to 10% (Figure 3.15, Figure 3.16 and Figure 3.17). The combination of the averaged value and standard deviation for a random sampling can well represent the overall data. Therefore, for each stable adsorption event, the inner-sphere adsorption energy was calculated every 10 ps (*i.e.* every 100 frames) and the corresponding standard deviation was calculated. This procedure was performed for every qualified event; then the overall inner-sphere adsorption energy was averaged from all the qualified events and corresponding standard deviation was calculated.
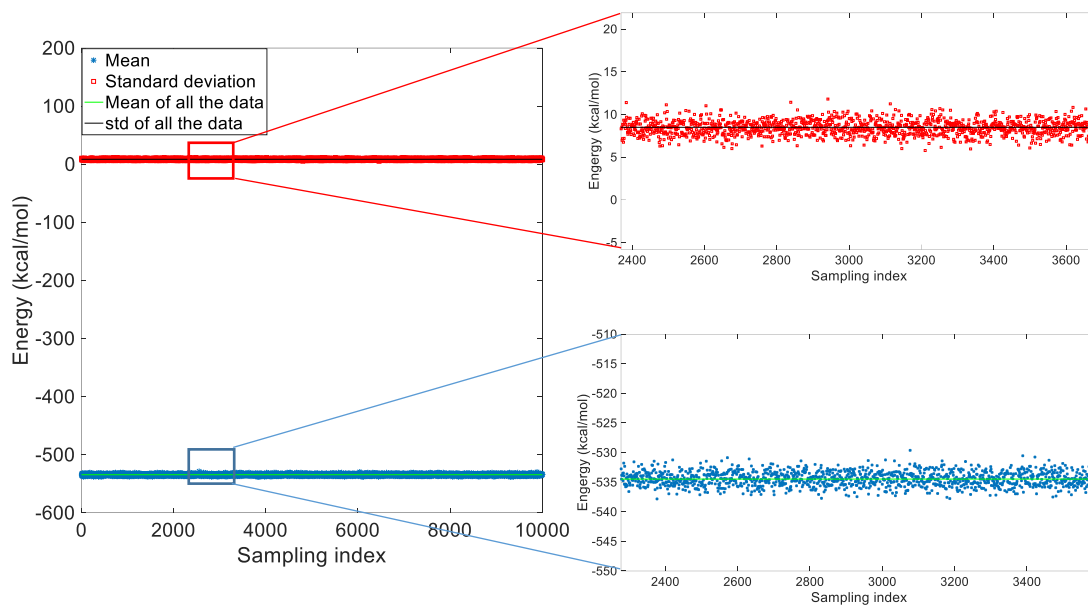
Figure 3.15. Monte Carlo analysis for the inner-sphere adsorption energies and corresponding standard deviation of one inner-sphere adsorption event of 0.5M CsCl/9Å tobermorite.
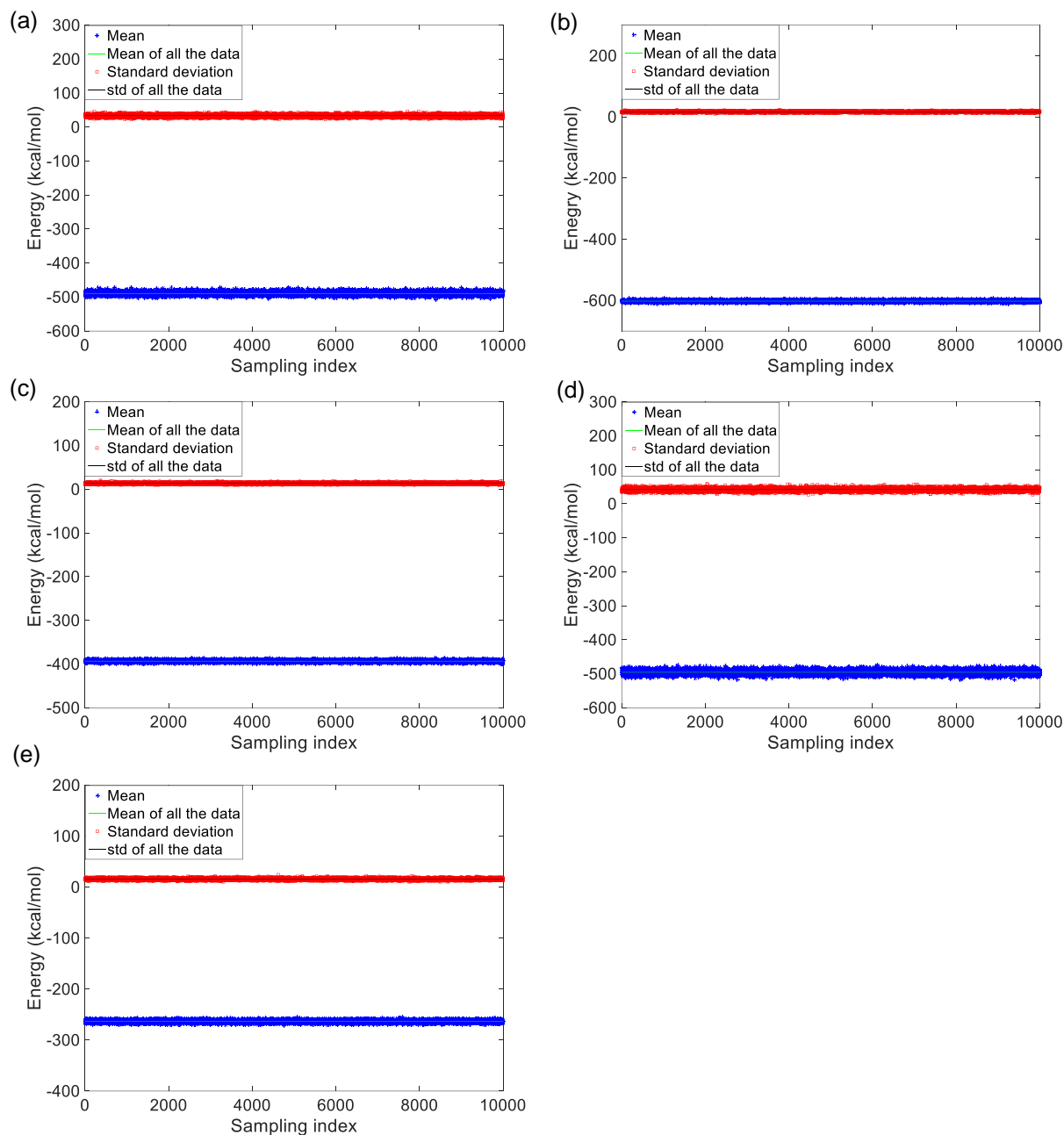
Figure 3.16. Monte Carlo analysis for the adsorption energies of TcO$_4^-$ ions and corresponding standard deviation of one adsorption event on the surface of 14Å tobermorite: (a) inner-sphere adsorption before co-ion adsorption; (b) inner-sphere adsorption after co-ion adsorption; (c) outer-sphere adsorption type 1 before co-ion adsorption; (d) outer-sphere adsorption type 1 after co-ion adsorption; (e) outer-sphere adsorption type 2.
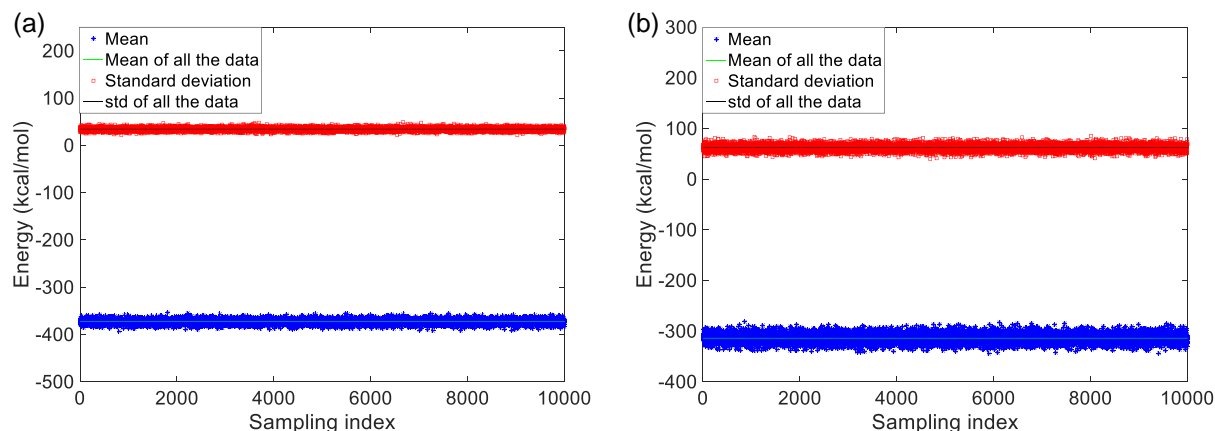
Figure 3.17. Monte Carlo analysis for the adsorption energies of TcO_4^- ions and corresponding standard deviation of one adsorption event on the surface of ettringite: (a) outer-sphere adsorption type 1 and (b) outer-sphere adsorption type 2.

3.8   Summary and Conclusion

Relative atomic density profiles and adsorption densities were calculated from all equilibrated data acquisition trajectories (*i.e.* the last 6-8 ns of trajectories). Most of the other calculations (*i.e.* adsorption energy, radial distribution function, coordination number, and diffusion coefficient) were performed on individual stable adsorption events, and averaged values were presented as final data. Detailed methods are summarized in the following table:

Table 3.2. Data analysis methods.

Data analysis	Methods
Convergence to equilibrium	▪ RMSD and interval adsorption density were calculated over the entire data acquisition trajectory. The interval adsorption densities were plotted every 1 ns of trajectory. ▪ The adsorption was considered to converge when the RMSD of ions plateaued and the interval adsorption density did not significantly increase or decrease within these time frames. ▪ To ensure statistical reliability, the plateau of RMSD and the stability of interval adsorption density had to last for at least 5 ns. ▪ The last 6-8 ns of trajectories for each system were collected for subsequent analysis.
Relative atomic density profiles	▪ Relative atomic density profiles were averaged over the last 6-8 ns of trajectories for each system.

Adsorption density (number of ions per unit surface area)	▪ Adsorption density was integrated from the relative atomic density profiles for adsorbed ions.
Contour maps	▪ Contour maps for interfacial atoms were calculated from the last 1 ns trajectory during the equilibrium trajectories.
Adsorption energy	▪ Data analysis was performed for each qualified event, the averaged value for all the events were presented as final data, standard deviation was calculated if necessary.
Radial distribution function (RDF)	
Coordination number (CN)	
Diffusion coefficients	
Local structure analysis (bond length, angle, dipole moment)	
Water orientation	▪ Water orientation was calculated for all water molecules located 20Å above (*i.e.* from the surface up to 20Å)
Hydration energy	▪ A cell of the same size with the liquid phase was built using only water molecules and one ion. The hydration energy was calculated by a module of Materials Studio, convergence was met.

This chapter discussed the methods employed in the present work for MD simulations, particularly the evaluation of equilibrium and the methods used for data analysis. The MD simulations were performed long enough (13 ns to 20 ns) to reach equilibrium, and the amount of trajectory collected (6 ns to 8 ns) for data analysis was able to guarantee statistical reliability. Data analysis was performed on stable adsorption events to make sure that the final results were accurate and representative.

CHAPTER 4

4   The Adsorption of Cs$^+$ Ions on the Surfaces of Crystalline C-S-H Phases

This chapter is planned to be submitted for peer-review publication.

4.1   Overview

^{137}Cs is a fission product readily produced in the nuclear fuel cycle. The high solubility, high decay energy (where ^{137m}Ba emits γ-rays, and it is a decay product of ^{137}Cs), and high chemical reactivity of ^{137}Cs make it one of the most problematic constituents of nuclear waste [4]. One of the methods for safely disposing ^{137}Cs is to immobilize it with cementitious materials, mainly conventional Portland cement [170]. Preventing ^{137}Cs release from closed waste tanks requires a deep understanding of the nature of its association with the waste solids and waste form.

The most important component of hydrated Portland cement is C-S-H. C-S-H is an amorphous and porous material, although experimental results from different techniques such as ^{29}Si nuclear magnetic resonance (NMR), X-ray diffraction (XRD), and infrared (IR) studies [65,171–173] revealed that C-S-H has a short range ordered structure at the atomistic scale. Most knowledge regarding the C-S-H gel has been gained from its comparison with fully crystalline calcium silicate hydrates such as 14 Å tobermorite and jennite. 14 Å tobermorite is composed of calcium oxide layers ribbed on both sides by silicate chains forming a layered structure, with water molecules and extra Ca ions in the interlaminar space [78]. The structure of jennite is similar to that of tobermorite with two main differences. First, in jennite the bridging tetrahedral of the silicate chains is also connected to the calcium oxide layer. Second, only half of the Ca^{2+} atoms in jennite are linked to the oxygen of the silicate groups while the rest are coordinated to hydroxyl groups from the calcium oxide layer [79]. Beyond the 14Å tobermorite and jennite, 9Å tobermorite [80] has also been widely accepted as a useful model to study the amorphous C-S-H gel [13]. 9Å tobermorite has a similar crystalline structure to 14Å tobermorite, but with two main differences: 1) the basal space between two complex layers is 9Å and 2) 9Å tobermorite does not contain interlayer water molecules. These three structures were used as models for crystalline C-S-H phases in the present work.

C-S-H plays an important role in the interaction between cement paste and Cs^+ ions. Experimental data (*e.g.* X-ray microanalysis [17] and NMR [103,104]) indicated that that Cs^+ was highly adsorbed on C-S-H [103,104] in hydrated PC. A variety of interaction mechanisms were suggested. Some researchers suggested physical entrapment of Cs^+ ions in the C-S-H intermolecular channels due to the amorphous property of C-S-H [22]. Other suggested interaction mechanisms between C-S-H and Cs^+ ions included substitution in the interlayer sites [68,101,102]; direct interaction with the oxygen atoms carried by the bridging silicon and generation of the inner-sphere complexes [103,104]; shortening of silicate chains in C-S-H gel [67]; particularly, electrostatic interactions (*i.e.* an ion-exchange process) between Cs^+ ions and alkali ions (Na^+, K^+) on negatively charged sites [100] or acidic silanol (Si–OH) sites [8,14,17,18].

The interactions between Cs^+ ions and crystalline C-S-H phases have rarely been addressed. Batch sorption experiments indicated that 14Å tobermorite exhibited a small ion exchange capacity with Cs^+ ions [12]. The Cs^+ exchange distribution coefficient (K_d) was small (10 meq/100 g), and the uptake of Cs^+ ions by 14Å tobermorite resulted from the exchange of protons from broken bonds of silicate chains.

The fate of radioactive wastes in the environment is related to the capability of natural/synthetic phases to immobilize contaminants and decrease the concentration in the liquid phase in contact with wasteform. A fundamental atomic-level understanding of these phenomena can be provided by Molecular Dynamic (MD) simulations. Although 9Å tobermorite, 14Å tobermorite, and jennite have been studied using MD simulations, previous studies mainly focused on structural and mechanical properties of these cement phases [113–122]. Those studies concerning dynamic properties either focused on the interactions between cement phases and other ions or molecules, such as Na^+, Sr^{2+} ions, and H_2O molecules [13,35–37,123,124], or used forcefields other than the ClayFF forcefield used in this work [117,118,125,126]. The results in previous studies indicated that tobermorites and jennite were capable of adsorbing some ions. Alkali ions such as Na^+ and K^+ ions can be adsorbed both on the surface and penetrate into the silicate channels of 9Å tobermorite and jennite to interact with different structure oxygen, and the interactions in the silicate channels were suggested to be chemical bonding [35].

MD simulation has been used to study the interfacial adsorption mechanisms between crystalline C-S-H phases and other ions [35–37,124], such as Na^+, Sr^{2+}, etc. The principal focus

here is on investigating the adsorption mechanisms of Cs^+ ions on three different crystalline C-S-H phases: 9Å tobermorite, 14Å tobermorite, and jennite. The molecular-scale energetic, structural, and dynamic properties of the interface between an aqueous solution containing CsCl and crystalline calcium-silicate-hydrate (C-S-H) phases were analyzed using relative atomic density profiles, radial distribution function (RDF), coordination number (CN), atomic density contour maps, diffusion coefficient, adsorption energy and hydration energy.

4.2   Computational Methods

4.2.1   Simulation Models and Computational Cells

The crystalline C-S-H structures (*i.e.*, 9Å tobermorite, 14Å tobermorite, and jennite) were modeled according to the widely used unit cell models proposed by Merlino *et al*. [80] and Bonaccorsi *et al.* [78,79], respectively. Each crystalline C-S-H structure (

Table 4.1) was cleaved along the (0 0 1) and (0 0 -1) crystallographic directions to produce two solid surfaces: the tetrahedral SiO_4 surface and the octahedral CaO_6 surface. To simulate the interfacial interactions between the two crystalline C-S-H solid surfaces and the 0.5M CsCl aqueous solution, two layers of geometrically optimized crystalline C-S-H structures separated by a 50Å thick vacuum layer between the tetrahedral SiO_4 surface and the octahedral CaO_6 surface were used to build the different computational cells (Table 4.2). The thickness of the layer between adjacent crystalline C-S-H planes was sufficiently large to effectively exclude direct interaction of one crystalline C-S-H solid surface with another and preclude the effects of small confined spaces. Water molecules, Cs^+ ions, and Cl^- ions were then packed into the vacuum layer to create the 0.5M CsCl solution (Table 4.3). The concentrations of ^{137}Cs in tanks of Hanford site ranged between 0.02 and 0.19 mM [45], which were several orders of magnitude lower than the concentration simulated in present work. The much higher concentration was chosen because one of the purposes of present work was to study the adsorption capacity of crystalline C-S-H phases. CsCl solution was designed to saturate the adsorption sites to ensure that all interaction mechanisms could be observed (*i.e.* inner-sphere and outer-sphere adsorption). In all cases, the Cs^+ and Cl^- ions were initially positioned away from the surfaces at the middle plane of the liquid phase (*i.e.* ~25Å away from the surfaces) (Figure 4.1). Periodic boundary conditions were applied along the three space dimensions.

Table 4.1. Crystallographic lattice parameters of the supercells constructed for the crystalline C-S-H structures.

	9Å tobermorite	14Å tobermorite	jennite
a/ Å	22.31	26.94	31.73
b/ Å	29.21	29.70	21.78
c/ Å	21.71	27.99	21.86
α/deg	101.08	90.0	101.3
β/deg	92.83	90.0	96.98
γ/deg	89.98	123.25	109.65

Table 4.2. Crystallographic lattice parameters of the C-S-H structures/liquid phase simulation cells.

	a/Å	b/Å	c/Å	α/deg	β/deg	γ/deg
0.5M CsCl/jennite	31.9	21.9	103.9	101.3	96.98	109.65
0.5M CsCl/9Å tobermorite	22.3	29.2	100.5	101.08	92.83	89.98
0.5M CsCl/14Å tobermorite	20.0	29.4	109.5	90.0	90.0	123.25

Table 4.3. CsCl solution details.

	Concentration (M)	Density[a] (g/cm^3)	Number of Cs$^+$	Number of Cl$^-$	Number of H$_2$O
9Å tobermorite	0.5	1.062	12	12	1274
14Å tobermorite	0.5	1.062	9	9	925
jennite	0.5	1.062	11	11	1230

[a][21]
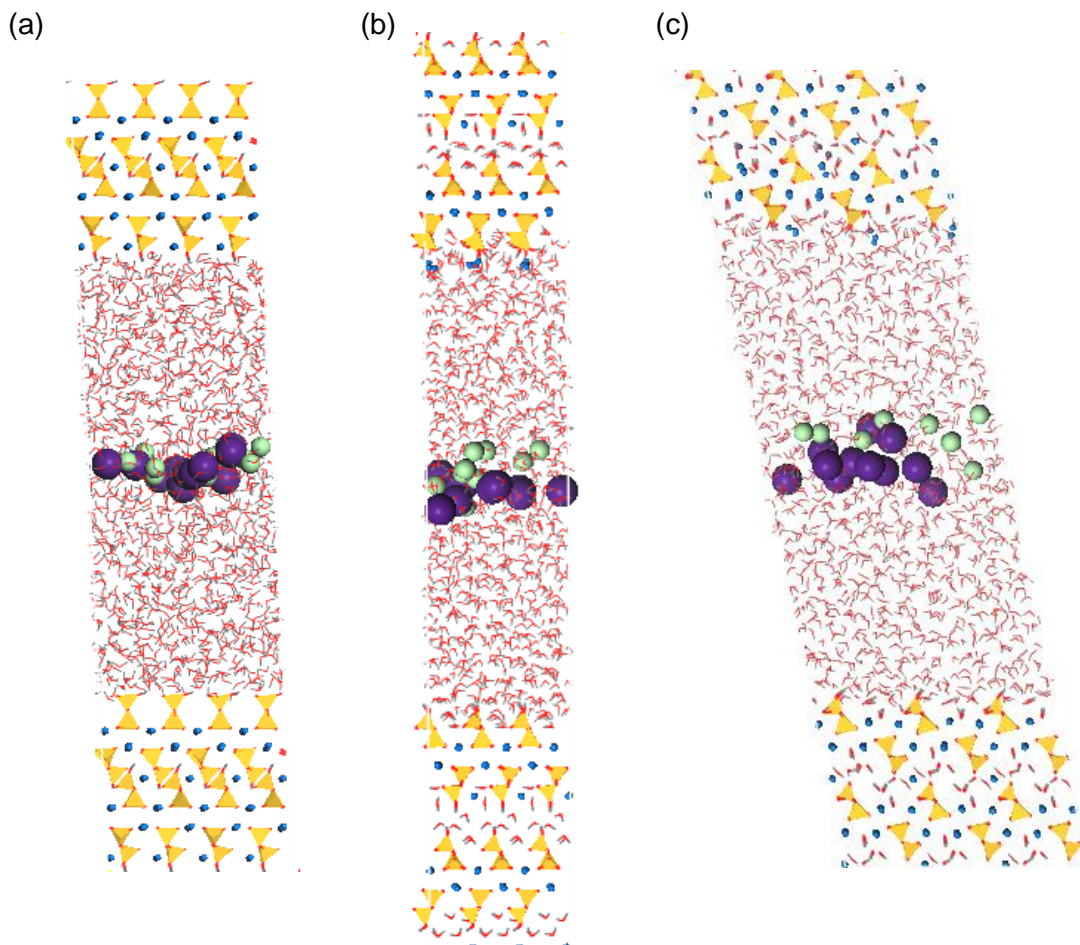
Figure 4.1. MD simulation cell of the geometry optimized configuration of: (a) 9Å tobermorite; (b) 14Å tobermorite; (c) jennite in contact with CsCl 0.5M solution. Purple balls: Cs^+ cations; green balls: Cl^- anions; yellow tetrahedral: Si; red lines: O; Grey lines: H; blue balls: Ca.

4.2.2   *Forcefield*

The CLAYFF forcefield [126] was used to describe the atomic interactions in the three crystalline C-S-H structures and their interactions with the different aqueous solutions. The uniqueness of this forcefield is in the treatment of metal-oxygen interactions as nonbonded interactions; the only bonded interactions explicitly defined are the water and hydroxyl interactions. This forcefield has been successfully used in the literature to model the structure and dynamic properties of hydrated mineral systems and their interfaces with aqueous solutions, including solutions containing Cs^+ or Cl^- ions [13,169] and has been demonstrated to be suitable for tobermorites and jennite [36,122,124,174].

4.2.3 MD Simulations

MD simulations were performed using Materials Studio 7.0 (Biovia, Inc., San Diego, CA). After geometry optimization of each constructed computational cell, 400 ps of NPT-ensemble MD simulations were employed to relax the computational cell. A portion of the solid structure located 6Å below the interface was then constrained and maintained fixed during the simulation. The solid phase was partially constrained to decrease the simulation time. Meanwhile, the impact of interfacial interaction on the surface structure could be investigated with the free near surface solid layer method. Each energy minimized computational cell was then subjected to an NVT-ensemble of MD simulations of 1,000 ps with a time step of 1.0 femtosecond (fs) at 298K for thermodynamic equilibration. The Nosé-Hoover-Langevin (NHL) thermostat was used to keep the temperature constant. The cut-off distance for non-bond energy was 9.5Å. The dynamic trajectory was then recorded at 100-fs intervals for an additional 13 ns of NVT-ensemble MD simulation for jennite structure (where Cs^+ ions had weak affinity to jennite, so that smaller amount of trajectory was collected for further data analysis), and 15 ns of NVT-ensemble MD for 9Å tobermorite and 14Å tobermorite structures.

4.2.4 Data Analysis

4.2.4.1 Convergence of Equilibrium

The equilibration status of each trajectory was evaluated by calculating the Root Mean Square Displacement (RMSD) [149–153] of the atoms located in the first layer of the solid surface and the ions (*i.e.* Cs^+ and Cl^- ions) in the solution. Particularly, the RMSD on the *z*-direction was evaluated, because movement of ions in the *z*-direction are associated with the adsorption-desorption process. The first layer atoms on the SiO_4 surfaces included all the hydroxyl oxygen, bridging oxygen with tetrahedral substitution, and silica ions at the surface in the first layer of silicate chains, as well as O in the interlayer water molecules and hydroxyl groups at the interface for 14Å tobermorite and jennite models. The first layer atoms on the CaO_6 surfaces included all the hydroxyl oxygen, bridging oxygen with tetrahedral substitution and silica atoms at the surface in the first layer of silicate chains, and interlayer Ca ions at the surface for all the three models. For 0.5M CsCl/14Å tobermorite, the first layer of atoms also included O in the interlayer water molecules. For 0.5M CsCl/jennite, the first layer of atoms also included O in the interlayer water molecules and hydroxyl groups at the interface. The equilibration of the interface was determined by the plateau of the RMSD curves in the *z*-direction. The systems were assumed to have reached

equilibrium before the end of the simulation (*i.e.* the final part of each RMSD curve was assumed to be part of a plateau that could be represented as a mean with random error). The data acquisition trajectories were segmented to a series of 1-ns segments (10,000 frames) at a running 0.1-ns interval (1,000 frames) from the end of the simulation (where equilibrium was assumed) back to the beginning. This process generated 140 or 120 piece-wise trajectory segments that overlapped (*i.e.* 140 for tobermorite models and 120 for jennite model). The interval mean was calculated for each trajectory segment (*i.e.* 10,000 points). The running mean (*i.e.* the mean calculated from the last frame of the data acquisition trajectory to the first frame of the selected trajectory segment) was compared to the interval mean, up to the last crossover point between the running mean curve and the raw RMSD curve. The last crossover point (relative to the end of the simulation) was assumed to represent the approximate beginning of the plateau. Typically, a statistical test on the difference in means (running versus interval) was used to identify the beginning of the plateau (*i.e.* when the means are significantly different); however, the results of any such test (*e.g.* a t-test at a 5% significance level) would indicate that the beginning of the plateau was proximate to the selected crossover point because of the large numbers of RMSD points used to estimate the running and interval means. Furthermore, selecting the last crossover point instead of the actual beginning of the plateau that would be obtained using a statistical test would not significantly change the statistics for the plateau. The end of the trajectory segment that corresponds to the last crossover point was used to define the beginning of the plateau.

4.2.4.2 Relative Atomic Density Profiles

Relative atomic density profiles were computed along the (0 0 1) direction (*i.e.* perpendicular to the solid/aqueous solution interface) to define inner-sphere and outer-sphere areas beyond the interface and to quantitatively analyze the structure of the interfaces. Relative atomic density profiles were averaged over the equilibrated phase of trajectories. The interactions of Cs^+ ions and associated Cl^- ions with the tobermorite and jennite surfaces were analyzed in terms of inner-sphere and outer-sphere adsorption. Inner-sphere adsorption was considered as the adsorption mechanism when the ions bind directly to the surface with no intervening water molecules and little mobility in the plane parallel to the surface for a long simulation period (700 ps) (where the residence time for a stable inner-sphere adsorption was 500 ps in a previous MD study [169]). Outer-sphere adsorption was characterized by the presence of intermediate water molecules between the ions and the surface and the complexes stayed in the outer-sphere region

longer than 250 ps. The inner-sphere region was defined by the first peak of Cs^+ ions beyond the surface; the outer-sphere region was defined by the second peak of Cs^+ ions. The first layer of O atoms in the solid structure was used to define the solid surface. For all three crystalline C-S-H structures, the O from the hydroxyl groups was chosen as the marker for the surface. The inner-sphere region thus corresponded to the region that was within 1-2Å from the surface and the outer-sphere region extended from the end of the inner-sphere region up to 4Å.

4.2.4.3 Atomic Density Contour Maps

Atomic density contour maps were plotted to indicate the possibility of finding ions at different locations for cross-sectional slices at various distances from the surface (*i.e. xy*-plane), and provided visual insight into the spatial correlation between the ions and the surface adsorption sites and the relative horizontal and vertical mobility of the ions.

4.2.4.4 Water Orientation

The influence of the solid surface charge on the orientation of water molecules was also examined by calculating the angles between the dipole vector of each water molecule that was located up to 20Å away from the surfaces ((0 0 1) plane) in the normal direction.

4.2.4.5 Radial Distribution Function and Coordination Number

Radial distribution functions (RDF) were calculated the along the *z*-direction between Cs^+ ions and bridging O (Cs-Ob), hydroxyl O (Cs-Oh) and bridging O with tetrahedral substitution (Cs-Obts) for stable inner-sphere complexes. RDFs were first calculated for each inner-sphere adsorption event, then overall RDFs of each pair were plotted by averaging the corresponding RDFs of each inner-sphere adsorption event. Coordination Numbers (CN) were calculated by averaging the CN within the first coordination shell (*i.e.* from 0 to the end of the first RDF peak) for each frame of inner-sphere adsorption events.

4.2.4.6 Interaction Energy and Hydration Energy

To estimate whether a complex would remain at the surface of the different crystalline C-S-H structures, the inner-sphere adsorption energies and hydration energies were calculated. Inner-sphere adsorption energy was calculated every 10 ps for each qualified inner-sphere adsorption event. Averaged inner-sphere adsorption energies and corresponding standard deviations were calculated from all the inner-sphere adsorption events. The calculation of the adsorption energy

was computationally expensive. For statistical reliability, a 1-ns inner-sphere adsorption event was sampled and the adsorption energy was calculated for each frame. Over this period of data collection, 10,000 points were collected. To determine how many points must be sampled from this data set to yield a representative population, a series of Monte Carlo sampling tests were performed for this data set. A 100 out of 10,000 points sampling strategy was selected. Monte Carlo sampling tests were performed by randomly sampling 100 points from this data set for 10,000 times. The results indicated that for 10,000 random samples of 100 points, the difference of the average of each random sampling compared to the overall averaged interaction energy was ~1%. The standard deviation was small with respect to the interaction energy (*i.e.* ~2%), which indicated that the complexes had stable structures. The averaged value for a random sampling represented well the overall data. Therefore, for each stable adsorption event, the inner-sphere adsorption energy was calculated every 10 ps (*i.e.* every 100 frames) and the corresponding standard deviation was calculated. This procedure was performed for each qualified event; then the overall inner-sphere adsorption energy was calculated from all the qualified events.

4.2.4.7 Dynamic Properties

The diffusion coefficients of stable complexes at the crystalline C-S-H surface/aqueous phase systems were calculated by the mean square displacement (MSD) to provide information about the mobility for complexes at different distances (inner-sphere region, outer-sphere region and bulk solution) from the surface. Diffusion coefficients were averaged from that of each stable adsorption or stable aqueous event, and standard deviations were calculated.

4.3   Results and Discussion

4.3.1   Convergence of Equilibrium

The equilibrium of the adsorption-desorption process at the solid-liquid interface was evaluated for all the three systems with the RMSD curves in the *z*-direction (Figure 4.2 and

Figure 4.3). The results indicated at the SiO_4 surfaces, the 0.5M CsCl/9Å tobermorite model reached equilibrium at ~6.9 ns, 0.5M CsCl/14Å tobermorite model reached equilibrium at ~3.7 ns, and 0.5M CsCl/jennite model reached equilibrium at ~4.8 ns. At the octahedral CaO_6 surface, the 0.5M CsCl/9Å tobermorite model reached equilibrium at ~3.7 ns, 0.5M CsCl/14Å tobermorite model reached equilibrium at ~1.3 ns, and 0.5M CsCl/jennite model reached equilibrium at ~3.3 ns. For consistency, the last 6-8 ns of all the trajectories (8 ns for tobermorites

and 6 ns for jennite) were sampled for further structural, statistical, and dynamical analysis. The large sampling guarantees statistic reliability for data analysis.
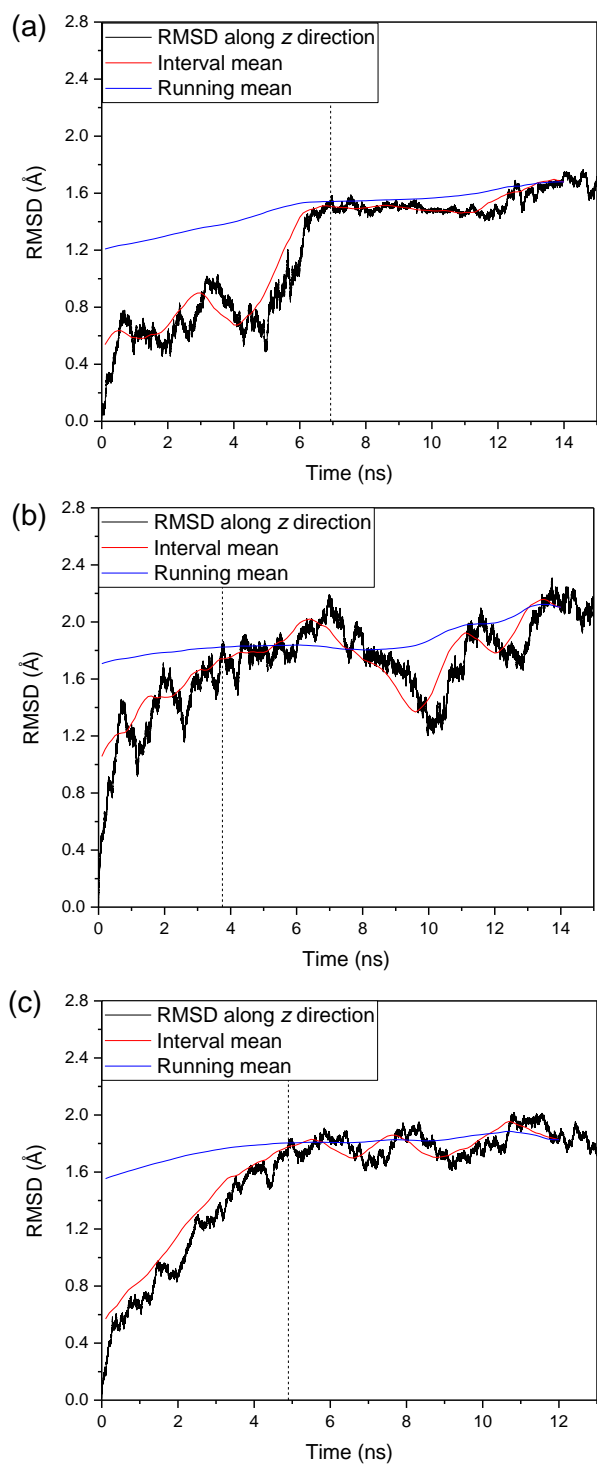
Figure 4.2. RMSD along the *z*-direction and corresponding interval mean and running mean for Cs^+ ions and the first layer of atoms on the tetrahedral SiO_4 surfaces of: (a) 9Å tobermorite, (b) 14Å tobermorite, and (c) jennite.
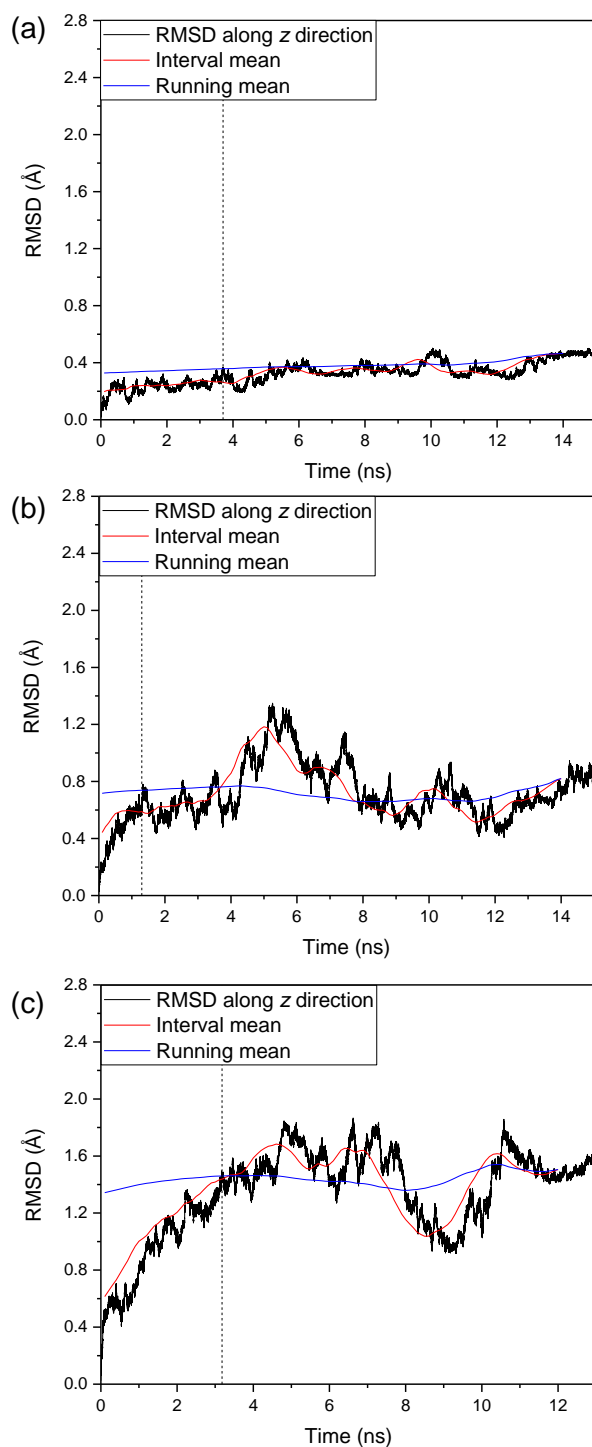
Figure 4.3. RMSD along the z direction and corresponding interval mean and running mean for Cl$^-$ ions, Cs$^+$ ions and the first layer atoms on the octahedral CaO$_6$ surfaces of: (a) 9Å tobermorite, (b) 14Å tobermorite, and (c) jennite.

4.3.2 *Molecular Mechanisms of Cs^+ Ion Binding to the Crystalline C-S-H Basal Surfaces*

Different adsorption capacities of the three crystalline C-S-H structures were observed for Cs^+ (Figure 4.4, Table 4.4). The Cs^+ ion binding capacity increased in the sequence jennite $< 14\mathring{A}$ tobermorite $< 9\mathring{A}$ tobermorite. For the $9\mathring{A}$ tobermorite structure, *ca*. 54% of the total Cs^+ ions (with standard deviation of 4.5%) were adsorbed at the tetrahedral SiO_4 surface and *ca*. 10.4% of the Cs^+ ions were surface bound at the octahedral CaO_6 surface. This percentage decreased to *ca*. 48% for Cs^+ ions (with standard deviation of 5.4%) at the tetrahedral SiO_4 surface and *ca*. 4.6% at the octahedral CaO_6 surface for the $14\mathring{A}$ tobermorite structure. The lowest adsorption capacity was observed for the jennite structure with only *ca*. 3.3% of the total Cs^+ ions (with standard deviation of 2.2%) surface bound at the tetrahedral SiO_4 surface and *ca*. 5.0% at the octahedral CaO_6 surface.

For all three crystalline C-S-H structures, Cs^+ ions were found preferentially located at the tetrahedral SiO_4 surfaces while small amounts of Cs^+ ions were adsorbed to the octahedral CaO_6 surfaces; Cl^- ions were located at the octahedral CaO_6 surfaces (Figure 4.4). For the jennite structure, small amounts of Cl^- ions (1.6%) were also found at the tetrahedral SiO_4 surface due to counter-ion driven adsorption.
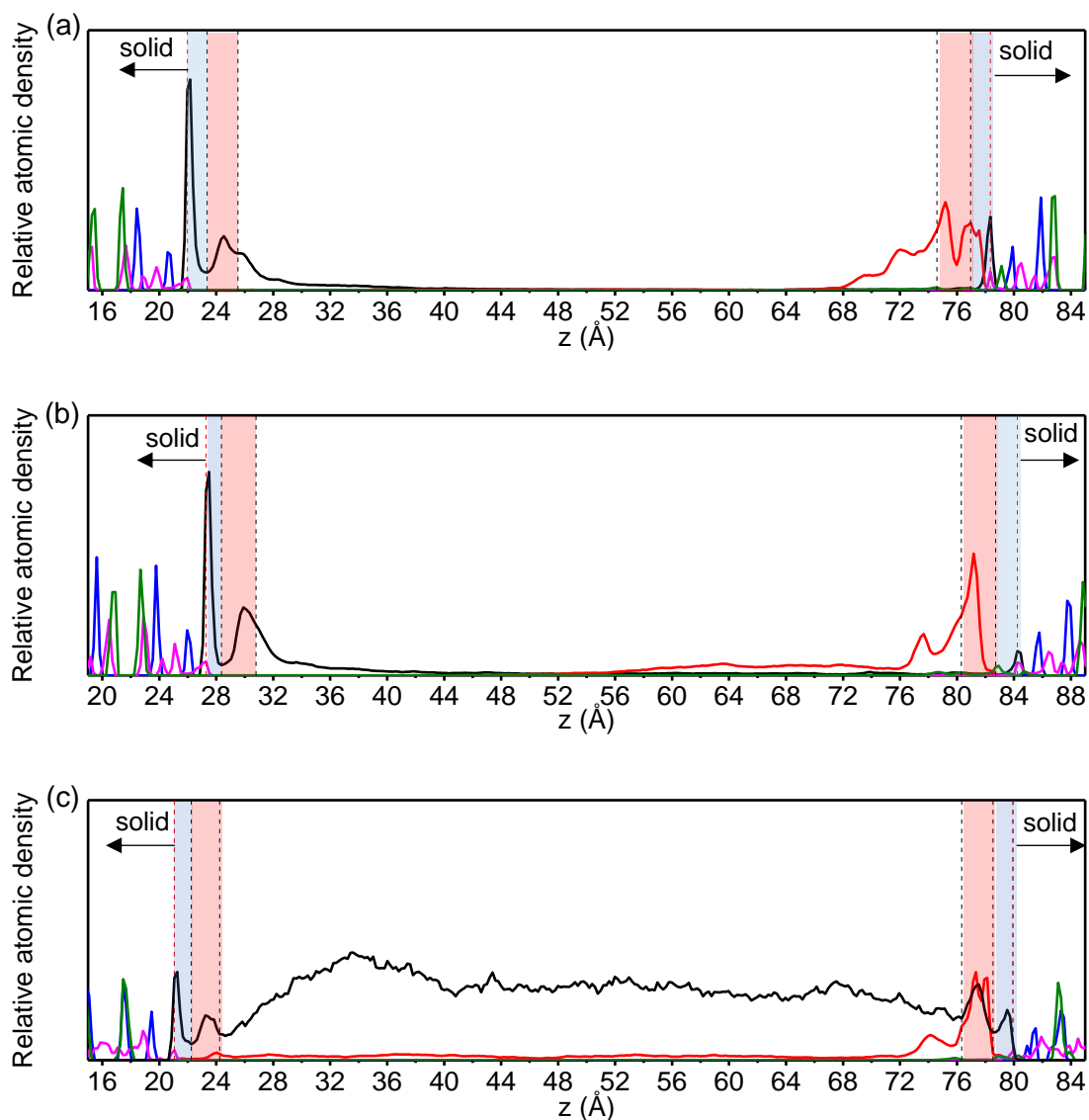
Figure 4.4. Relative atomic density profiles for three different C-S-H crystalline phase-0.5M systems: (a) 9Å tobermorite, (b) 14Å tobermorite, and (c) jennite. Color key: black (Cs), red (Cl), magenta (O), blue (Si), green (Ca). The inner-sphere region is highlighted in blue while the outer-sphere region is highlighted in red. Red dash line corresponds to the surface.

Table 4.4. Adsorption statistics for inner-sphere region and the total surface for different crystalline C-S-H structure/0.5M CsCl aqueous solution interfaces.

The tetrahedral SiO$_4$ surfaces

	Inner-sphere Cs complexes					Total adsorbed Cs			
	Ntot	Nad	ρ (1/nm^2)	Xad (%)	Std (%)	Nad	ρ (1/nm^2)	Xad (%)	Std (%)
9Å tobermorite	12	4.11	0.63	34.3	7.2	6.46	1.00	53.8	4.5
14Å tobermorite	9	2.65	0.54	29.5	6.5	4.36	0.88	48.4	5.4
jennite	11	0.17	0.03	1.6		0.37	0.06	3.3	2.2

The octahedral CaO$_6$ surfaces

	Inner-sphere Cs complexes				Total adsorbed Cs		
	Ntot	Nad	ρ (1/nm^2)	Xad (%)	Nad	ρ(1/nm^2)	Xad
9Å tobermorite	12	1.17	0.18	9.7	1.25	0.19	10.4
14Å tobermorite	9	0.34	0.07	3.8	0.42	0.08	4.6
jennite	11	0.15	0.02	1.3	0.55	0.08	5.0

Ntot: total number of Cs$^+$ ions in the system.
Nad: total number of Cs$^+$ ions adsorbed in the inner-sphere region.
Xad: percentage of the Cs$^+$ adsorbed.
ρ: adsorption density.
Std: standard deviation.

4.3.2.1 Tetrahedral SiO$_4$ Surface

Well-defined inner-sphere and outer-sphere complexes were present for Cs$^+$ ions at the tetrahedral SiO$_4$ surface of all the three crystalline C-S-H phases. For the tobermorites, Cs$^+$ ions were mainly adsorbed as inner-sphere complexes, as indicated by a pronounced peak of Cs$^+$ ions in the inner-sphere region (*i.e.*, 1-2Å from surface) (Figure 4.4). However, for jennite, although Cs$^+$ ions showed similar adsorption patterns as those at the tetrahedral SiO$_4$ surfaces of tobermorites, the relative atomic density of inner-sphere complexes and outer-sphere complexes was lower than that in the bulk solution, which indicated that the adsorption of Cs$^+$ ions was not favorable at the tetrahedral SiO$_4$ surface of jennite. Moreover, co-ion adsorption might also increase the amount of Cs$^+$ ions adsorbed at the tetrahedral SiO$_4$ surface of jennite.

A relatively larger fraction of the surface associated with Cs^+ occurred in the inner-sphere region with *ca.* 34% of all Cs^+ ions for 9Å tobermorite, *ca.* 29% for 14Å tobermorite and *ca.* 1.6% for the jennite structure, compared to the surface associated with Cs^+ in both inner-sphere and outer-sphere regions with *ca.* 54% and 48% and 3.3% of all Cs^+ ions for the 9Å tobermorite and 14Å tobermorite and jennite structures, respectively (Table 4.4, Figure 4.5a). This result was consistent with experimental results from solid-state NMR spectroscopy previously reported in the literature that indicated inner-sphere adsorption as the main mechanism for Cs^+ ions in hydrated C-S-H [17]. The difference in adsorption capacity between the three different crystalline C-S-H structures was motivated by structural differences of the basal tetrahedral SiO_4 surface. The surface Ca layer of the jennite structure was located closer to the surface (~3.6Å) than that of the tobermorite structures (~4.5Å), making the adsorption of Cs^+ in the inner-sphere region of jennite less favorable because of the more prominent repulsive interactions between Cs^+ and Ca ions (Figure 4.6). The secondary peak observed in the outer sphere region of both tobermorite structures indicated adsorption of Cs^+ also as outer-sphere complexes. The secondary peak in the outer-sphere region, however, showed a similar area with the peak in the inner-sphere region for the jennite structure (*ca.* 1.7% vs *ca.* 1.6%), which indicated that at the tetrahedral SiO_4 surface of jennite, outer-sphere adsorption was as important as inner-sphere adsorption, most likely due to the co-ion driven adsorption in the outer-sphere region.

4.3.2.2 Octahedral CaO_6 Surface

At the octahedral CaO_6 surfaces of all the three crystalline C-S-H phases, non-negligible adsorption behavior of Cs^+ ions was observed. At the octahedral CaO_6 surfaces of tobermorites, a pronounced Cs peak was observed in the inner-sphere region, while outer-sphere complexes were negligible. However, at the octahedral CaO_6 surfaces of jennite, the peak of outer-sphere Cs complex was higher than that of inner-sphere Cs complex. Given the fact that the amount of Cl^- ions adsorbed at the octahedral CaO_6 surfaces was much larger than that of Cs^+ ions at the same surface and the adsorption of Cl^- ions occurred earlier than Cs^+ ion at the (0 0 -1) surfaces, the adsorption of Cs^+ ions at the octahedral CaO_6 surfaces might be attributed to the adsorption of Cl^- ions (*i.e.* co-ion adsorption).

A significantly larger fraction of surface associated Cs^+ occurred in the inner-sphere region with *ca.* 9.7% of all the Cs^+ for 9Å tobermorite and *ca.* 3.8% for 14Å tobermorite compared to

10.4% and 4.6% of all surface bound Cs^+ ions (inner-sphere and outer-sphere complexes). On the other hand, a relatively smaller fraction of surface associated Cs^+ occurred in the inner-sphere region with a *ca.* 1.3% for jennite compared to 5.0% of all surface bound Cs^+ ions (inner-sphere and outer-sphere complexes) (Table 4.4, Figure 4.5b). The difference in the adsorption mechanisms of Cs^+ ions between the two tobermorite structures might be attributed to the location of the surface Ca ions. The positions of Ca ions on the surface of 14Å tobermorite were above the surface, while the positions of Ca ions on the surface of 9Å tobermomorite were below the surface (Figure 4.7). Ca ions above the surface of the 14Å tobermorite structure occupied part of the adsorption sites and made the formation of Cs complexes difficult.
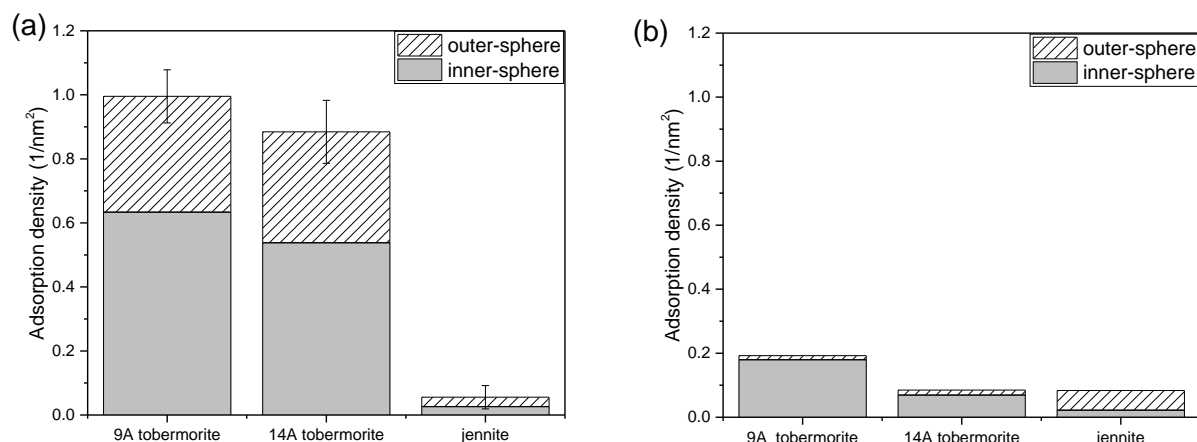
Figure 4.5. Adsorption density of Cs^+ on (a) the tetrahedral SiO_4 surface and (b) the octahedral CaO_6 surface of all the three crystalline C-S-H phases.
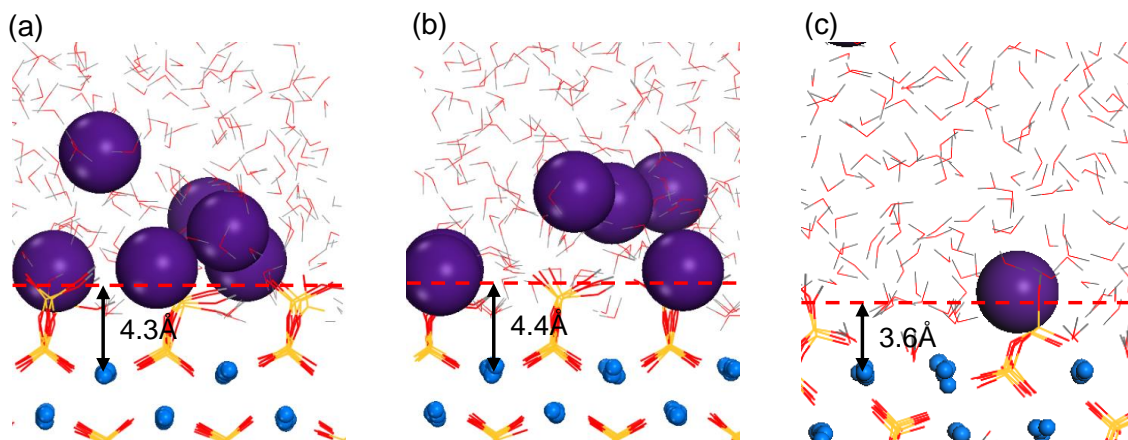
Figure 4.6. Snapshot of the local structure at 12 ns at the tetrahedral SiO$_4$ surface of (a) 9Å tobermorite, (b) 14Å tobermorite and (c) jennite showing the different location of the Ca layer with respect to the solid surface. Color key: green (Cl), blue (Ca), yellow (Si), red (O), grey (H), purple (Cs). Red dash line corresponds to the surface.
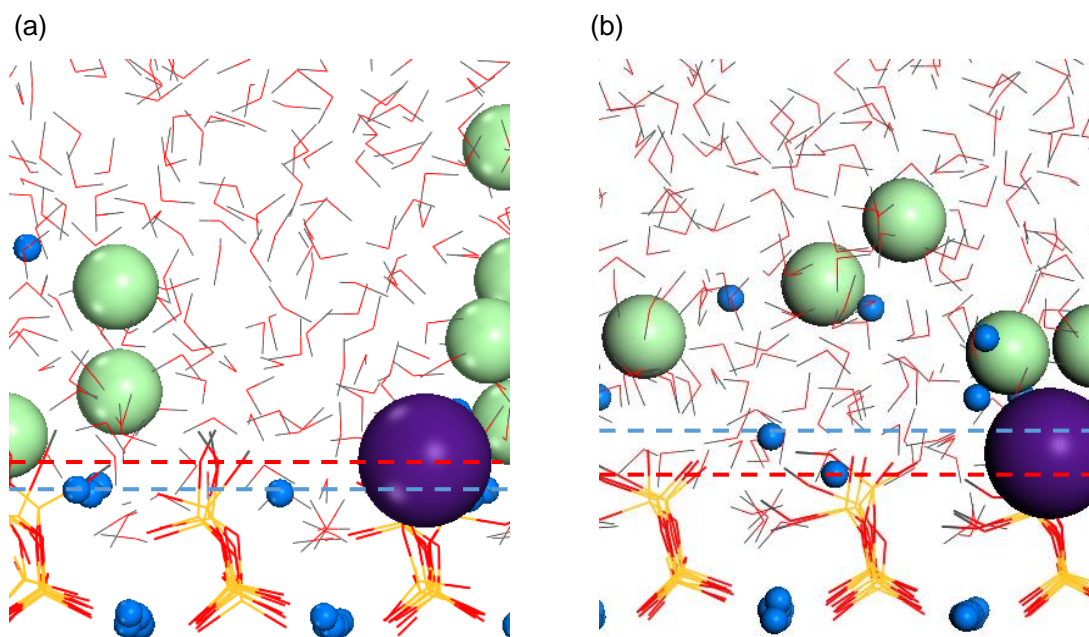
Figure 4.7. Snapshot of the local structure at 12 ns at the octahedral CaO6 surface of the (a) 9Å tobermorite and (b) 14Å tobermorite. Color key: green (Cl), blue (Ca), yellow (Si), red (O), grey (H). Red dash lines correspond to the surfaces. Blue dash lines correspond to the original positions of Ca ions.

4.3.3 Structure of the Crystalline C-S-H/Solution Interfaces

4.3.3.1 Interface Water

The adsorption of water was affected by the crystalline C-S-H structure type as seen from the relative atomic density profiles of oxygen atoms of water molecules (Figure 4.8). For all crystalline structures, the water molecules penetrated ~2-3Å into the silicate channels of both tetrahedral SiO_4 and octahedral CaO_6 surfaces. The strong oscillation of the water density (oxygen atom in water molecules) near the tobermorite structures indicated a stronger layering of the water molecules at the tobermorite surfaces compared to jennite. In contrast to tobermorites, the jennite structure possesses interlayer Ca-OH groups making the diffusion of the water molecules in the vicinity of the surface more difficult. The layering of water near solid-water interfaces has been previously observed in atomistic simulations at other mineral surfaces such as clay [175] and silica [176]. The water molecules in the vicinity of the tetrahedral SiO_4 surface (*i.e.* up to 3-4Å) of the 14Å tobermorite and 9Å tobermorite structures showed a preferential orientation (Figure 4.9) with the dipole vector pointing towards the silicate chain (*i.e.* dipolar angle distribution characterized by angles from 120° to 150° as shown in Figure 4.10), indicating that the tetrahedral SiO_4 surface remained negatively charged and thus that all surface sites were not occupied by the Cs^+ ions (*i.e.* the tobermorite tetrahedral SiO_4 surface was not saturated and more Cs^+ ions could be adsorbed). In contrast, the jennite structure had no influence on the orientation of the water dipoles (Figure 4.9), which appeared oriented randomly as in the bulk. At the surface of jennite for a concentration of CsCl 0.5M, all the adsorption sites were occupied by Cs^+ ions (Figure 4.6b) and a neutrally charged cavity was formed at the position of the Ca-OH groups.
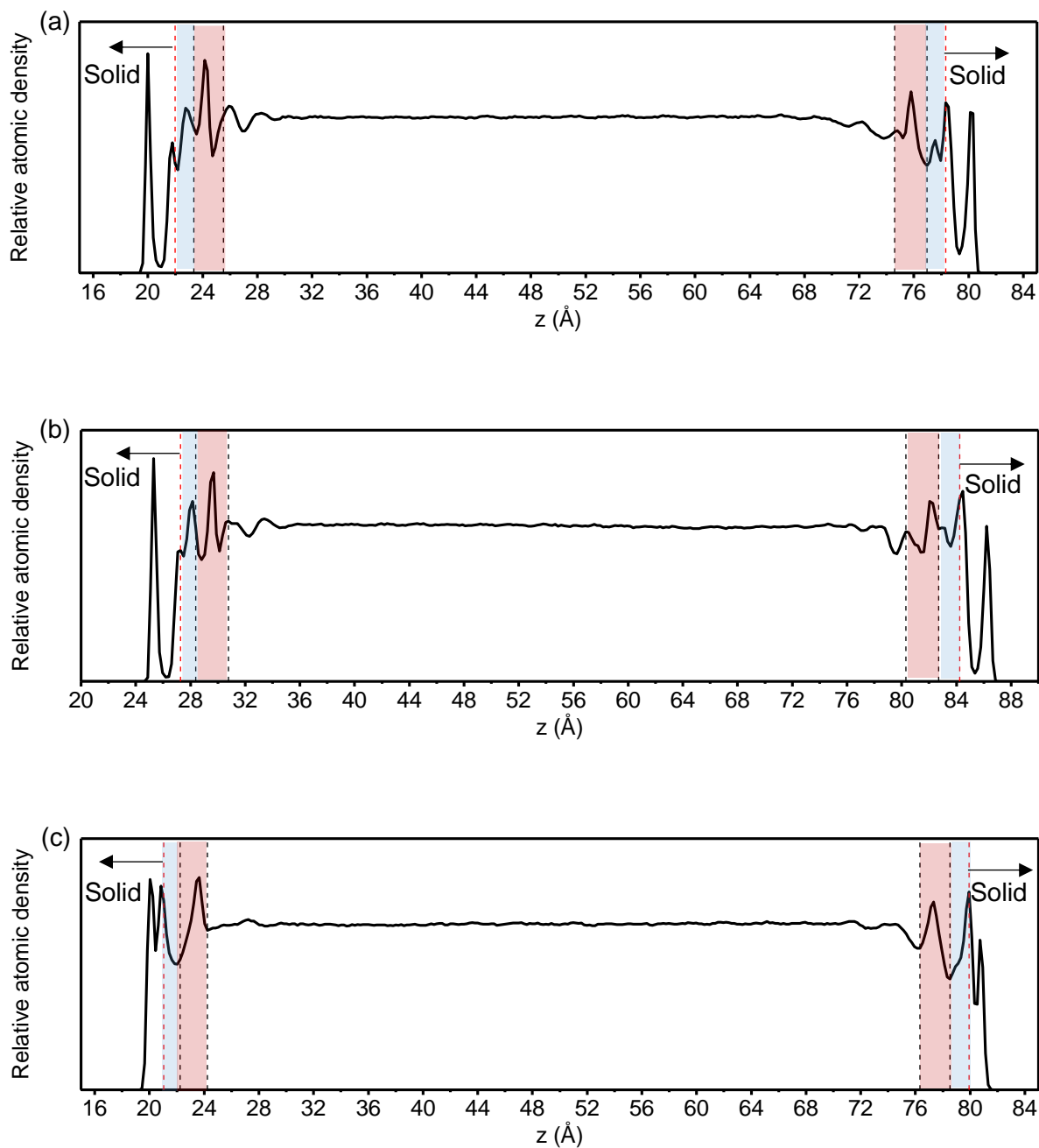
Figure 4.8. Relative atomic density profiles of O in H_2O molecules for three different crystalline C-S-H phases: (a) 9Å tobermorite, (b) 14Å tobermorite, and (c) jennite. The inner-sphere region is highlighted in blue while the outer-sphere region is highlighted in red. Red dash line corresponds to the surface.
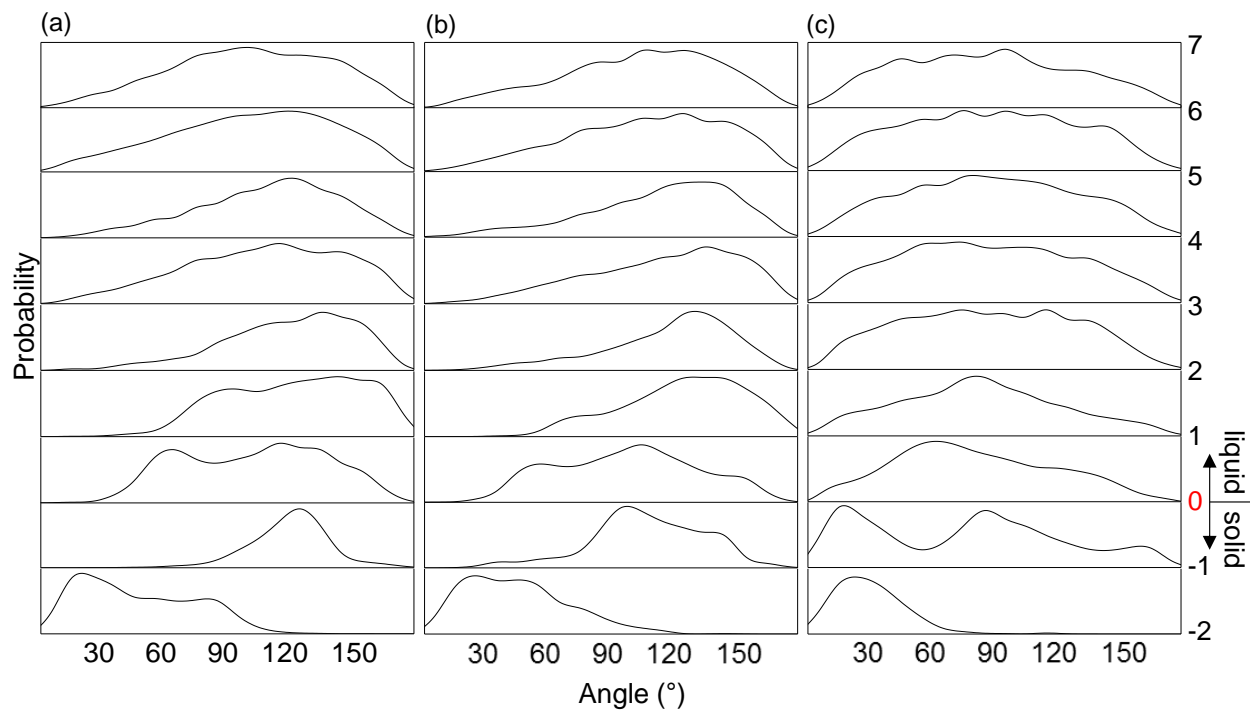
Figure 4.9. Distribution of the angle between the water dipole and the normal vector for the surface of the tetrahedral SiO_4 surface as a function of distance from the surface: (a) 9Å tobermorite, (b) 14Å tobermorite, and (c) jennite for a CsCl concentration of 0.5M. Surface is indicated by 0.
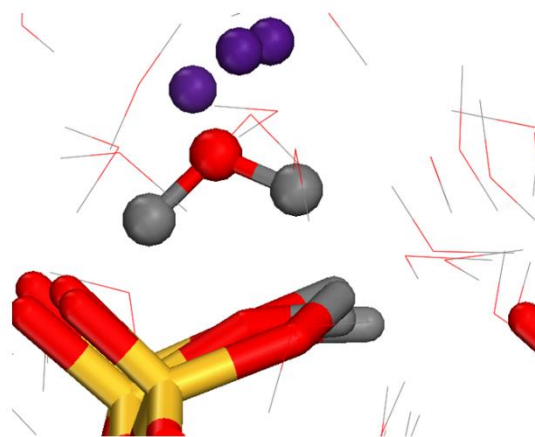
Figure 4.10. Snapshot at 12 ns of a water molecule with the OH groups pointing towards the silicate chain at the tetrahedral SiO_4 surface of 14Å tobermorite. Color key: yellow (Si), red (O), grey (H), purple (Cs).

4.3.3.2 Adsorption Site Structural Information

The atomic density contour maps at the tetrahedral SiO_4 surface of the three crystalline C-S-H structures showed a strong spatial correlation in the inner-sphere region (Figure 4.11) between Cs^+ ions and the surface silicon (Si) and bridging oxygen atoms (Ob). The contour maps indicated that the 14Å tobermorite structure presented more structural changes than the 9Å tobermorite and jennite structures. Inner-sphere Cs^+ ions were located preferentially at the cavities of the silicate chains in all three crystalline C-S-H structures and had little mobility in the plane parallel to the surface. Outer-sphere Cs^+ complexes, on the other hand, showed higher mobility and less stability for the three crystalline C-S-H structures (Figure 4.12).

Contour maps of the octahedral CaO_6 surface of the tobermorite structures for inner-sphere Cs complexes (Figure 4.13) showed that the surface Ca ions became disordered. The surface Ca ions were more disordered at the octahedral CaO_6 surface of 14Å tobermorite than 9Å tobermorite. The adsorption of inner-sphere Cs complexes most likely happened at the locations where surface Ca ions have diffused out of the surfaces; Cs^+ ions could go through these locations and be adsorbed at the octahedral CaO_6 surfaces.
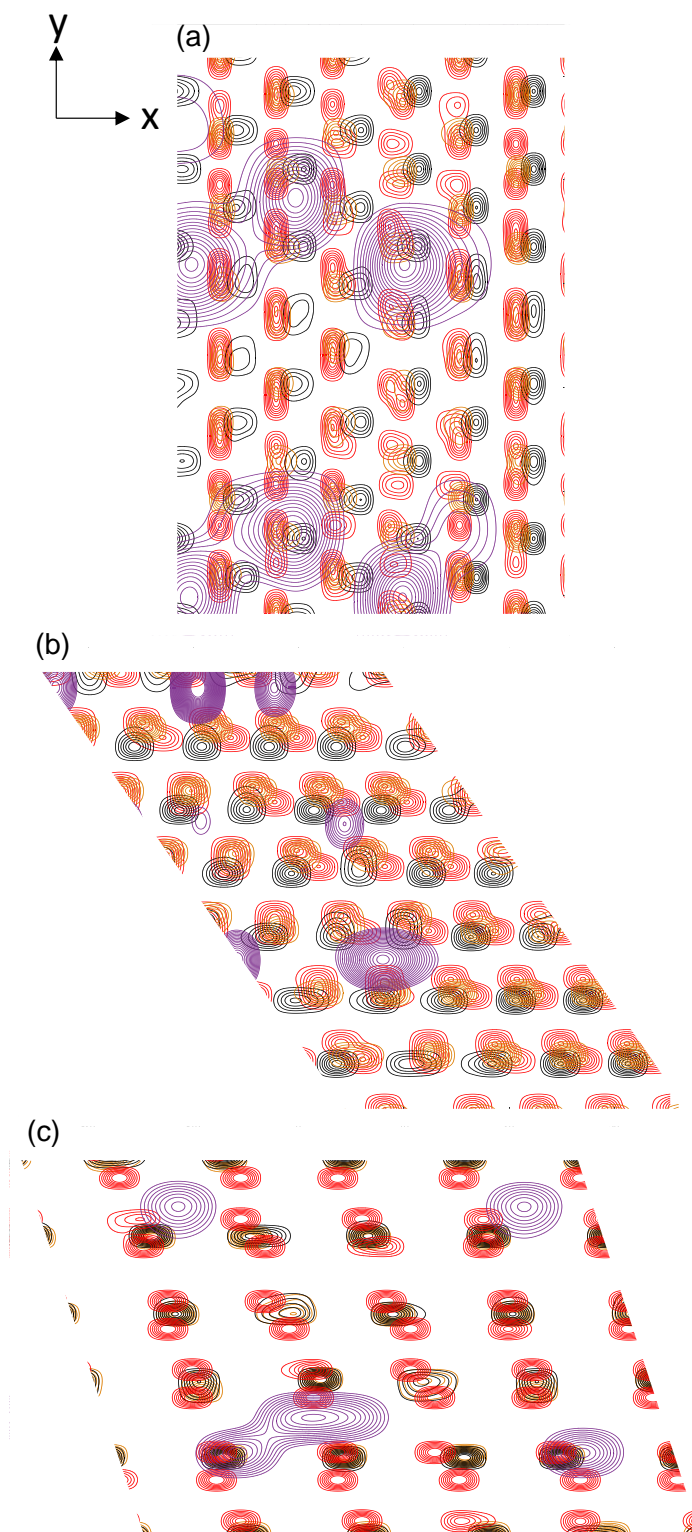
Figure 4.11. Atomic density contour maps of the inner-sphere region of the tetrahedral SiO$_4$ surface of (a) 9Å tobermorite, (b) 14Å tobermorite, and (c) jennite in contact with 0.5M CsCl solution. [Legend: red contours: surface bridging O atoms; black contours: O atoms of SiOH groups; brown contours: Si of SiOH groups; violet contours: Cs$^+$ cations]
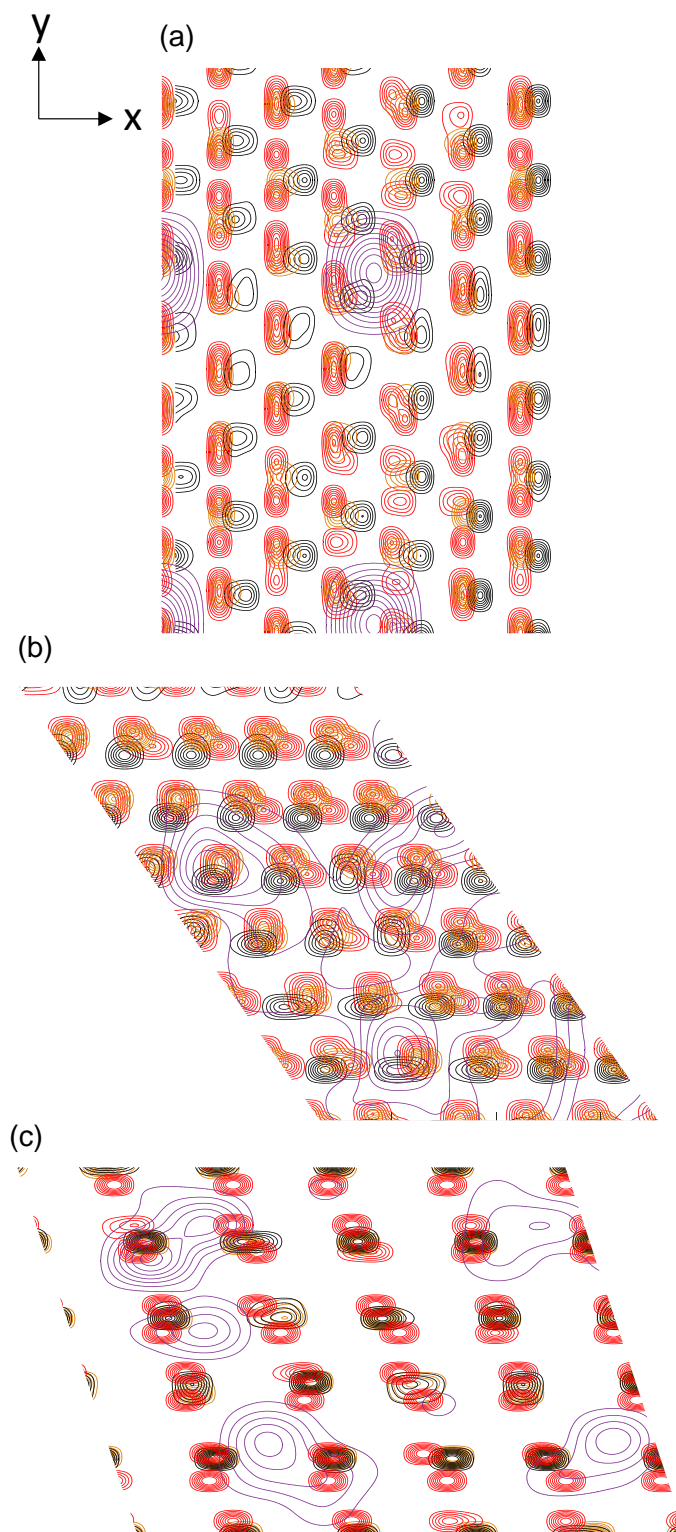
Figure 4.12. Atomic density contour maps of the outer-sphere region of the tetrahedral SiO_4 surface of (a) 9Å tobermorite, (b) 14Å tobermorite, and (c) jennite in contact with 0.5M CsCl solution. [Legend: red contours: surface bridging O atoms; black contours: O atoms of SiOH groups; brown contours: Si of SiOH groups; violet contours: Cs^+ cations].
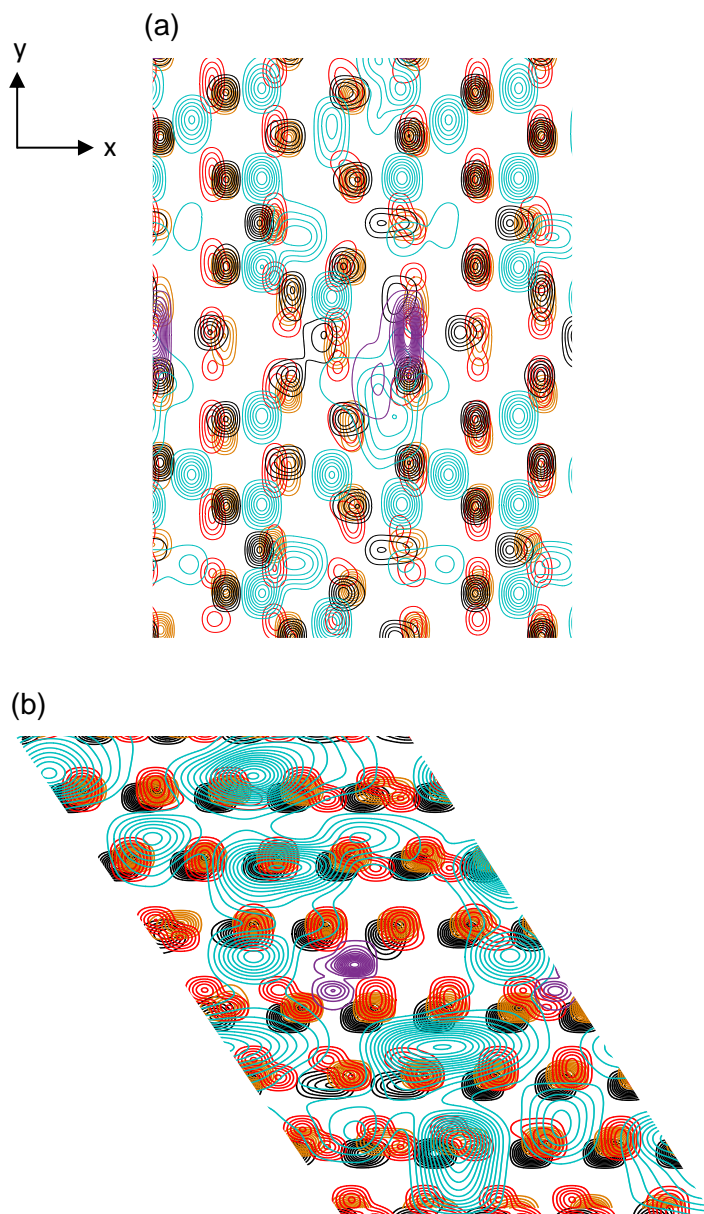
Figure 4.13. Atomic density contour maps of the inner-sphere region of the octahedral CaO_6 surface of (a) 9Å tobermorite and (b) 14Å tobermorite in contact with 0.5M CsCl solution. [Legend: red contours: surface bridging O atoms; black contours: O atoms of SiOH groups; brown contours: Si of SiOH groups; teal contours: Ca cations; violet contours: Cs^+ cations].

The RDFs were calculated for inner-sphere Cs complexes at both surfaces of the tobermorites, mainly between Cs^+ ions and structural O atoms (*i.e.* O atoms in the crystalline C-S-H structures: bridging O, hydroxyl O, and bridging O with tetrahedral substitution). At the

tetrahedral SiO_4 surface of the tobermorites, Cs-Ob RDFs (RDF between the bridging O and Cs^+ ions) presented a pronounced peak at ~3Å (Figure 4.14a and b), and ~3 Ob (bridging oxygen) atoms coordinated with one (1) Cs^+ ion for the tobermorite structures (Table 4.5). Although one (1) Cs^+ ion coordinated with the same number of Oh atoms in the first coordination shell (~3), the characteristic distance (R) of the Cs-Oh pair was larger than that of the Cs-Ob pair (Table 4.5). These results indicated that Cs^+ ions adsorbed in the inner-sphere region of the tetrahedral SiO_4 surfaces of the tobermorites mainly coordinated with Ob atoms. The interaction between inner-sphere Cs^+ ions and bridging O with tetrahedral substitution (Cs-Obts) was weak; RDFs presented peaks at longer distances (~ 5Å) for both 9Å and 14Å tobermorite (Figure 4.14).

Although RDFs for Cs^+ ions at the octahedral CaO_6 surface of 14Å tobermorite showed a similar pattern with those at the tetrahedral SiO_4 surface (Figure 4.14b and d), Cs^+ ions coordinated with less Ob and Oh in the first coordination shell at the octahedral CaO_6 surface (Table 4.5). This result was thought to be due to the interaction between Cs^+ ions and Cl^- ions that adsorbed at the same surface. Adsorbed Cl^- ions were located further away from the surface compared to the Cs^+ ions. The attractive interaction between Cl^- ions and Cs^+ ions could contribute to the desorption of Cs^+ ions at the surface. As a result, Cs^+ ions coordinated with less O atoms.

Though Cs-Ob RDF at the octahedral CaO_6 surface of 9Å tobermorite showed a similar pattern to that at the tetrahedral SiO_4 surface, the Cs-Oh and Cs-Obts RDFs had different patterns than those at the tetrahedral SiO_4 surface (Figure 4.14a and c). Cs-Oh RDF had smaller R, which indicated that in the inner-sphere complexes, Cs^+ ions were located closer to Oh compared to the inner-sphere complexes at the tetrahedral SiO_4 surface (Table 4.5). The first Cs-Oh RDF major peak merged several peaks, which indicated the unstable coordination between Cs^+ ions and Oh atoms. The Cs-Obts RDF only showed one major peak within the distance of 6Å at the octahedral CaO_6 surface (Figure 4.14c), compared to two peaks at the tetrahedral SiO_4 surface (Figure 4.14a). Cs^+ ions adsorbed at the octahedral CaO_6 surface of 9Å tobermorite coordinated with less Ob and Oh atoms in the first coordination shell compared to the inner-sphere complexes at the tetrahedral SiO_4 surface due to attractive interaction between Cl^- ions and Cs^+ ions (Table 4.5). The different patterns for Cs-Oh and Cs-Obts RDFs at surfaces of 9Å tobermorite might be due to the difference between the surface structures.

The difference of the structure of inner-sphere Cs complexes between the tetrahedral SiO_4 surface and the octahedral CaO_6 surface of tobermorites was mainly due to the presence of Ca layers. Ca ions at the octahedral CaO_6 surfaces tended to leak out of the surfaces of tobermorites; Cs^+ ions that could penetrate through the surface Ca layer interacted with the structure beneath the Ca layer, which was very similar to corresponding tetrahedral SiO_4 surface. This result explained the similarity between the RDF patterns at the tetrahedral SiO_4 surface and the octahedral CaO_6 surface.
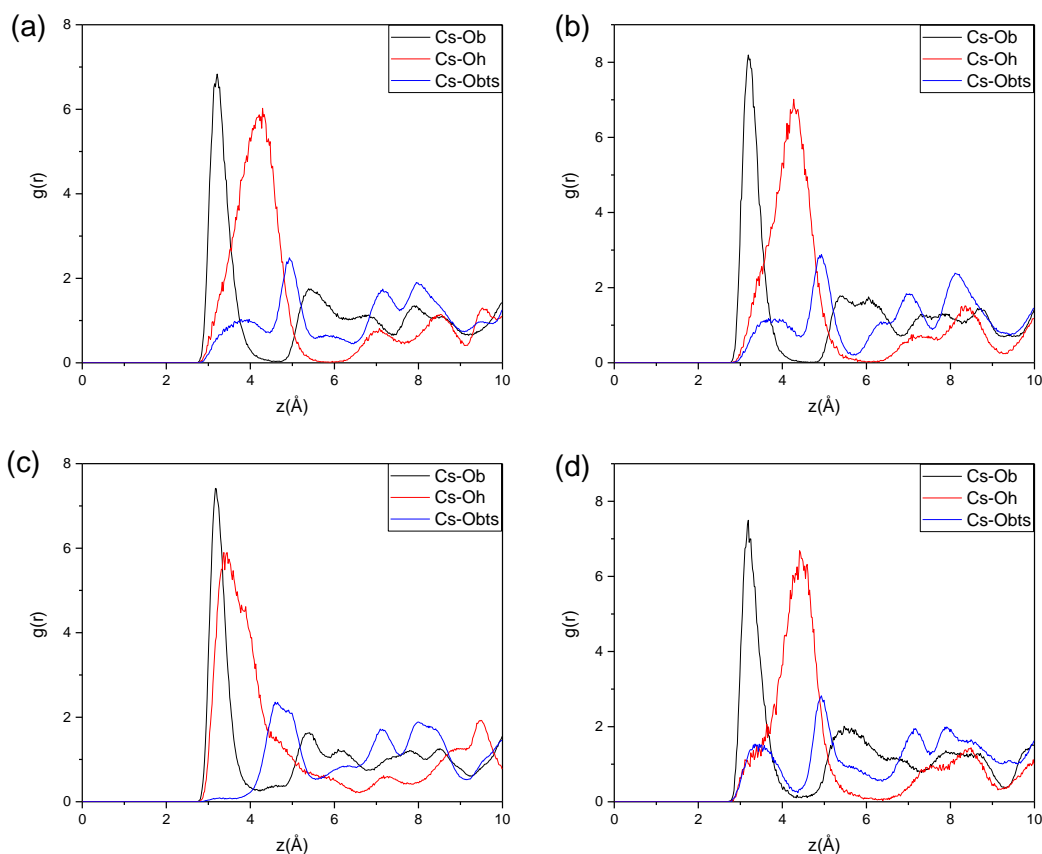
Figure 4.14. RDFs between inner-sphere Cs^+ ions and different types of structural O at the tetrahedral SiO_4 surface of: (a) 9Å tobermorite and (b) 14Å tobermorite; and the octahedral CaO_6 surface of: (c) 9Å tobermorite and (d) 14Å tobermorite. Ob is bridging O, Oh is hydroxyl O, and Obts is bridging O with tetrahedral substitution.

Table 4.5. Coordination number (N) and characteristic distance (R) of inner-sphere Cs complexes

	N		R(Å)	
	9Å tobermorite	14Å tobermorite	9Å tobermorite	14Å tobermorite
tetrahedral SiO₄ surface				
Cs-Ob	3.0	2.9	3.21	3.19
Cs-Oh	3.1	3.1	4.33	4.29
octahedral CaO₆ surface				
Cs-Ob	2.0	2.0	3.27	3.19
Cs-Oh	2.0	2.0	3.67	4.41

4.3.4 Adsorption Energies and Hydration Energies

The inner-sphere adsorption energies were calculated for inner-sphere complexes at the tetrahedral SiO_4 surfaces of all three crystalline C-S-H phases (Figure 4.15). The inner-sphere adsorption energy between Cs^+ ions and 9Å tobermorite was -534.5 kcal/mol ± 8.5 kcal/mol (± indicated one sample standard deviation about the mean). The inner-sphere adsorption energy between Cs^+ ions and 14Å tobermorite was -580.2 ± 8.2 kcal/mol. The inner-sphere adsorption energy between Cs^+ ions and jennite was only -7.1 ± 14.0 kcal/mol, which indicated that the adsorption reaction was not thermodynamically favored. The hydration energy of Cs^+ ion was -41.1 kcal/mol. The much lower inner-sphere adsorption energy of Cs^+ ions on the surface of tobermorites compared to the hydration energy indicated that inner-sphere adsorption was energetically favorable. The lower hydration energy of Cs^+ ion compared to the inner-sphere adsorption hydration energy of Cs^+ ions on the surface of jennite indicated that the adsorption of Cs^+ ions on the surface of jennite was not energetically favorable.

The interaction energy between inner-sphere Cs complexes and the octahedral CaO_6 surface was calculated for tobermorites and compared with the interaction energy between inner-sphere Cs complexes adsorbed at the octahedral CaO_6 surface and Cl^- ions (Table 4.6). The adsorption of Cs^+ ions at the octahedral CaO_6 surface was triggered by co-ion adsorption: Cl^- ions adsorbed at the octahedral CaO_6 surfaces and made the surface negatively charged, which attracted

Cs$^+$ ions remaining in the bulk solution to adsorb at the octahedral CaO$_6$ surfaces. The results indicated that the interaction between inner-sphere Cs complexes and the octahedral CaO$_6$ surfaces was not energetically favorable. The occurrence of inner-sphere Cs adsorption was triggered by co-ion adsorption: Cl$^-$ ion adsorbed at the octahedral CaO$_6$ surfaces attracted Cs$^+$ ions from the bulk solution to the octahedral CaO$_6$ surface. Those Cs$^+$ ions were able to penetrate through the disordered surface Ca layers and interact with Ob and Oh atoms. The disordered Ca layers prevented the desorption behavior of inner-sphere Cs complexes and enhanced stable inner-sphere Cs complexes at the octahedral CaO$_6$ surfaces.
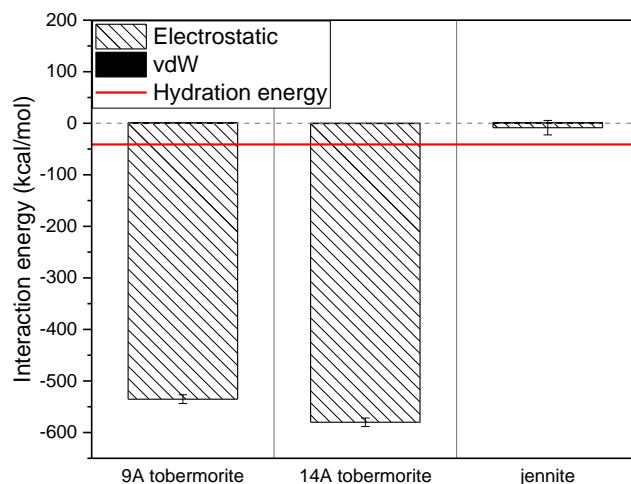
Figure 4.15. Inner-sphere interaction energy and hydration energy of Cs ions for all the three crystalline C-S-H phases at the tetrahedral SiO$_4$ surfaces. Note: vdW indicates van der Waals energies.

Table 4.6. Interaction energies between inner-sphere Cs complexes and the octahedral CaO$_6$ surface surfaces and between inner-sphere Cs complexes and Cl$^-$ ions.

	Interaction energy (kcal/mol)	
	octahedral CaO$_6$ surface + inner-sphere Cs	Cl$^+$ ions + inner-sphere Cs
9Å tobermorite	374.60 ± 29.47	-465.37 ± 21.63
14Å tobermorite	231.36 ± 35.00	-361.13 ± 38.60

4.3.5   Dynamic Properties at the Crystalline C-S-H Basal Surfaces

In the inner-sphere regions of 9Å tobermorite and 14Å tobermorite, Cs^+ ions diffused three to four orders of magnitude slower than in the bulk solution (0.00024×10^{-5} vs. $2.59 \times 10^{-5} cm^2/s$ for 9Å tobermorite and 0.00016×10^{-5} vs. $3.47 \times 10^{-5} cm^2/s$ for 14Å tobermorite) (Figure 4.16, Table 4.7), which indicated that the Cs complexes were stable in the inner-sphere region and unlikely to diffuse out from the surface. In contrast, the diffusion coefficients of Cs^+ ions in the outer-sphere region were one order of magnitude lower than in the bulk solution for the 9Å tobermorite and 14Å tobermorite structures (0.31×10^{-5} vs. 2.59×10^{-5} cm^2/s for 9Å tobermorite and 0.27×10^{-5} vs. 3.47×10^{-5} cm^2/s for 14Å tobermorite) (Figure 4.16, Table 4.7).

Inner-sphere Cs complexes diffused faster at the octahedral CaO_6 surfaces compared to those adsorbed at the tetrahedral SiO_4 surfaces (0.00045×10^{-5} vs. 0.00024×10^{-5} cm^2/s for 9Å tobermorite and 0.0005×10^{-5} vs. 0.00016×10^{-5} cm^2/s for 14Å tobermorite) due to the attractive interaction between Cl^- ions and Cs^+ ions at the octahedral CaO_6 surfaces (Figure 4.16, Table 4.7).

The calculated average diffusion coefficients for aqueous Cs^+ ions in the bulk solution (2.59 ± 1.19 - $3.47 \pm 0.64 \times 10^{-5}$ cm^2/s) were on the same magnitude with values found in the literature (1.19-$2.36 \times 10^{-5} cm^2/s$) [177,178]. Experimental conditions could be very different from those in simulations; the data were close enough to confirm the reliability of simulation results.
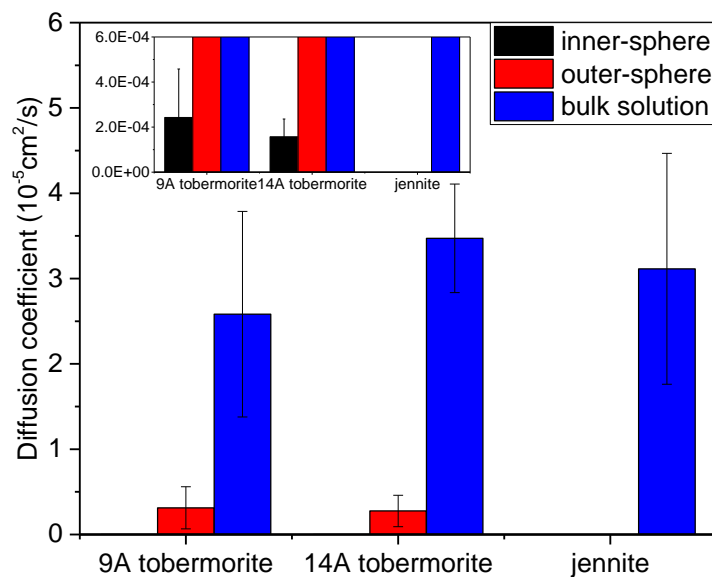
Figure 4.16. Diffusion coefficients of inner-sphere, outer-sphere Cs complexes and Cs species in the bulk solution at the tetrahedral SiO_4 surfaces.

Table 4.7. Diffusion coefficient of Cs^+ ions ($10^{-5}cm^2/s$).

	9Å tobermorite	14Å tobermorite	jennite	Experimental
Aqueous				
Cs^+	2.59±1.19	3.47±0.64	3.11±1.35	1.19-2.36 [a,b]
Cs^+ adsorbed at tetrahedral SiO_4 surface				
Inner-sphere	0.00024±0.00020	0.00016±0.000079	N/A	
Outer-sphere	0.31±0.25	0.27±0.18	N/A	
Cs^+ adsorbed at octahedral CaO_6 surface				
Inner-sphere	0.00045*	0.0005*	N/A	
Outer-sphere	N/A	N/A	N/A	

N/A = not applicable.

* Insufficient data to estimate standard deviation.

[a] [177] [b] [178]

4.4   Conclusions

The energetic, structural, and dynamic behavior of water and ions at crystalline C-S-H surface-liquid phase interfaces have been studied on an atomic scale. Results obtained in the present work contribute toward a further understanding of the stability of cementitious waste forms and future design of new waste forms with better performance. The main findings are summarized as follows:

- Cs^+ ions were mainly adsorbed as inner-sphere complexes on the SiO_4 surface of 9Å tobermorite and 14Å tobermorite. The adsorption capacity decreased in the sequence of: 9Å tobermorite > 14Å tobermorite > jennite.

- Cs^+ ions mainly interacted with bridging O (Ob) to form inner-sphere complexes in which one Cs^+ ion coordinated with three Ob atoms.

- Inner-sphere adsorption of Cs^+ ions at the SiO_4 surface of 9Å tobermorite and 14Å tobermorite was energetically favorable, while not at the SiO_4 surface of jennite.

- Inner-sphere Cs complexes diffused four orders of magnitude slower than aqueous Cs^+ ions, while outer-sphere Cs complexes were much mobile and diffused one order of magnitude slower than aqueous Cs^+ ions.

- Cl^- ions adsorbed on the octahedral CaO_6 surface of all the three crystalline C-S-H phases; the amount of Cl^- ions adsorbed 5Å above the surfaces decreased in the sequence of: 9Å tobermorite > 14Å tobermorite > jennite. Ca ions played an important role in the adsorption of Cl^- ions.

- Water molecules showed a layered structure at the interface. The dipole moments had a preferred orientation up to 6Å above the SiO_4 surface of 9Å tobermorite and 14Å tobermorite and up to 2Å above the SiO_4 surface of jennite.

CHAPTER 5

5   The adsorption of TcO$_4^-$ Ions on the Surface of Cement Phases

This chapter is planned to be submitted for peer-review publication.

5.1   Overview

The long-lived radionuclide ^{99}Tc is generated during the fission process of ^{235}U. For every ton of enriched uranium fuel (3% ^{235}U) that is consumed at a typical burn-up rate, nearly 1 kg of ^{99}Tc is produced. When released to the environment, plants and animals can take up ^{99}Tc to an appreciable extent; thus the presence of ^{99}Tc in the food chain is an obvious concern [179]. One of the preferred methods for safely disposing radioactive wastes is to immobilize them with concrete.

The mobility and speciation of ^{99}Tc are very sensitive to the redox potential (Eh) and pH of the system, as well as the hydrolytic and complexation equilibria. The solubility of ^{99}Tc is significantly lowered under reducing conditions compared to oxidizing conditions. Low pH and Eh values in cementitious waste forms can be imposed by blending specific additives, *e.g.*, iron blast furnace slag [110]. The addition of blast furnace slag or solidified slag produces cementitious waste forms with few and small pores, which slows ^{99}Tc from leaching [29,32,109]. Moreover, ^{99}Tc mainly presented as a less soluble Tc^{4+} species under the reducing environment (from slag addition) and was effectively immobilized as TcS$_x$ or TcO$_2$•xH$_2$O [29,30]. Portland cement (PC) and fly ash pastes both have high pH and Eh values; the dominant redox species of ^{99}Tc were highly soluble TcO$_4^-$ species under these pH-Eh conditions [110]. PC and fly ash grouts have been shown to be marginally acceptable for retention of TcO$_4^-$ ions. Experimental data indicated that the primary adsorption mechanism was anion exchange and that the exchange with Ca^{2+} ions was weak [32]. PC was studied because it is the most widely used cementitious waste form although blast furnace slag blended cementitious waste forms may be more effective to immobilize ^{99}Tc. For the range of pH values (>12) present in cement leachates, ^{99}Tc exists mainly as highly mobile TcO$_4^-$. Therefore, understanding the interaction mechanisms between PC paste and TcO$_4^-$ is the key to decreasing leaching and designing high performance cementitious waste forms for ^{99}Tc.

Cement paste is a truly complex material; it is porous, multicomponent, and multi-scalar. In PC, hydration products, such as ettringite, coexist with unhydrated clinkers of different sizes surrounded by C-S-H gel. C-S-H gel is one of the most important hydrated products and is mainly responsible for the cohesion of the cement paste. The C-S-H is an amorphous and porous material, although experimental results from different techniques such as ^{29}Si nuclear magnetic resonance (NMR), X-ray diffraction (XRD), and infrared (IR) studies [171–173] revealed that it has a short range ordered structure at atomistic scale. Most knowledge regarding the C-S-H gel has been gained from its comparison with fully crystalline C-S-H such as 14Å tobermorite and jennite. While C-S-H gel is one of the most significant components in hydrated cement paste, ettringite also plays an important role in the chemistry of cement; ettringite can be found at the early hydration stages of Portland cement [180]. The formation of ettringite can cause expansion and cracking and eventually affect the durability of cement paste [82]. 14Å tobermorite, jennite, and ettringite were used as models for cement phases in the present work.

Experimental studies have been conducted to evaluate the adsorption properties for TcO_4^- of various oxides, hydroxides, silicates, sulfides, and activated carbon [179,181–183]. Results indicated that TcO_4^- ions adsorbed weakly onto the solid phases, such as some clay minerals [179,181–183]. Experimental study indicated that bentonite was able to adsorb TcO_4^- ions and decrease the diffusion coefficient of surface species; the adsorption mechanism was through physical adsorption to the sites on the surface, and adsorption was proportional to the specific surface area of bentonite [184]. Although reduction of Tc(VII) has been studied extensively [185–187], relatively little is known about ^{99}Tc adsorption under the hyper-alkaline conditions present in cementitious materials.

A fundamental atomic-level understanding, interpretation, and prediction of immobilizing radionuclides with natural/synthetic phases can be provided by Molecular Dynamic (MD) simulations. Although 14Å tobermorite, jennite, and ettringite have been studied using MD simulations, previous studies mainly focused on structural and mechanical properties of these cement phases [113–122]. The studies concerning dynamic properties either focused on the interactions between cement phases and other ions or molecules, such as Na^+, Sr^{2+} ions, and H_2O molecules [13,35–37,123,124] or used other forcefields other than the ClayFF forcefield that is used in this work [117,118,125,126]. The results indicated that tobermorites and jennite were

capable of adsorbing some ions. Alkali ions such as Na^+ and K^+ ions can be adsorbed both on the surface and penetrate into the silicate channels of 9Å tobermorite and jennite to interact with different structural oxygen, and the interactions in the silicate channels were suggested to be chemical bonding [35].

MD simulations have also been applied to study the interactions between TcO_4^- and other ions in aqueous solution or water molecules; the structural and dynamic properties of hydrated TcO_4^- ions have also been studied [44,133–135]. The adsorption of TcO_4^- ions on a mesoporous amorphous silica known as self-assembled monolayers on mesoporous supports (SAMMS) has also been investigated using MD simulations [136]. MD simulation data on the interactions between TcO_4^- ions and cement phases or other clay minerals have not been published yet.

MD simulations have been used to study the interfacial adsorption mechanisms between crystalline C-S-H phases and other ions and have also been used to study the interaction between TcO_4^- ions and some solid phases. Previous studies separately investigated the two aspects that were combined in this work. This research will provide important information about cementitious waste form capacity and possible solutions for designing new waste forms for problematic constituents. The principal focus here is on immobilizing TcO_4^- ions in three different cement phases: 14Å tobermorite, jennite, and ettringite. The molecular-scale energetic, structural, and dynamic properties of the interface between an aqueous solution containing $KTcO_4$ and cement phases were analyzed by using relative atomic density profiles, radial distribution function (RDF), coordination number (CN), local structure analysis, diffusion coefficient, adsorption energy, and hydration energy.

5.2   Theoretical Methods

5.2.1   Simulation Models and Computational Cells

MD simulations were performed employing three different crystalline structures: 14Å tobermorite, jennite, and ettringite. In the present work, a concentration of 0.2M $KTcO_4$ was chosen to study the interaction mechanisms between TcO_4^- ions and cement phases by analyzing structural, energetic, and dynamical properties (Table 5.1). The concentration of TcO_4^- ions in the tank waste at the Hanford Site was thousands of times lower than the concentration that was used in present work (0.00005M [46] vs. 0.2M). Chemical interactions are not involved in MD simulations; therefore, the interaction mechanisms between radionuclides and cement phases were

not affected by the concentration of radionuclides in the models. The concentration of TcO_4^- ions was chosen due to the limitation of the size of the computational cell that would have required to be significantly bigger to accommodate lower concentration while providing a sufficient number of TcO_4^- ions in the cell to perform proper analysis.

Table 5.1. Details for $KTcO_4$ solution.

	Concentration (M)	Density (g/cm^3)	N of TcO_4^-	N of K^+	N of H_2O
14Å tobermorite	0.2	1	4	4	905
Ettringite	0.2	1	5	5	1142
Jennite	0.2	1	5	5	1200

The 0.2M $KTcO_4$/14Å tobermorite model and 0.2M $KTcO_4$/jennite model were constructed in a similar way. 14Å tobermorite, $Ca_5Si_6O_{16}(OH)_2 \cdot 7H_2O$, was modeled according to the unit cell structure proposed by Bonaccorsi *et al*. [78]. The structure used in the present work was composed of 12 unit cells (3×4×1 units in *a*, *b*, and *c* directions). The jennite structure, $Ca_9Si_6O_{18}(OH)_6 \cdot 8H_2O$, was modeled according to the unit cell structure proposed by Bonaccorsi *et al*. [79]. The jennite structure used in this work was composed of 24 unit cells (3×4×2 units in the *a*, *b*, and *c* directions) (Table 5.2). 14Å tobermorite and jennite were created by cleaving the crystal structure parallel to the tetrahedral SiO_4 and the octahedral CaO_6 surfaces under the interlayer Ca ions. On both surfaces, bridging silicate tetrahedrons were exposed to the solution. Interlayer water molecules of 14Å tobermorite and interlayer water molecules and hydroxyl groups of jennite were evenly distributed on both surfaces, while interlayer Ca ions were left on the octahedral CaO_6 surface.

Ettringite, $Ca_6[Al(OH)_6]_2(SO_4)_3 \cdot \sim 26H_2O$, was modeled according to unit cell structure described by Moore and Taylor [84]. The ettringite structure used in this work was composed of 6 unit cells (2×3×1 units in the *a*, *b*, and *c* directions) (Table 5.2) and were created by cleaving the crystal structure perpendicular to the Al_2O_3 columns under intracolumn Ca ions. Column Ca ions and the water molecules coordinated with Ca ions were left on one surface, which was named the

octahedral CaO$_6$ surface. The other surface was named the tetrahedral SO$_4$ surface, which was characterized by tetrahedral SO$_4$ groups pointing out (Figure 5.1).

octahedral CaO$_6$ surface

tetrahedral SO$_4$ surface
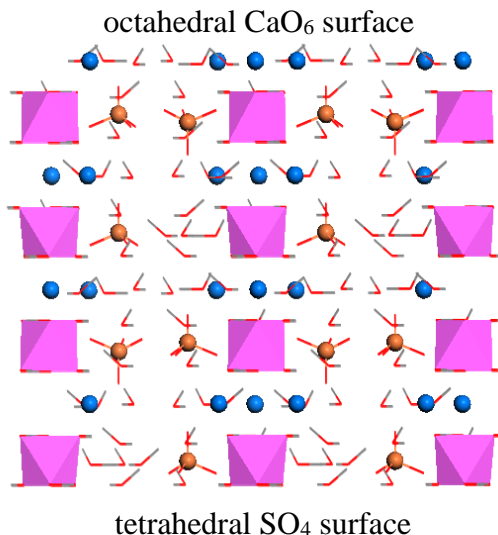
Figure 5.1. The characterization of the tetrahedral SO$_4$ surface and the octahedral CaO$_6$ surface of ettringite.

Two layers of geometry optimized cement phases were used to build the simulation box, with a 50Å thick vacuum in between to avoid interaction between two surfaces. The designated pore width is in the range of the cement phases pore size that ranges from 50Å to 100Å, as proposed by Mindess *et al*. [188]. For 14Å tobermorite and jennite, the tetrahedral SiO$_4$ and the octahedral CaO$_6$ surfaces were facing the vacuum; for ettringite, the tetrahedral SO$_4$ and the octahedral CaO$_6$ surfaces were facing the vacuum. After the supercells were built, water molecules, K$^+$ ions, and TcO$_4^-$ ions were packed into the vacuum with the density indicated in (Table 5.1). Periodic boundary conditions (PBC) were applied in all three dimensions.

Table 5.2. Crystallographic lattice parameters of simulated crystalline structures.

	Ettringite	14Å Tobermorite	Jennite
a/ Å	22.31	26.94	31.73
b/ Å	29.21	29.70	21.78
c/ Å	21.71	27.99	21.86
α/deg	101.08	90.0	101.3
β/deg	92.83	90.0	96.98
γ/deg	89.98	123.25	109.65

5.2.2 *Forcefield*

In the present work, the CLAYFF forcefield [126] was used to describe the atomic interactions in the crystalline structures and their interactions with the aqueous solution. This forcefield has been successfully used to simulate the structure and dynamic properties of hydrated mineral systems and their interfaces with aqueous solutions [189]. Prior MD studies concerning a variety of cement phases, such as portlandite and tobermorites, demonstrated that the CLAYFF forcefield could provide reliable results for the structure and dynamic properties of the C-S-H gel, although the forcefield was not initially designed for cement systems [36]. However, the CLAYFF forcefield does not contain forcefield parameters for TcO_4^- ions [190] and sulfate groups [191] in ettringite. Relevant parameters were found in literature and incorporated into the CLAYFF forcefield to perform MD simulations (Table 5.3).

Table 5.3. Forcefield parameters for TcO_4^- and SO_4^{2-} [44].

Nonbond parameters for TcO_4^- and SO_4^{2-}

Atom type	symbol	q_i	ϵ_{ii} (kcal/mol)	σ_{ii} (Å)
Tc in TcO_4^-	Tc	+2.720	1.0080	2.6550
O in TcO_4^-	Otc	−0.930	0.2090	3.8600
S in SO_4^{2-}	so	+2.300	0.8370	3.5500
O in SO_4^{2-}	os	−1.075	0.6500	3.2500

Bond parameters for the TcO_4^- and SO_4^{2-}

Bond Stretch

atom i	atom j	k_1 (kcal/mol Å^2)	r_o (Å)
Tc	Otc	2094.5	1.0000
so	os	2198.7	1.4870

Angle Bend

atom i	atom j	atom k	k_2 (kcal/mol rad^2)	θ_o (deg)
Otc	Tc	Otc	585.8	109.47
os	so	os	585.8	109.47

5.2.3 Computational Methods

MD simulations were performed using Materials Studio software (Accelrys, Inc., San Diego, CA). The crystalline structures were first geometrically optimized, then $KTcO_4$ solution was packed in to the 50Å pore space between the two solid phase layers. After geometry optimization of each constructed computational cells, 400 ps of NPT-ensemble MD simulations were employed to relax the computational cells. A portion of the solid structure located 6Å below the interface was then constrained and maintained fixed during the simulation to decrease the simulation time. Meanwhile, the impact of interfacial interaction on the surface structure could be investigated with the free near surface solid layer method. Each energy minimized computational

cell was then subjected to an NVT-ensemble of MD simulations of 1 ns with a time step of 1.0 fs at 298K for thermodynamic equilibration. The dynamic trajectory was then recorded at 100-fs intervals for an additional 20 ns of NVT-ensemble MD simulation.

5.2.4 Data Analysis

The equilibration status of each trajectory was determined by calculating the Root Mean Square Displacement (RMSD) of the atoms located in the first layer of the CaO_6 surfaces and the aqueous species (*i.e.* TcO_4^- ions) in solution [149,153]. Particularly, the RMSD in the *z*-direction was evaluated because the movement of ions in the *z*-direction is associated with the adsorption-desorption process. The first layer atoms on the CaO_6 surfaces of 14Å tobermorite and jennite included all the hydroxyl oxygen, bridging oxygen with tetrahedral substitution, and silica ions at the surface in the first layer of silicate chains, as well as interlayer Ca ions at the interface. The first layer atoms on the CaO_6 surface of ettringite included all the sulfur and aluminum atoms in the first layer of SO_4 and AlO_6 groups, as well as interlayer Ca ions at the interface. The equilibration of the interface was determined by the plateau of the RMSD curves in the *z*-direction. The systems were assumed to have reached equilibrium by the end of the simulation (*i.e.* the final part of each RMSD curve was assumed to be part of a plateau that could be represented as a mean with random error). The data acquisition trajectories were segmented to a series of 1-ns segments (10,000 frames) at a running 0.1-ns interval (1,000 frames) from the end of the simulation (where equilibrium was assumed) back to the beginning. This process generated 190 piece-wise trajectory segments that overlapped. The interval mean was calculated for each trajectory segment (*i.e.* 10,000 points). The running mean (*i.e.* the mean calculated from the last frame of the data acquisition trajectory to the first frame of the selected trajectory segment) was compared to the interval mean, up to the last crossover point between the running mean curve and the raw RMSD curve. The last crossover point (relative to the end of the simulation) was assumed to represent the approximate beginning of the plateau. Typically, a statistical test on the difference in means (running versus interval) could be used to identify the beginning of the plateau (*i.e.* when the means are significantly different); however, the results of any such statistical test (*e.g.* a t-test at a 5% significance level) would indicate that the beginning of the plateau was proximate to the selected crossover point because of the large numbers of RMSD points used to estimate the running and interval means. Furthermore, selecting the last crossover point instead of the actual beginning of the plateau that would be obtained using a statistical test would not significantly change the

statistics for the plateau. The end of the trajectory segment that corresponds to the last crossover point was used to define the beginning of the plateau.

Relative atomic density profiles were computed along the (0 0 1) direction (*i.e.* perpendicular to the solid/aqueous solution interface) to determine the occurrence of adsorption and to define the inner-sphere and outer-sphere regions beyond the interface. Relative atomic density profiles were averaged over the equilibrated phase of trajectories. The first layer of O atoms in the solid structure was used to define the solid surface. For the three cement phases, the oxygen of hydroxyl groups was chosen as the marker for the surface. The interactions of TcO_4^- ions with the cement phases were analyzed in terms of inner-sphere and outer-sphere adsorption. Inner-sphere adsorption was considered as the adsorption mechanism when the ions bind directly to the surface with no intervening water molecules and little mobility in the plane parallel to the surface for a long simulation period (700 ps) (*e.g.* >500ps in literature [169]). Outer-sphere adsorption was characterized by the presence of intermediate water molecules between the ions and the surface, and the complexes stayed in the outer-sphere region longer than 250 ps. The inner-sphere and outer-sphere regions were determined by comparing the location of the relative atomic density profiles of the Tc ion in TcO_4^- ions and O in water molecules. The residence time of the inner-sphere and out-sphere complex were studied by plotting the *z*-coordinates of Tc in each TcO_4^- ion as a function of time.

Radial distribution functions (RDF) were calculated the along the *z*-direction between Tc in TcO_4^- ions and bridging O (Tc-Ob), hydroxyl O (Tc-Oh), bridging O with tetrahedral substitution (Tc-Obts), and Ca (Tc-Ca) for stable inner-sphere complexes. Due to the structure of TcO_4^- ions, the RDFs between O in TcO_4^- ions and Ca (Otc-Ca) were also analyzed to study the configuration of complexes. Then for each model, overall RDFs of each pair were plotted by averaging corresponding RDFs of each inner-sphere adsorption event. Overall Coordination Numbers (CN) were averaged by the CN of each frame from qualified events. RDFs and CNs for outer-sphere complexes were analyzed in the same way as for inner-sphere complexes. Instead of structural O (*i.e.* Ob, Oh, Obts), the configuration of outer-sphere complex was analyzed between Tc and O in water molecules (Tc-O*), and the corresponding CNs were calculated.

To have an estimate of how energetically favorable it was to form a complex at the surface of different cement phases, the adsorption energies for inner-sphere and outer-sphere complexes

were compared to the hydration energies. Overall adsorption energies were averaged from all the adsorption events, and corresponding standard deviations were calculated. The calculation of the adsorption energy was computationally expensive. For statistical reliability, different types of inner-sphere adsorption events and outer-sphere adsorption events (before co-ion adsorption vs. after co-ion adsorption, type 1 outer-sphere adsorption vs. type 2 outer-sphere adsorption (Figure 3.16 and Figure 3.17)) were sampled for 1 ns, and the adsorption energy was calculated for each frame. Over this period of data collection, 10,000 points were collected. To determine how many points must be sampled from this data set to yield a representative population, a series of Monte Carlo analyses were performed. A 100 out of 10,000 points sampling strategy was proposed. Monte Carlo analyses were performed by randomly sampling 100 points from this data set for 10,000 times. The results indicated that for 10,000 random samples of 100 points, the difference of the averaged adsorption energy of each random sampling compared to the overall averaged interaction energy was less than 3%. Although the standard deviation of each random sampling showed significant variation compared to the overall standard deviation, the standard deviation was small with respect to the interaction energy (*i.e.* less than 20%). Therefore, the combination of the averaged value and standard deviation for a random sample can well represent the overall data. Therefore, for each stable adsorption event, the adsorption energy was calculated every 10 ps (*i.e.* every 100 frames), and the corresponding standard deviation was also calculated. This procedure was performed for every qualified event; then the overall adsorption energy was averaged from all the qualified events and the corresponding standard deviation was calculated.

Dynamic properties, including the diffusion coefficients of stable complexes in the cement phase/aqueous solution systems were calculated by mean square displacement (MSD) to provide information about the mobility for complexes at different distances (inner-sphere region, outer-sphere region, and bulk solution) from the surface. Diffusion coefficients were averaged from that of each qualified event, and standard deviations were also calculated.

5.3   Results and Discussion

5.3.1   *Equilibrium of the System*

The equilibrium of each model was evaluated by calculating the RMSD of the first layer elements and surface species (Figure 5.2). The RMSD in the *z*-direction of each system, which represented the adsorption - desorption process, approached a plateau at ~14 ns. The results

indicated that the 0.2M $KTcO_4$/14Å tobermorite system reached equilibrium at ~11.5 ns, 0.2M $KTcO_4$/jennite system reached equilibrium at ~12.5 ns, and 0.2M $KTcO_4$/ettringite system reached equilibrium at ~11.0 ns. For consistency, only the last 6 ns of trajectories of all the systems were collected for data analysis.
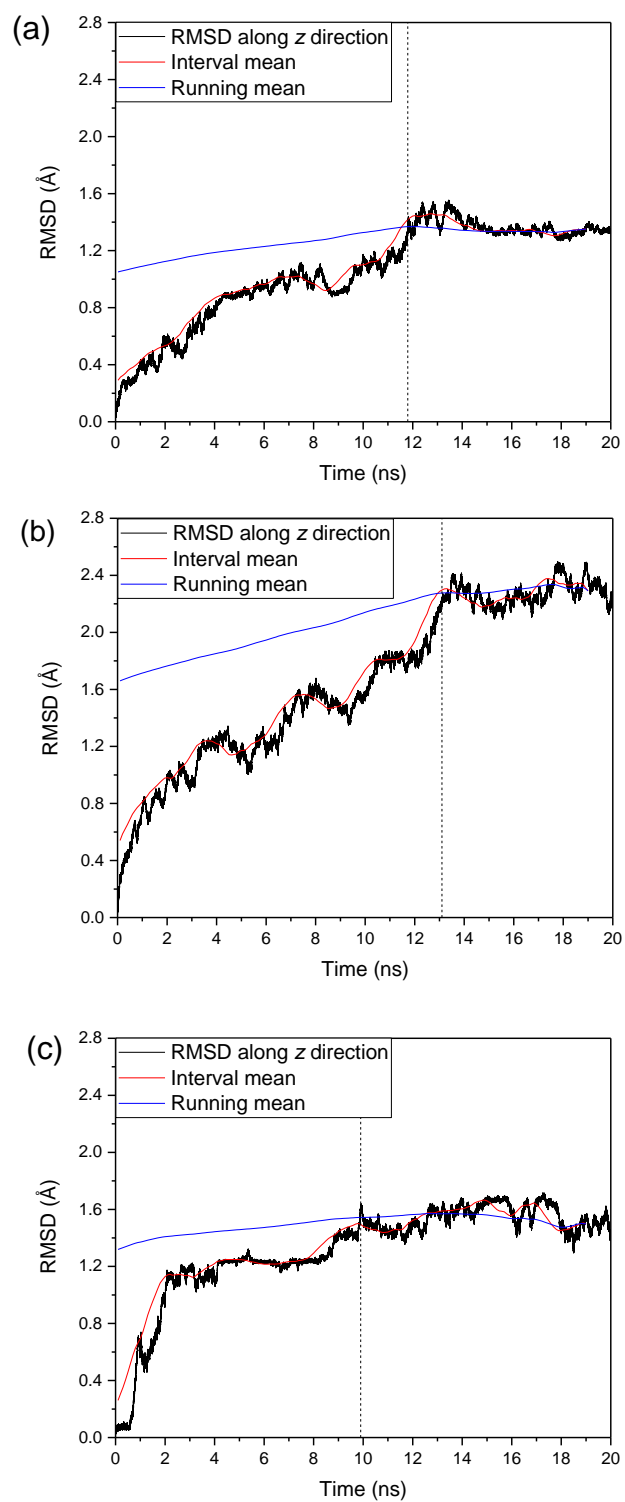
Figure 5.2. RMSD along the *z*-direction, and corresponding interval mean and running mean for TcO$_4^-$ ions and the first layer of surface element: (a) 14Å tobermorite, (b) jennite, and (c) ettringite.

5.3.2   Relative Atomic Density Profiles and Identification of Inner-Sphere and Outer-Sphere Complexes

Due to the limited size of each computational cell, only four or five TcO_4^- ions were included in each model. The results showed that, for 0.2M $KTcO_4$/14Å tobermorite, only one TcO_4^- ion formed a stable inner-sphere Tc complex and two TcO_4^- ions were adsorbed as the outer-sphere complexes; for 0.2M $KTcO_4$/ettringite, all the five TcO_4^- ions formed stable outer-sphere complexes.

The relative atomic density profiles indicated the adsorption capacity of TcO_4^- at the surfaces of different cement phases. The profiles represented the collective atomic structures in equilibrium with 0.2M $KTcO_4$ structure (Figure 5.3). On the octahedral CaO_6 surfaces of 14Å tobermorite, two major peaks were observed, which indicated that at least two types of Tc complexes were adsorbed on the surface. There was a shoulder on the second peak, which indicated that either the adsorption was not stable or there were two subcategories of complexes in this region. Some K^+ ions diffused into the octahedral CaO_6 surface area of 14Å tobermorite; a pronounced K peak was observed, which indicated that the adsorption of TcO_4^- ions on the octahedral CaO_6 surface might be due to the co-ion effect. On the octahedral CaO_6 surface of ettringite, only one major peak was observed; however, the distance between the surface and the highest point of the peak was about 3 Å. This distance was big enough to accommodate a layer of water molecules, which indicated that TcO_4^- may have formed outer-sphere complexes on the surface of ettringite, and the Tc complexes might include water molecules. On the octahedral CaO_6 surface of jennite, no surface complexes were observed, and the relative atomic density profile of Tc was evenly distributed along the *z*-direction of the liquid phase, which indicated that the affinity of TcO_4^- ions to the surface of jennite was weak.

Adsorption of K^+ ions on the tetrahedral SiO_4 surface of 14Å tobermorite and jennite was observed. The high peak of the K profile on the tetrahedral SiO_4 surface of 14Å tobermorite indicated strong interaction between K^+ ions and the surfaces. However, the interaction between K^+ ions and jennite was weak. On the tetrahedral SO_4 surface of ettringite, several major peaks were observed near the surface area, which indicated strong interactions. However, sulfate leaked into the aqueous phase; therefore, it was impossible to define the surface. The adsorption of K^+

ions on the surface of cement phases was not the main interest of the present work. Therefore, no further analysis was conducted on the tetrahedral SiO_4/SO_4 surfaces.
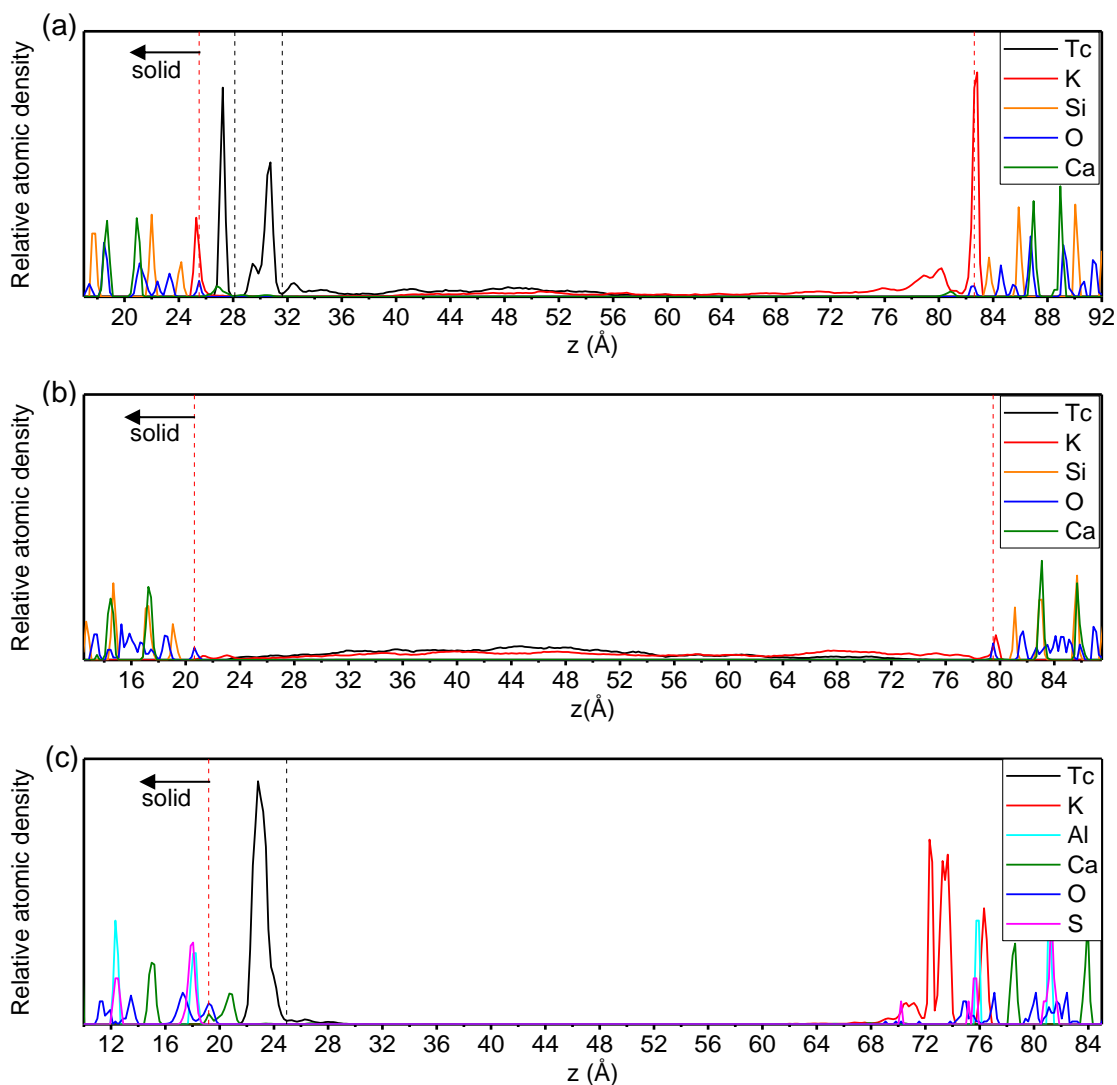
Figure 5.3. Relative atomic density profiles for three systems: (a) 0.2M $KTcO_4$/14Å tobermorite; (b) 0.2M $KTcO_4$/jennite; and (c) 0.2M $KTcO_4$/ettringite. Note that the surfaces were shown by red dash lines; black dash lines represented the lowest point of the first few peaks from the surfaces.

On the octahedral CaO_6 surface of 14Å tobermorite and ettringite, relative atomic density profiles of Tc ions were zoomed in and combined with the relative atomic density profiles of O in water molecules to identify the inner-sphere complexes and outer-sphere complexes on the surfaces (Figure 5.4). The relative atomic density profile of O in water molecules showed no peak

between the surface and the first peak of Tc on the surface of 14Å tobermorite, and there was at least one peak of water O between the surface and the second major Tc peak. These results indicated that near the surface of 14Å tobermorite, TcO_4^- ions formed both inner-sphere and outer-sphere complexes. The tails of Tc profile indicated that surface Tc complexes had a chance to diffuse out of the surface area to the bulk solution. On the other hand, on the surface of ettringite, there was an obvious peak of water O between the surface and the Tc profile, which indicated that on the surface of ettringite, TcO_4^- ions only generated outer-sphere complexes.
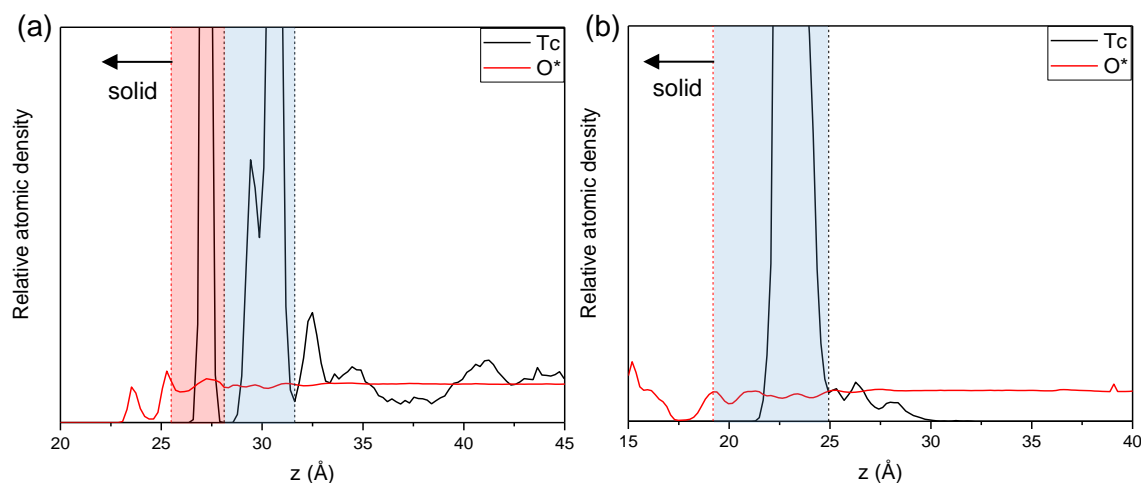
Figure 5.4. Relative atomic density profiles of Tc ion and O in water molecules at the surface of: (a) 14Å tobermorite and (b) ettringite. The inner-sphere region was highlighted in red, and the outer-sphere region was highlighted in blue.

5.3.3   Structural Properties of Tc Complexes on the Surface of 14Å Tobermorite

K^+ ions approached the octahedral CaO_6 surface of 14Å tobermorite at 17.2 ns after data acquisition started. The relative atomic density profiles of Tc ions in TcO_4^- and K^+ ions within different time frames were plotted to compare the influence of K^+ ions on the adsorption of TcO_4^- ions (Figure 5.5). The results indicated that the presence of K^+ ions on the surface did not affect the distance between the inner-sphere Tc complex and the surface. However, K^+ ions on the surface pushed the outer-sphere complexes ~1.1Å further away from the surface. The presence of K^+ ions on the surface also attracted the Tc complexes from the bulk solution into the outer-sphere region, as evidenced by the merging of the second and third peaks after the adsorption of K^+ ions. The

results indicated that there might be two types of outer-sphere Tc complexes in the surface area of 14Å tobermorite.
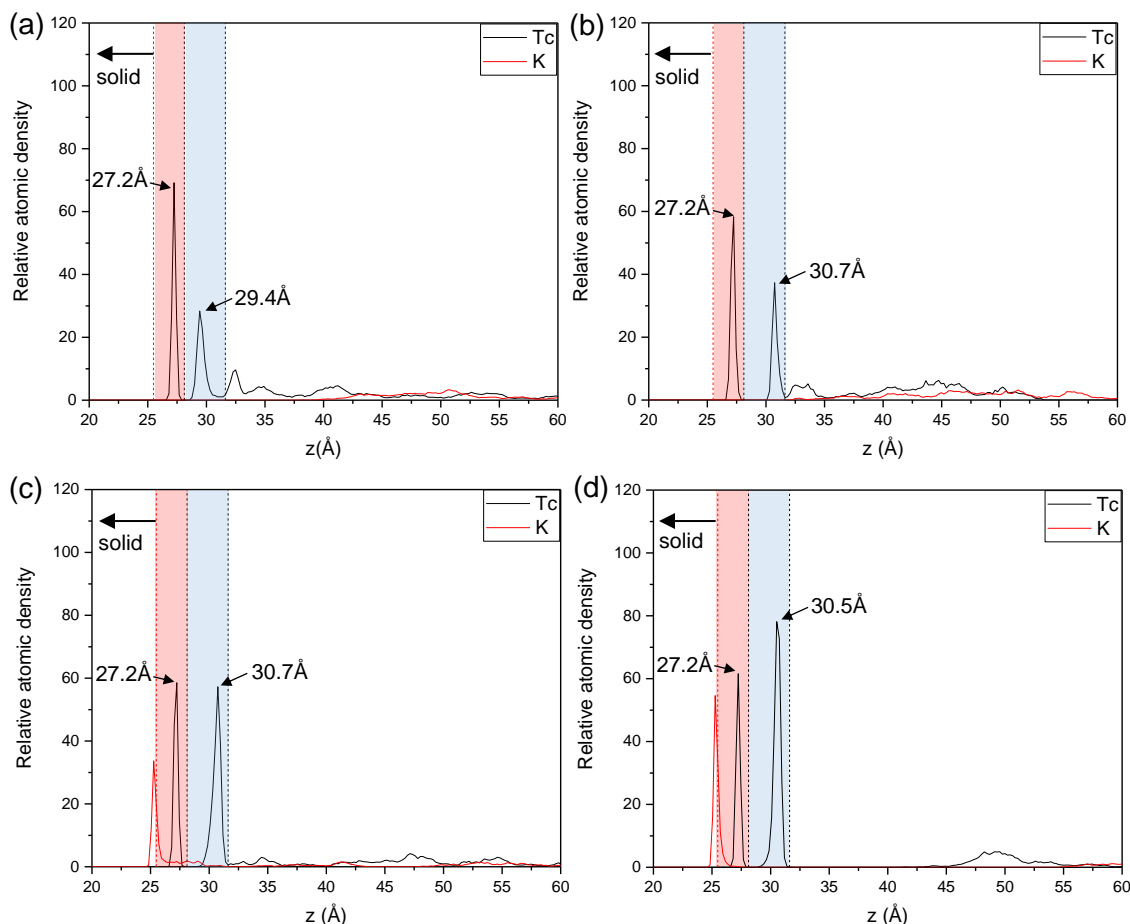
Figure 5.5. The evolution of the location of Tc ion and K$^+$ ions between: (a) 14-16 ns, (b) 16-17 ns, (c) 17-18 ns, and (d) 18-20 ns. Note that K$^+$ ions arrived at the surface area at 17.2 ns after the data acquisition started. The inner-sphere region was highlighted in red, and the outer-sphere region was highlighted in blue.

5.3.3.1 Inner-sphere Tc Complex

The radial distribution function (RDF), characteristic distance (R), and coordination number (CN) provided more specific information on the structures of complexes. For the inner-sphere Tc complex, RDFs were plotted between Tc ions (Tc) and O ions in TcO$_4^-$ groups (Otc), different structural O (Obts, Ob, and Oh), O in water molecules (O*), and Ca ions to investigate the structure of inner-sphere Tc complex. The RDF results indicated that the inner-sphere Tc complex included TcO$_4^-$, bridging O with tetrahedral substitution (Obts), and Ca ions (Figure 5.6).

100

The TcO$_4^-$ ion has non-polar tetrahedral geometry in vacuum, which is in sp^3 hybridization. However, the TcO$_4^-$ ion in the inner-sphere Tc complex was strongly polar; the Tc ion was relocated to the apex in a tetragonal pyramid geometry. The angles between the dipole moment of TcO$_4^-$ and the normal vector of surface were ~140° (Figure 5.7), which indicated that the TcO$_4^-$ ions had dipole moment pointing towards the surface; the Tc ions were located closer to the surface and the Otc atoms were located further away from the surface. RDF and CN results indicated that in the inner-sphere Tc complex, the Tc ion at the apex of TcO$_4^-$ pyramid was coordinated with 1 Obts atom at the surface, and the distance between the Tc ion and the Obts atom was 2.287 ± 0.053Å. The Ca ions were located closer to the Otc atoms. The Tc ion coordinated with 3-4 Ca ions (Figure 5.6). Co-ion adsorption did not affect the distance between the inner-sphere Tc complex and the surface; however, it significantly affected the structure of the inner-sphere Tc complex.
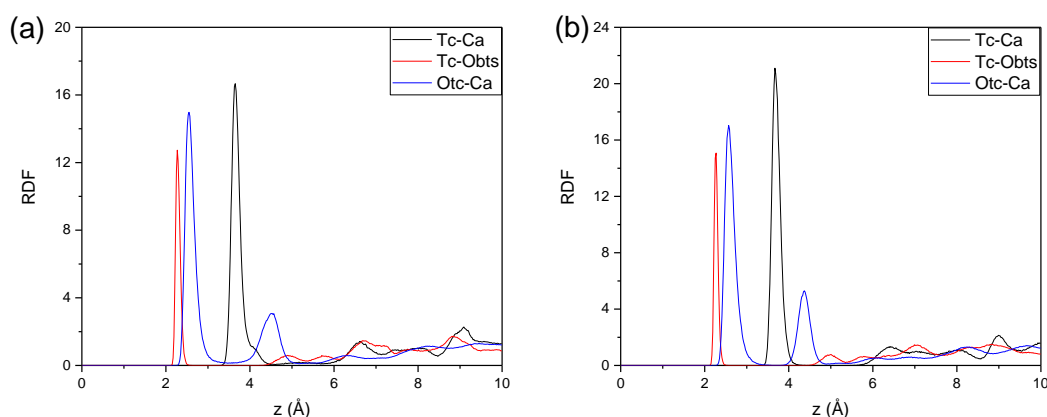
Figure 5.6. RDFs of the inner-sphere Tc complex on the surface of 14Å tobermorite: (a) before co-ion adsorption and (b) after co-ion adsorption.
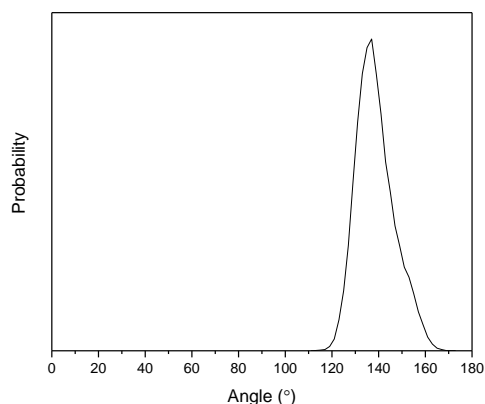
Figure 5.7. Orientation of the dipole moment of the inner-sphere Tc complex on the surface of 14Å tobermorite. Note that dipole moment points from negative charge to positive charge in physics by convention.

The major influence of co-ion adsorption on the structure of inner-sphere Tc complex was the configuration of Ca ions in the complex. Before the occurrence of co-ion adsorption, the Tc ion coordinated with 3-4 Ca ions (in most cases, 3 Ca ions), which was evidenced by the shoulder of the first peak of Tc-Ca RDF curve (Figure 5.6a). These 3 Ca ions were located beneath the base of the tetragonal TcO_4^- pyramid and formed an irregular tetrahedron with Tc (Figure 5.8a, b and c, Table 5.4). After K^+ ions were adsorbed on the surface, the inner-sphere complex contained 4 Ca ions. These Ca ions were located beneath the base of the tetragonal TcO_4^- pyramid and formed a square pyramid with the Tc ion (Figure 5.8d, e and f, Table 5.4).

The configurations of TcO_4^- ions in the inner-sphere Tc complex were almost identical before and after co-ion adsorption. The TcO_4^- ions were in a square pyramid configuration, although the Otc-Tc-Otc edge angles showed more variation with each other before co-ion adsorption. The Tc-Otc bonds in the inner-sphere complex were longer than those in equilibrated TcO_4^- tetrahedron in vacuum (1.704Å) [44], which indicated strong interaction between the Otc atoms and the Ca ions. The TcO_4^- ions in the inner-sphere Tc complex were strongly polar, with dipole moments up to 11.6 Debye (D) (Table 5.4).

102

Table 5.4. Geometry of the inner-sphere Tc complex on the surface of 14Å tobermorite.

	before co-ion adsorption	after co-ion adsorption
Tc-Otc bond length (Å)	1.714 ± 0.016	1.712 ± 0.017
Otc-Tc-Otc Angles (°)	78.84 ± 2.23	78.77 ± 2.01
angle 1	80.16 ± 2.06	78.73 ± 1.99
angle 2	77.62 ± 2.00	78.64 ± 2.01
angle 3	78.65 ± 2.05	78.66 ± 2.00
angle 4	78.95 ± 2.05	79.08 ± 2.00
Tc-Ca distance (Å)	3.67 ± 0.11	3.72 ± 0.11
Ca-Tc-Ca Angles (°)		65.11 ± 3.25
angle 1	72.68 ± 4.85	65.99 ± 2.95
angle 2	130.77 ± 7.31	63.55 ± 2.94
angle 3	80.68 ± 5.15	65.59 ± 3.28
angle 4	N/A	65.34 ± 3.26
Dipole moment (Debye)	11.65 ± 0.23	11.69 ± 0.23
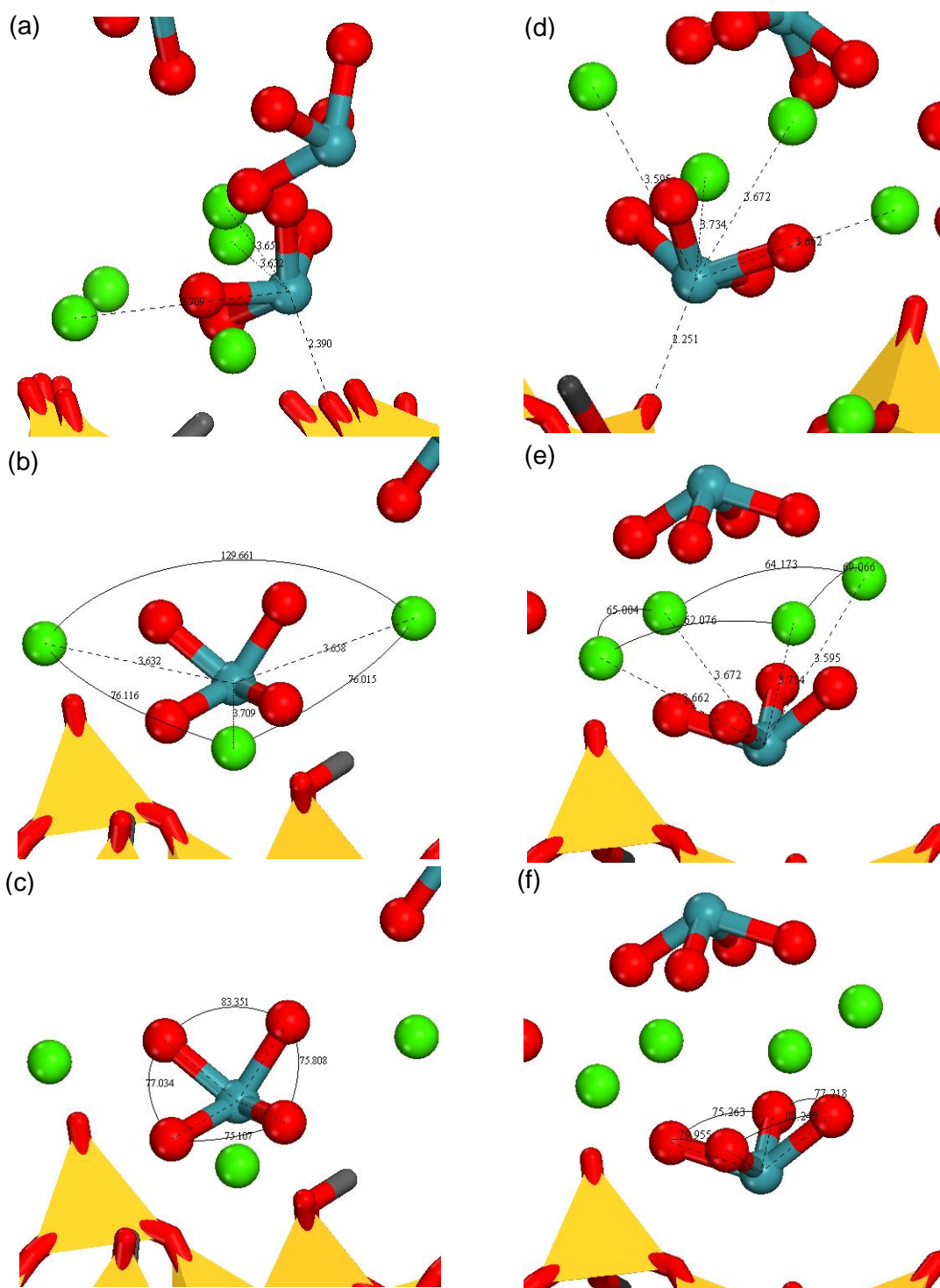
Figure 5.8. Snapshots of the local structure of inner-sphere Tc complexes before co-ion adsorption on the surface of 14Å tobermorite: (a) the distance between Tc and Obts, Tc and Ca; (b) the Ca-Tc-Ca angles; and (c) the Otc-Tc-Otc angles. After co-ion adsorption: (d) the distance between Tc and Obts, Tc and Ca; (e) the Ca-Tc-Ca angles; and (f) the Otc-Tc-Otc angles. For a clear view, water molecules were not shown. Legend: blue – Tc, red – O, green – Ca, yellow – Si.

5.3.3.2 Outer-sphere Tc Complex

The outer-sphere Tc complex was classified based on the geometry of the TcO_4^- ion in the complex. Two types of outer-sphere complexes were identified. The outer-sphere Tc complex type 1 had the TcO_4^- ion in tetragonal pyramid geometry and the outer-sphere Tc complex type 2 had the TcO_4^- ion in tetrahedral geometry.

The configuration of the outer-sphere Tc complex type 1 was affected by co-ion adsorption. Before co-ion adsorption, the outer-sphere Tc complex type 1 coordinated with 2 water O in the first hydration shell and with 2-3 Ca ions in the first Ca coordination shell (*i.e.* in most cases, 2 Ca ions). A second Ca coordination shell was also observed (Figure 5.9a). The outer-sphere Tc complex type 1 that formed after co-ion adsorption only had one Ca coordination shell with 3 Ca ions (Figure 5.9b). Instead of coordinating with the Obts atom in the inner-sphere Tc complex, the Tc ion in the outer-sphere Tc complex 1 coordinated with two water molecules through O, before and after co-ion adsorption. Co-ion adsorption affected the charge balance of the surface, which changed the angular orientation for the dipole moment of the TcO_4^- ion from 40° to 140° (Figure 5.10).
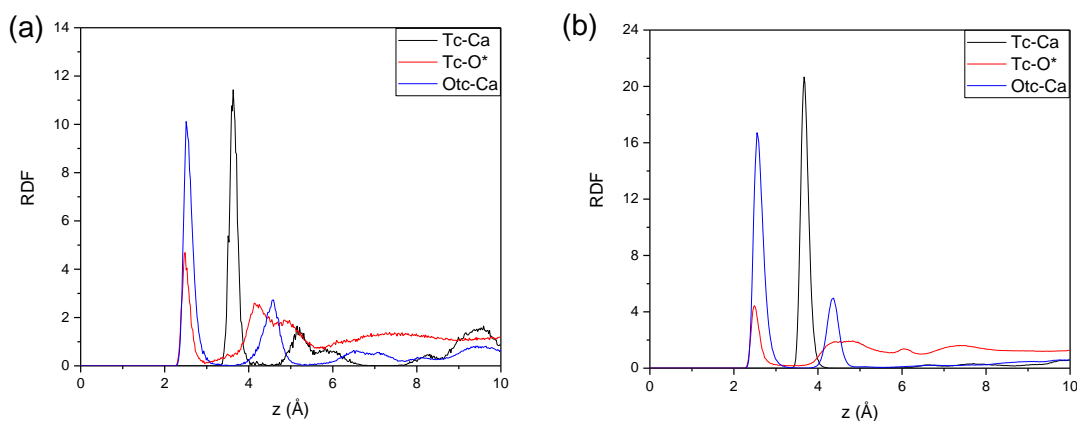
Figure 5.9. RDF of the outer-sphere Tc complex type 1: (a) before K^+ co-ion adsorption and (b) after K^+ co-ion adsorption.
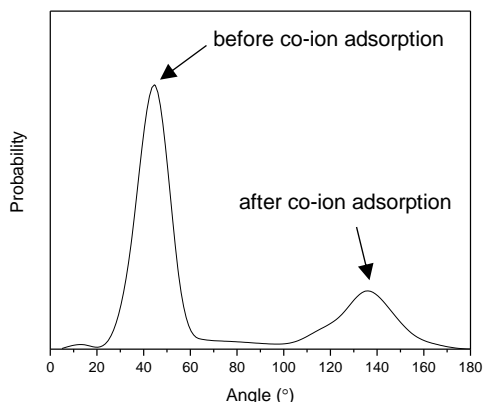
Figure 5.10. Orientation of the dipole moment of the outer-sphere Tc complex type 1 on the surface of 14Å tobermorite. Note that dipole moment points from negative charge to positive charge in physics by convention.

Local structure and configuration statistical analysis indicated that before co-ion adsorption, 2 Ca ions were located beneath the base of the TcO_4^- pyramid. In the case when a third Ca ion coordinated, the third Ca ion was located further away from the Tc ion compared to the other 2 Ca ions and was located above the base of TcO_4^- pyramid (Figure 5.11). The Tc atom in the TcO_4^- ions coordinated with the O atom in water molecules (Figure 5.11).

The co-ion adsorption of K^+ ions occupied surface sites and pushed the outer-sphere Tc complex type 1 away from the surface and changed the structure of the complex (Figure 5.12). The TcO_4^- ion in the outer-sphere Tc complex type 1 kept tetragonal pyramid geometry. The apex Tc ion coordinated with 2 water molecules in the first hydration shell. Three (3) Ca ions were located beneath the base of TcO_4^- pyramid and formed an irregular tetrahedron with the Tc ion (Figure 5.12).

Figure 5.11. Snapshots of the local structure of outer-sphere Tc complex type 1 before co-ion adsorption on the octahedral CaO_6 surface of 14Å tobermorite: (a) the distance between Tc and water O, Tc, and Ca; (b) the Otc-Tc-Otc angles. For a clear view, water molecules are not shown. Legend: blue – Tc, red – O, green – Ca, yellow – Si, grey – H.

Figure 5.12. Snapshots of the local structure of outer-sphere Tc complex type 1 after co-ion adsorption on the octahedral CaO$_6$ surface of 14Å tobermorite: (a) the distance between Tc and water O, Tc, and Ca; (b) the Ca-Tc-Ca angles; and (c) the Otc-Tc-Otc angles. For a clear view, water molecules are not shown. Legend: blue – Tc, red – O, green – Ca, yellow – Si, grey – H.

Like the inner-sphere Tc complex, the TcO_4^- ion in the outer-sphere Tc complex type 1 was in a square pyramid configuration, which was not significantly affected by co-ion adsorption. The Otc-Tc-Otc edge angles showed more variation with each other before co-ion adsorption. In the outer-sphere complex type 1, the Tc-Otc bonds were longer than those in equilibrated TcO_4^- tetrahedron in vacuum (1.704Å) [44], which was attributed to the strong interaction between the Otc atom and the Ca ions. The TcO_4^- ions in the outer-sphere Tc complex type 1 were strongly polar with a dipole moment up to 11.6 Debye (D) (Table 5.5).

Table 5.5. Geometry of the outer-sphere Tc complex type 1 on the octahedral CaO_6 surface of 14Å tobermorite.

	before co-ion adsorption	after co-ion adsorption
Tc-Otc bond length (Å)	1.712 ± 0.016	1.712 ± 0.017
Otc-Tc-Otc Angles (°)	78.91 ± 2.28	78.69 ± 2.06
angle 1	78.09 ± 2.01	78.50 ± 2.02
angle 2	79.68 ± 2.11	78.69 ± 2.03
angle 3	77.81 ± 2.05	78.60 ± 2.03
angle 4	80.07 ± 2.06	78.98 ± 2.11
Tc-Ca distance (Å)	3.65 ± 0.11	3.70 ± 0.10
Ca-Tc-Ca Angles (°)		
angle 1	N/A	65.63 ± 3.24
angle 2	N/A	67.33 ± 3.87
angle 3	N/A	97.90 ± 3.93
Dipole moment (Debye)	11.63 ± 0.22	11.74 ± 0.22

The outer-sphere Tc complex type 2 contained 2 Ca ions in the first Ca coordination shell. A second Ca coordination was centered at 5.27Å. The first hydration shell of the complex contained 18.05 ± 0.45 water molecules (Figure 5.13), which indicated that the TcO_4^- ion was most likely fully hydrated.

Local structure and geometry statistical analysis indicated that the TcO_4^- ion kept the tetrahedral geometry, yet was slightly polar with a dipole moment equal to 0.43 ± 0.18 D. The weak polarity of the TcO_4^- ion was most likely due to the interaction with the ambient environment: unequal changes in the internal bond angles and bond lengths of the ion. Therefore, it was difficult to determine the angular orientation of the tetrahedral TcO_4^- ion. The length of the Tc-Otc bond was equal to 1.705 ± 0.017 Å, and the tedrahedral angles (edge central angle) were 109.45 ± 1.76 °. These values were almost identical to the values of bond length and tedrahedral angle when the

TcO$_4^-$ ion is in equilibrium in vacuum (1.705 Å and 109.47°). The Ca ions were located further away from the Tc ion in the TcO$_4^-$ group compared to the outer-sphere Tc complex type 1 (4.12 ± 0.21Å vs. 3.70 ± 0.10Å).

The TcO$_4^-$ ion in the outer-sphere Tc complex type 2 had similar geometry to that for the aqueous TcO$_4^-$ ion, and the characteristic distance (R) of the first hydration shell for both types of TcO$_4^-$ ion were comparable (4.35Å vs. 4.03Å) (Figure 5.13). However, the outer-sphere Tc complex type 2 contained many more water molecules in the first hydration shell compared to the aqueous TcO$_4^-$ ion (18.05 ± 0.45 vs. 5.76 ± 0.83 water molecules). The incorporation of Ca ions in the complex may affect the amount of water molecules, and the layered structure of water molecules in the surface region also contributed to the large amount of water molecules in the first hydration shell of the outer-sphere Tc complex type 2 (Figure 5.4). Although the first hydration numbers of the aqueous TcO$_4^-$ ion were comparable to the value found in other MD simulation (5.8), the characteristic distance (R) for the first hydration shell found in the present work was larger than the value found in the literature (4.03Å vs. 3.81Å [44]). The nature of hydration shell was affected by the counter-ions and the concentration of the solution. The concentration was particularly important as salt may form water-separated ion pairs and direct ion-pairs. In the present work, the relatively high concentrations resulted in competition with solute and solvent for the remaining water molecules, both reducing the total number of water molecules involved in first shell hydration and the shift of R [192].
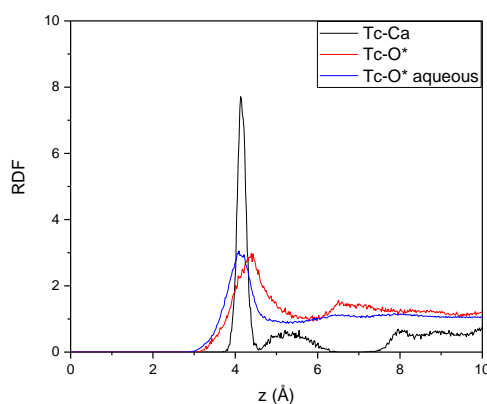
Figure 5.13. RDFs of the outer-sphere Tc complex type 2 on the octahedral CaO$_6$ surface of 14Å tobermorite and RDF for the aqueous TcO$_4^-$ ion.
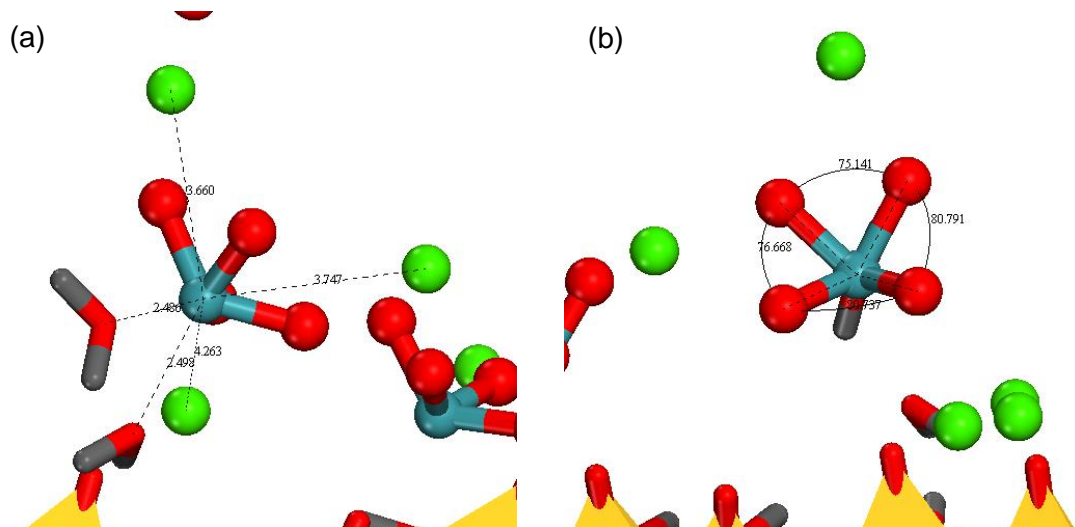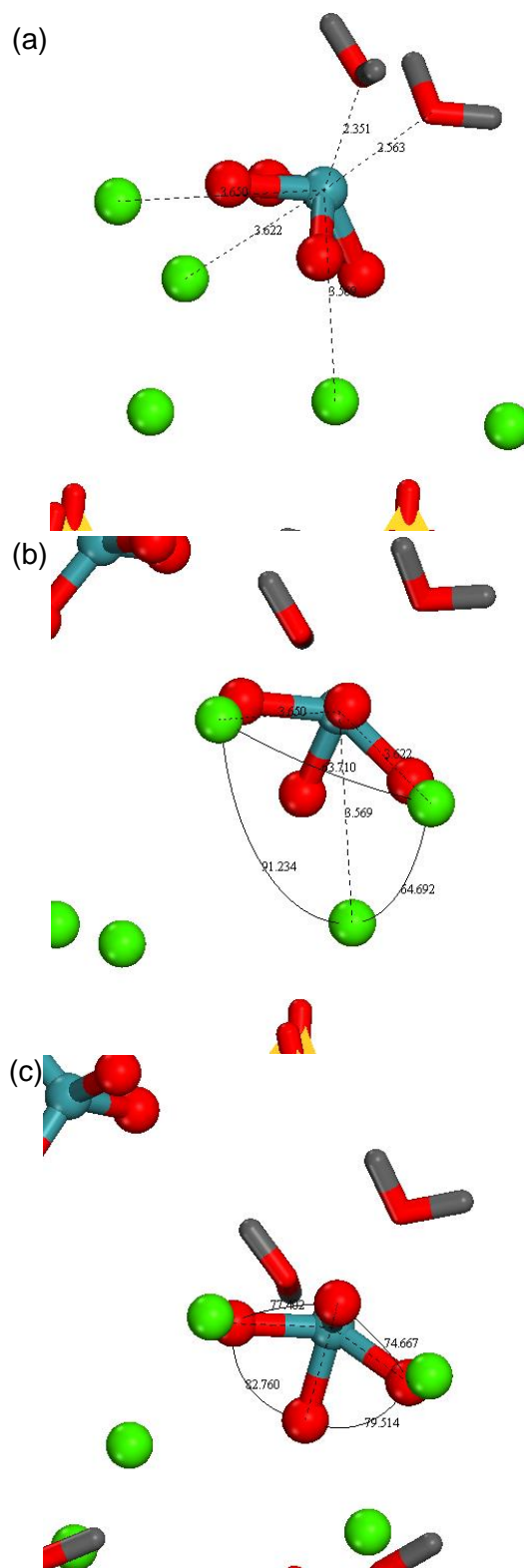
(a)   (b)

Figure 5.14. Snapshots of the local structure of outer-sphere Tc complex type 2 on the octahedral CaO_6 surface of 14Å tobermorite. Due to the large number of water molecules in the first hydration shell, water molecules are not shown for clarity. Legend: blue – Tc, red – O, green – Ca, yellow – Si, grey – H.

5.3.4   Structural Properties of Tc on the Octahedral CaO_6 Surface of Ettringite

RDFs were calculated between the Tc atom in TcO_4^- ions and the Ca ions (Tc-Ca), the Tc atom in TcO_4^- ions, and the O atom in H_2O molecules (Tc-O*) to investigate how Ca ions and H_2O molecules coordinated with the TcO_4^- ions. The results indicated that the TcO_4^- ions formed two types of outer-sphere complexes on the surface of ettringite like those on the surface of 14Å tobermorite: the outer-sphere Tc complex type 1 and the outer-sphere complex type 2.

The outer-sphere Tc complex type 1 contained 2 water molecules and 3 Ca ions: 3 Ca ions were located close to the Otc atoms, and the water molecules coordinated with the Tc ion through water O (Figure 5.15). The angles between the dipole moment of the outer-sphere complex type 1 and the normal vector of the surface were greater than 90°, which indicated that the TcO_4^- ion in the complex had the Tc ion pointing towards the surface. Two major peaks in the probability curves of the orientation were observed: one peak was located at 125° and another peak was located 165° (Figure 5.16). The change of the angular orientation of TcO_4^- ions was due to the movement of Ca ions associated with the TcO_4^- ion in the complex.
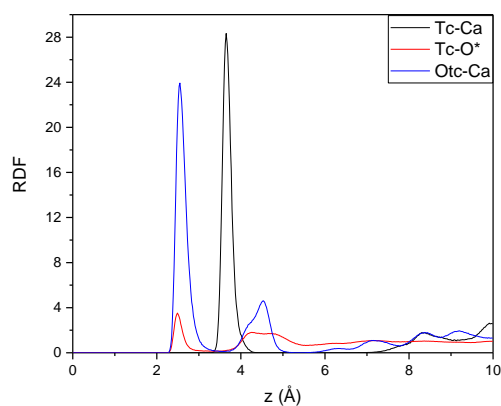
Figure 5.15. RDF of the outer-sphere Tc complex type 1 on the octahedral CaO_6 surface of ettringite.
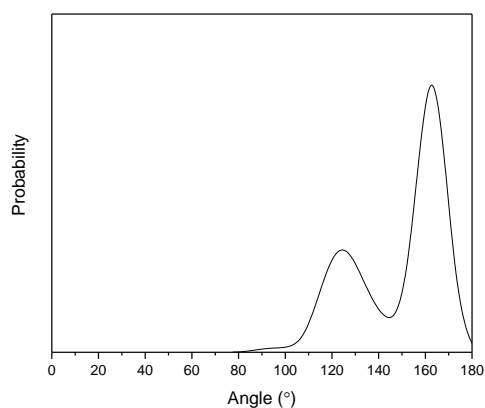
Figure 5.16. Orientation of the dipole moment of outer-sphere Tc complex type 1 on the octahedral CaO_6 surface of ettringite.

Local structure and geometry statistical analysis (Figure 5.17, Table 5.6) indicated that in the outer-sphere Tc complex type 1, the TcO_4^- ion was in a square pyramid geometry and was strongly polar with a dipole moment equal to 11.67 ± 0.22 D. The Ca ions were located beneath the base of the TcO_4^- square pyramid and formed an irregular tetrahedron with the Tc ion. The values of the Ca-Tc-Ca edge angles showed large fluctuations, which confirmed the two major peaks of the orientation of dipole moment for the TcO_4^- ion in the outer-sphere Tc complex type 1.

112
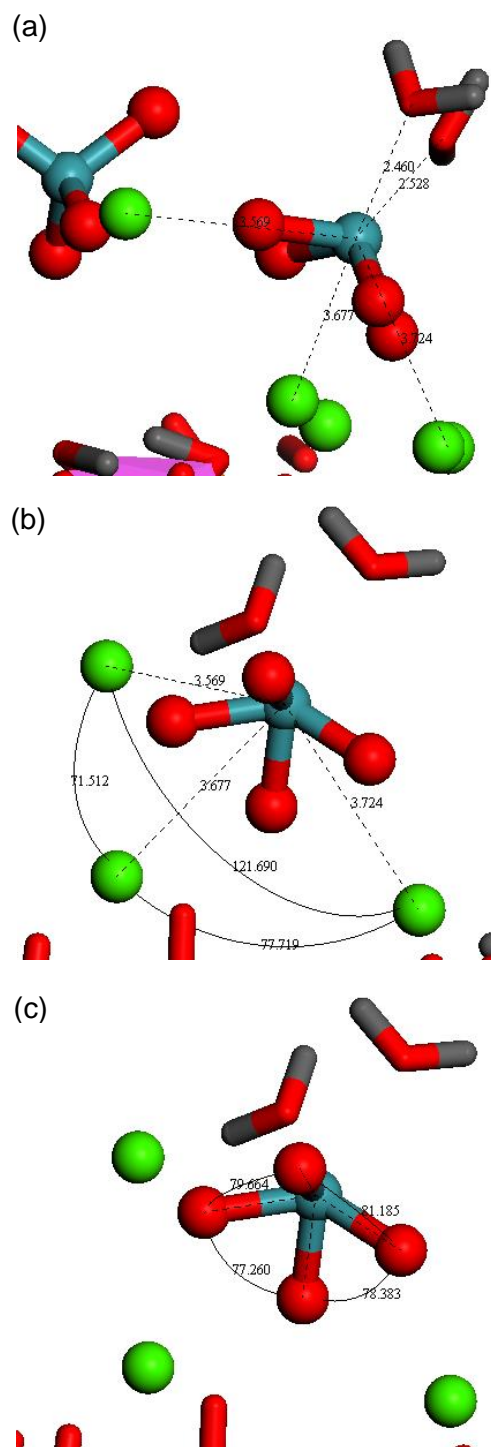
Figure 5.17. Snapshots of the local structure of outer-sphere Tc complex type 1 on the octahedral CaO_6 surface of ettringite: (a) the distance between Tc and water O, Tc, and Ca; (b) the Ca-Tc-Ca angles; and (c) the Otc-Tc-Otc angles. For a clear view, water molecules are not shown. Legend: blue – Tc, red – O, green – Ca, pink – Al, grey – H.

The outer-sphere Tc complex type 2 on the surface of ettringite had a similar structure to that on the octahedral CaO_6 surface of 14Å tobermorite: the Tc ion coordinated 2 Ca ions at about 4.1Å (*i.e.* R = 4.1Å) in the first Ca coordination shell. The Tc ion coordinated with 20.97 ± 0.37 water molecules in the first hydration shell, which indicated that the TcO_4^- ion in the outer-sphere complex type 2 was most likely fully hydrated (Figure 5.18).
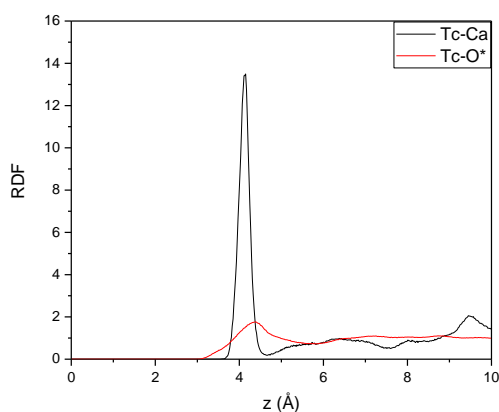
Figure 5.18. RDF of the outer-sphere Tc complex type 2 on the octahedral CaO_6 surface of ettringite.

Local structure and geometry statistical analysis (Figure 5.19, Table 5.6) indicated that the TcO_4^- ion in the outer-sphere Tc complex type 2 kept tetrahedral geometry; the length of Tc-Otc bonds and the values of tetrahedral angles in the outer-sphere Tc complex 2 were comparable with those in equilibrated TcO_4^- tetrahedron (1.705Å and 109.47°) [44]. The distances between the Tc ion and the Ca ions in the outer-sphere complex Tc type 2 were longer than those in the outer-sphere Tc complex type 1 (4.12 ± 0.12Å vs. 3.70 ± 0.13Å). The dipole moment of the TcO_4^- ion in the outer-sphere Tc complex type 2 was weak (Table 5.6), which was almost identical to the dipole moment of TcO_4^- tetrahedron in the bulk solution (0.43 ± 0.19D vs. 0.43 ± 0.18D).
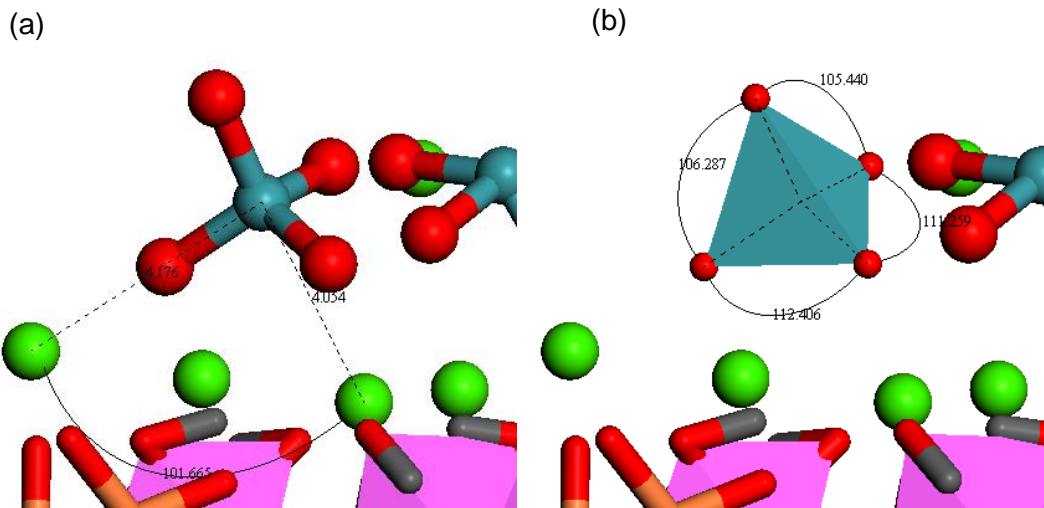
Figure 5.19. Snapshots of the local structure of outer-sphere Tc complex type 2 on the octahedral CaO_6 surface of ettringite: (a) Ca-Tc-Ca angle, (b) Otc-Tc-Otc angle. Due to the large number of water molecules in the first hydration shell, water molecules are not illustrated. Legend: blue – Tc, red – O, green – Ca, pink – Al, grey – H.

Table 5.6. Geometry for the outer-sphere Tc complexes on the octahedral CaO_6 surface of ettringite.

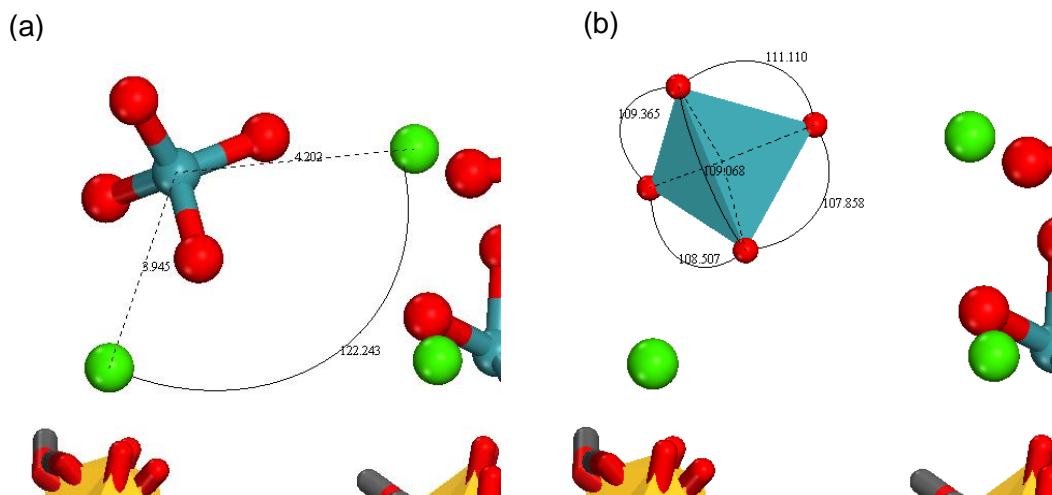|	outer-sphere complex type 1	outer-sphere complex type 2
Tc-Otc bond length (Å)	1.713 ± 0.017	1.705 ± 0.017
Otc-Tc-Otc edge angles (°)	78.82 ± 2.16	N/A
Otc-Tc-Otc tetrahedral angles (°)	N/A	109.46 ± 1.76
Tc-Ca distance (Å)	3.70 ± 0.13	4.12 ± 0.12
Ca-Tc-Ca Angles (°)		
angle 1	87.86 ± 14.39	N/A
angle 2	87.93 ± 18.09	N/A
angle 3	77.04 ± 5.08	N/A
Dipole moment (Debye)	11.67 ± 0.22	0.43 ± 0.19

5.3.5 *Adsorption Energy and Hydration Energy*

The adsorption energy for the inner and outer-sphere TcO_4^- ions at the surfaces of 14Å tobermorite and ettringite were compared to the hydration energy to determine the adsorption capacity of cement phases (Figure 5.20). The results showed that for 14Å tobermorite and ettringite, the adsorption energy of TcO_4^- ion at the octahedral CaO_6 surface (-489 ± 34 kcal/mol for inner-sphere Tc complex type 1, -602 ± 17 kcal/mol for inner-sphere Tc complex type 2, -393 ± 14 kcal/mol for outer-sphere Tc complex type 1 before co-ion adsorption, -496 ± 42 kcal/mol

115

for outer-sphere Tc complex type 1 after co-ion adsorption, -263 ± 16 kcal/mol for outer-sphere Tc complex type 2) was more negative than the hydration energy of TcO_4^- ion (-56 kcal/mol), which indicated that the adsorption was energetically favorable at the surfaces of 14Å tobermorite and ettringite. The adsorption energies between the TcO_4^- ions and 14Å tobermorite and the TcO_4^- ions and ettringite followed the sequence: inner-sphere Tc complex < outer-sphere Tc complex type 1 < outer-sphere Tc complex type 2.

For 14Å tobermorite, both the inner-sphere Tc complex and outer-sphere complex type 1 were affected by co-ion adsorption, and the adsorption energies for the TcO_4^- ions in both categories of complexes decreased after the co-ion adsorption when compared to adsorption energies for corresponding TcO_4^- ions before co-ion adsorption. Both inner-sphere Tc complex and outer-sphere Tc complex type 1 contained one more Ca ion after co-ion adsorption, which indicated that the Ca ions played an important role on the adsorption of the TcO_4^- ions to the surfaces of cement phases. The adsorption energy for the inner-sphere Tc complex was more negative than those for both type of outer-sphere Tc complexes on the surface of 14Å tobermorite mainly because only the inner-sphere TcO_4^- ion coordinated with the main structure of 14Å tobermorite; the inner-sphere Tc complex contained an Obts ion. The effect of the distance between the surface and the complexes on the adsorption energy was uncertain because different configurations of the complexes would also affect the adsorption energy.
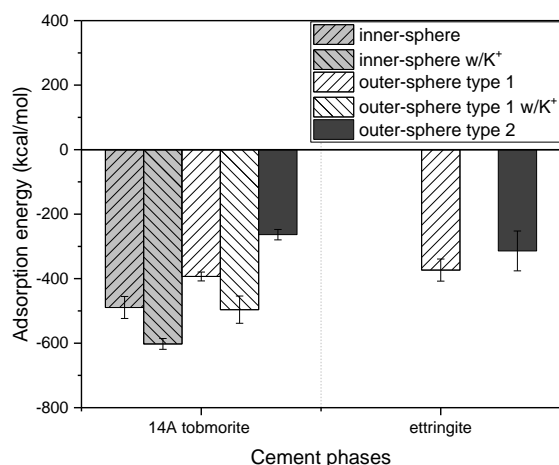
Figure 5.20. Adsorption energy between TcO_4^- ions and cement phases. Note: w/K^+ indicated with K^+ co-ion adsorption.

5.3.6 Dynamic Properties

The effect of interfacial interactions on the molecular mobility of the surface and bulk TcO_4^- ions was studied by using the diffusion coefficient calculated from the mean square displacement (MSD). In the bulk solution, TcO_4^- ions diffused three to four orders of magnitude faster than the surface species. The range of diffusion coefficients of the aqueous TcO_4^- ion (Figure 5.21) was comparable with other MD data (1.717×10^{-5} cm^2 s^{-1} [193]) and represented an underprediction of 17% compared to the experimental data of 1.950×10^{-5} cm^2 s^{-1} [194]. The inner-sphere TcO_4^- ions diffused one order of magnitude slower than the outer-sphere TcO_4^- ions on the surface of the 14Å tobermorite (Figure 5.21). Although there were two types of outer-sphere complexes on the surfaces of 14Å tobermorite and ettringite, the diffusion coefficients for the different types of complexes were comparable. Co-ion adsorption on the surface of 14Å tobermorite did not affect the dynamic properties of the inner-sphere and outer-sphere complexes. The large standard deviations for the diffusion coefficient of outer-sphere complexes on both the surface of 14Å tobermorite and ettringite were most likely due to the change of the configuration of outer-sphere complexes: the variation of amount of water molecules and Ca ions associated with TcO_4^- ions.
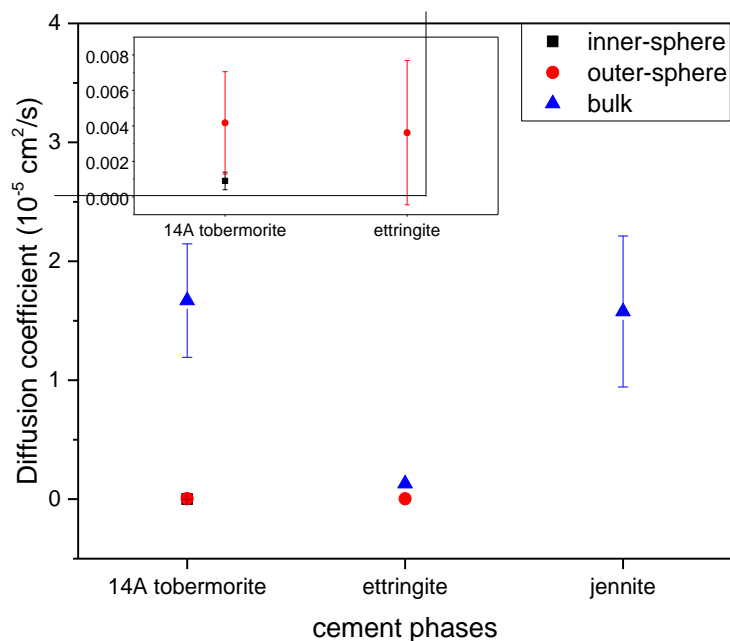
Figure 5.21. Diffusion coefficients of the inner-sphere and outer-sphere complexes and aqueous species in all the three models.

5.4   Conclusions

Molecular dynamics simulations were performed to study the molecular-scale energetic, structural, and dynamic properties of the interface between an aqueous solution containing 0.2M KTcO$_4$ and cement phases (14Å tobermorite, jennite, and ettringite). Results indicated the adsorption of TcO$_4^-$ ions on the octahedral CaO$_6$ surfaces of 14Å tobermorite and ettringite was energetically favorable, whereas no adsorption was observed on the octahedral CaO$_6$ surface of jennite.

On the octahedral CaO$_6$ surface of 14Å tobermorite, TcO$_4^-$ ions formed one type of inner-sphere and two types of outer-sphere Tc complexes (*i.e.* outer-sphere Tc complex type 1 with tetragonal geometry and outer-sphere Tc complex type 2 with tetrahedral geometry). The inner-sphere Tc complexes contained Obts, TcO$_4^-$, and Ca ions. Outer-sphere Tc complexes contained water molecules, TcO$_4^-$, and Ca ions. TcO$_4^-$ ions in the inner-sphere Tc complex and the outer-sphere Tc complex type 1 were in square pyramid geometry and were strongly polar. Co-ion adsorption mainly affected the configurations of Ca ions in these complexes. TcO$_4^-$ ions in the

outer-sphere Tc complex type 2 kept tetrahedral geometry. On the octahedral CaO_6 surface of ettringite, TcO_4^- ions only formed two types of outer-sphere Tc complexes consisting of water molecules, TcO_4^-, and Ca ions: outer-sphere Tc complex type 1 with square pyramid TcO_4^- ion and outer-sphere Tc complex type 2 with tetrahedral TcO_4^- ion. Dynamic properties indicated that surface TcO_4^- ions had much lower mobility than aqueous TcO_4^- ions: inner-sphere complexes diffused three to four orders slower than the aqueous species.

Interlayer or intercolumn Ca ions played an important role in the adsorption of TcO_4^- ions: TcO_4^- ions formed complexes with Ca ions; therefore, effective TcO_4^- ion immobilization on the surface of cement phases requires surface Ca ions remain at their original positions. The long-term performance of cementitious waste forms for TcO_4^- ions is, therefore, particularly challenged when subjected to calcium leaching [21].

CHAPTER 6

6   Summary and Perspective for Future Work

The goal of this research was to study the fundamental interaction mechanisms between ^{137}Cs, ^{99}Tc ions, and cementitious materials at the atomic scale. This chapter presents a summary of the results of the interactions between Cs^+ ions and crystalline C-S-H phases (9Å tobermorite, 14Å tobermorite, and jennite) as well as a summary of the results of the interactions between TcO_4^- ions and cement phases (14Å tobermorite, jennite, and ettringite). Further research is suggested based on the findings from this work.

6.1   Summary of Main Results

The present work yielded the following results for the interaction between Cs^+ ions and crystalline C-S-H phases (9Å tobermorite, 14Å tobermorite, and jennite):

- Cs^+ ions formed inner-sphere and outer-sphere complexes on the tetrahedral SiO_4 surface of crystalline C-S-H phases. The adsorption capacity decreased in the sequence of: 9Å tobermorite > 14Å tobermorite > jennite. Most adsorbed Cs^+ ions interacted with bridging O (Ob) on the SiO_4 surfaces to form inner-sphere complexes, in which one Cs^+ ion coordinated with about three Ob atoms.

- Inner-sphere adsorption of Cs^+ ions at the SiO_4 surface of 9Å tobermorite and 14Å tobermorite was energetically favorable while not favored at the SiO_4 surface of jennite. Inner-sphere Cs complexes diffused at a rate four orders of magnitude lower than aqueous Cs^+ ions, while outer-sphere Cs complexes were much mobile and diffused at a rate one order of magnitude lower than aqueous Cs^+ ions.

- Co-ion driven adsorption of Cs^+ ions was observed at the octahedral CaO_6 surfaces of all the three crystalline C-S-H phases. At the surfaces of tobermorite, inner-sphere adsorption was dominant over outer-sphere adsorption. Cs^+ ions adsorbed at the octahedral CaO_6 surfaces and interacted with Ob atoms, but coordinated with less Ob atoms than the inner-sphere Cs complexes at the tetrahedral SiO_4 surfaces.

- Water molecules showed a layered structure at the interface of 9Å tobermorite, 14Å tobermorite, and jennite at both the tetrahedral SiO_4 surface and the octahedral CaO_6 surfaces of all the three crystalline C-S-H phases. The dipole moments had preferred orientations up to 6Å above the SiO_4 surface of the 9Å tobermorite and 14Å tobermorite, whereas the dipole moments displayed a preferred orientation only up to 2Å above the tetrahedral SiO_4 surface of jennite.

MD simulations were used to study the interactions between TcO_4^- ions and cement phases (14Å tobermorite, jennite, and ettringite) and led to the following results:

- The adsorption of TcO_4^- ions on the octahedral CaO_6 surfaces of 14Å tobermorite and ettringite was energetically favorable, whereas no adsorption was observed on the octahedral CaO_6 surface of jennite. No adsorption was observed on the tetrahedral SiO_4 surface of 14Å tobermorite and jennite, or on the tetrahedral SO_4 surface of ettringite.
- On the surface of 14Å tobermorite, TcO_4^- ions formed one type of inner-sphere and two types of outer-sphere Tc complexes (*i.e.* outer-sphere Tc complex type 1 and outer-sphere Tc complex type 2). The inner-sphere Tc complexes contained bridging oxygen with tetrahedral substitution (Obts), TcO_4^-, and Ca^{2+} ions. Outer-sphere Tc complexes contained water molecules, TcO_4^-, and Ca^{2+} ions. TcO_4^- ions in the inner-sphere Tc complex and the outer-sphere Tc complex type 1 were in square pyramidal geometry and were strongly polar. Co-ion adsorption mainly affected the configurations of Ca^{2+} ions in these complexes. TcO_4^- ions in the outer-sphere Tc complex type 2 kept tetrahedral geometry.
- On the surface of ettringite, TcO_4^- ions formed two types of outer-sphere Tc complexes consisting of water molecules, TcO_4^-, and Ca^{2+} ions: outer-sphere Tc complex type 1 with square pyramidal TcO_4^- ion and outer-sphere Tc complex type 2 with tetrahedral TcO_4^- ion. The dynamic properties indicated that surface TcO_4^- ions had much lower mobility than aqueous TcO_4^- ions: inner-sphere complexes diffused three to four magnitudes slower than aqueous species.

6.2   Perspectives for Future Work

The present work applied short-term MD simulation (<20 ns) to investigate the energetic, dynamic, and structural properties at the interfaces between aqueous phases containing radionuclides and cement phases at the atomic scale. Although the present work provided fundamental knowledge about interaction mechanisms, the models applied need additional work to be applied to nuclear waste forms under field conditions. To design nuclear waste forms with better performance, the following factors should be considered in future research:

- Computational cells with larger sizes should be designed to accommodate more radionuclides at lower concentrations. The concentrations of solutions in the present work are higher than those found in the pore solutions of cementitious waste forms. Larger computational cells are required for models with more realistic concentrations, while maintaining enough ions in the solution to guarantee statistical reliability of the results.

- An amorphous realistic molecular model of cement hydrates is suggested to replace the crystalline C-S-H phases to study the interaction between radionuclides and the C-S-H [195]. In this case, a CLAYFF modified forcefield – CSHFF – might provide more accurate results [196].

- The cement pore solution contains a variety of ions including Na^+, K^+, Ca^{2+}, Mg^{2+}, Al^{3+}, Fe^{2+}, etc., to maintain ionic strengths in the range of 0.03-0.29M and pH-values in the range of 12.4-13.5 for fresh cement paste [197]. The pH-values of cement pore solution would be lower in long-term conditions due to aging, including carbonation [56]. The pH-value of a fully carbonated paste has been reported to be about 7 [198]. All these chemical properties should be included to design a more realistic model.

- MD simulations longer than 20ns are suggested to evaluate the long-term performance of cementitious materials, especially for the cementitious waste forms for TcO_4^- ions. Based on the results of the present work, Ca ions played an important role in the immobilization of TcO_4^- ions. Although most surface Ca ions stayed within inner-sphere and outer-sphere regions in the scope of present work, a complete decalcification might occur in long-term MD simulation and eventually desorb all the TcO_4^- ions. Further MD simulations could involve cement phases with different degrees of decalcification to study the effect of Ca leaching on the adsorption of TcO_4^- ions.

REFERENCES

[1]   D.A. Palmer, R.E. Meyer, Adsorption of technetium on selected inorganic ion-exchange materials and on a range of naturally occurring minerals under oxic conditions, J. Inorg. Nucl. Chem. 43 (1981) 2979–2984.

[2]   W. Lutze, R.C. Ewing, Radioactive waste forms for the future., New York, NY (USA); Elsevier Science Pub. Co., Inc., 1988.

[3]   A. Koning, R. Forrest, M. Kellett, The JEFF-3 . 1 . 1 Nuclear Data Library Organisation for Economic Co-operation and Development, 2006.

[4]   A.L. Nichols, D.L. Aldama, M. Verpelli, Handbook of Nuclear Data for Safeguards: Database Extensions, 2008.

[5]   W. Haynes, CRC handbook of chemistry and physics, 2014.

[6]   O.E. Omotoso, D.G. Ivey, R. Mikula, Containment mechanism of trivalent chromium in tricalcium silicate, J. Hazard. Mater. 60 (1998) 1–28.

[7]   F.P. Glasser, Characterization of the barrier performance of cements, Mater. Res. Soc. Symp. Proc. 713 (2002) 721–732.

[8]   S.Y. Hong, F.P. Glasser, Alkali sorption by C-S-H and C-A-S-H gels: Part II. Role of alumina, Cem. Concr. Res. 32 (2002) 1101–1111.

[9]   N. Evans, Binding mechanisms of radionuclides to cement, Cem. Concr. Res. 38 (2008) 543–553.

[10]   Y. Kim, R.T. Cygan, R.J. Kirkpatrick, 133Cs NMR and XPS investigation of cesium adsorbed on clay minerals and related phases, Geochim. Cosmochim. Acta. 60 (1996) 1041–1052.

[11]   Y. Kim, R. James Kirkpatrick, R.T. Cygan, 133Cs NMR study of cesium on the surfaces of kaolinite and illite, Geochim. Cosmochim. Acta. 60 (1996) 4059–4074.

[12]   S. Komarneni, D. Roy, C. Fyfe, G. Kennedy, Naturally occurring 1.4 nm tobermorite and synthetic jennite: Characterization by 27Al and 29Si MASNMR spectroscopy and cation

exchange properties, Cem. Concr. 17 (1987) 891–895.

[13] A.G. Kalinichev, R.J. Kirkpatrick, Molecular dynamics modeling of chloride binding to the surfaces of calcium hydroxide, hydrated calcium aluminate, and calcium silicate phases, Chem. Mater. 14 (2002) 3539–3549.

[14] M. Ochs, I. Pointeau, E. Giffaut, Caesium sorption by hydrated cement as a function of degradation state: Experiments and modelling, Waste Manag. 26 (2006) 725–732.

[15] S. Bagosi, L.J. Csetényi, Caesium immobilisation in hydrated calcium-silicate-aluminate systems, Cem. Concr. Res. 28 (1998) 1753–1759.

[16] K.G. Papadokostaki, A. Savidou, Study of leaching mechanisms of caesium ions incorporated in Ordinary Portland Cement, J. Hazard. Mater. 171 (2009) 1024–1031.

[17] H. Viallis, P. Faucon, J.C. Petit, a Nonat, Interaction between salts (NaCl, CsCl) and calcium silicate hydrates (C-S-H), J. Phys. Chem. B. 103 (1999) 5212–5219.

[18] I. Pointeau, N. Marmier, F. Fromage, M. FEdoroff, E. Giffaut, Cesium and lead uptake by CSH phases of hydrated cement, Mater. Res. Soc. 663 (2001).

[19] K. Noshita, T. Nishi, T. Yoshida, H. Fujihara, Categorization of cement hydrates by radionuclide sorption mechanism, MRS Online Proc. Libr. Arch. 663 (2000).

[20] S. Aggarwal, M.J. Angus, J. Ketchen, Sorption of radionuclides onto specific mineral phases present in repository cements, Rep. AEA Technol. NSS. 312 (2000) 1–64.

[21] K.N. V Adinarayana, P. Sasidhar, V. Balasubramaniyan, Modelling of calcium leaching and its influence on radionuclide migration across the concrete engineered barrier in a NSDF, J. Environ. Radioact. 124 (2013) 93–100.

[22] R.O. Abdel Rahman, D.H.A. Zin El Abidin, H. Abou-Shady, Cesium binding and leaching from single and binary contaminant cement-bentonite matrices, Chem. Eng. J. 245 (2014) 276–287.

[23] R.W. Crawford, C. McCulloch, M. Angus, F.P. Glasser, A.A. Rahman, Instrinsic sorption potential of cement components for 134Cs, Cem. Concr. Res. 14 (1984) 595–599.

[24]   R.O. Abdel Rahman, D.H.A. Zin El Abidin, H. Abou-Shady, Cesium binding and leaching from single and binary contaminant cement-bentonite matrices, Chem. Eng. J. 245 (2014) 276–287.

[25]   J. V. Hanna, L.P. Aldridge, E.R. Vance, Cs speciation in cements, Mater. Res. Soc. Symp. - Proc. 663 (2001) 89–96.

[26]   A. Atkinson, A.K. Nickerson, The diffusion of ions through water-saturated cement, J. Mater. Sci. 19 (1984) 3068–3078.

[27]   S. Komarneni, D.M. Roy, Tobermorites: A New Family of Cation Exchangers, Science (80-.). 221 (1983) 647–648.

[28]   M. Ochs, D. Mallants, L. Wang, Radionuclide and metal sorption on cement and concrete, Springer, 2006.

[29]   W.W. Lukens, J.J. Bucher, D.K. Shuh, N.M. Edelstein, Evolution of technetium speciation in reducing grout, Environ. Sci. Technol. 39 (2005) 8064–8070.

[30]   R.G. Allen, G.S. Siemerings, D.K. Shuh, J.J. Bucher, N.M. Edelstein, C.A. Langton, S.B. Clark, T. Reich, M.A. Denecke, Technetium Speciation in Cement Waste Forms Determined by X - ray Absorption Fine Structure Spectroscopy, Radiochim. Acta. 76 (1997) 77–86.

[31]   R. Druteikienė, J. Šapolaitė, Ž. Ežerinskis, L. Juodis, Batch-type study of Cs, Co, and Tc binding with hydrated cement under hyperalkaline conditions, J. Radioanal. Nucl. Chem. 313 (2017) 299–307.

[32]   J.J. Westsik, K. Cantrell, R. Serne, N. Qafoku, Technetium Immobilization Forms Literature Survey, 2014.

[33]   S. Bayliss, R. McCrohon, P. Oliver, N. Pilkington, H.P. Thomason, Near-Field Sorption Studies: January 1989 to June 1991., 1996.

[34]   S. Bayliss, A. Haworth, R. McCrohon, A.D. Moreton, P. Oliver, N.J. Pilkington, A.J. Smith, J.L. Smith-Briggs, Radioelement Behaviour in a Cementitious Environment, MRS Proc.

257 (1991) 641.

[35] D. Hou, Z. Li, Molecular Dynamics Study of Water and Ions Transported during the Nanopore Calcium Silicate Phase: Case Study of Jennite, J. Mater. Civ. Eng. 26 (2014) 930–940.

[36] A.G. Kalinichev, J. Wang, R.J. Kirkpatrick, Molecular dynamics modeling of the structure, dynamics and energetics of mineral-water interfaces: Application to cement materials, Cem. Concr. Res. 37 (2007) 337–347.

[37] M. Youssef, R.J.-M. Pellenq, B. Yildiz, Docking 90Sr radionuclide in cement: An atomistic modeling study, Phys. Chem. Earth. 70–71 (2014) 39–44.

[38] M. Nakano, K. Kawamura, Y. Ichikawa, Local structural information of Cs in smectite hydrates by means of an EXAFS study and molecular dynamics simulations, Appl. Clay Sci. 23 (2003) 15–23.

[39] N. Loganathan, A.O. Yazaydin, G.M. Bowers, A.G. Kalinichev, R.J. Kirkpatrick, Structure, energetics, and dynamics of Cs+ and H2O in hectorite: Molecular dynamics simulations with an unconstrained substrate surface, J. Phys. Chem. C. 120 (2016) 10298–10310.

[40] D.E. Smith, Molecular computer simulations of the swelling properties and interlayer structure of cesium montmorillonite, Langmuir. 14 (1998) 5959–5967.

[41] X. Liu, X. Lu, R. Wang, H. Zhou, Effects of layer-charge distribution on the thermodynamic and microscopic properties of Cs-smectite, Geochim. Cosmochim. Acta. 72 (2008) 1837–1847.

[42] G. Kosakowski, S. V. Churakov, T. Thoenen, Diffusion of Na and Cs in montmorillonite, Clays Clay Miner. 56 (2008) 190–206.

[43] R.F. Giese, Hydroxyl orientation in 2:1 phyllosilicates., Clays Clay Miner. 27 (1979) 213–223.

[44] C.D. Williams, P. Carbone, A classical force field for tetrahedral oxyanions developed using hydration properties: The examples of pertechnetate (TcO4-) and sulfate (SO42-), J. Chem.

Phys. 143 (2015) 174502.

[45] R.J. Serne, J.M. Zachara, D.S. Burke, Chemical Information on Tank Supernatants, Cs Adsorption From Tank Liquids Onto Hanford Sediments, and Field Observations of Cs Migration From Past Tank Leaks, 1998.

[46] K.R. Ashley, J.R. Ball, K.D. Abney, R. Turner, N.C. Schroeder, Breakthrough volumes of TcO_4- on Reillex^{TM}-HPQ anion exchange resin in a Hanford double shell tank simulant, J. Radioanal. Nucl. Chem. Artic. 194 (1995) 71–79.

[47] Radionuclide Basics: Cesium-137, www.epa.gov/radiation/radionuclide-basics- cesium-137.

[48] EPA Facts about Cesium-137, https://semspub.epa.gov/work/HQ/176308.pdf.

[49] R.L. Bunting, Nuclear data sheets for A = 137, Nucl. Data Sheets. 15 (1975) 335–369.

[50] A. Bunker, The ICRP Database of Dose Coefficients: Workers and Members of the Public, J. Radiol. Prot. 19 (1999) 290–290.

[51] Radionuclide Basics: Technetium-99, https://www.epa.gov/radiation/radionuclide-basics-technetium-99.

[52] I.S. Muller, D.A. McKeown, I.L. Pegg, Structural Behavior of Tc and I Ions in Nuclear Waste Glass, Procedia Mater. Sci. 7 (2014) 53–59.

[53] M. Garcia-Leon, 99Tc in the environment: Sources, distribution and methods, J. Nucl. Radiochem. Sci. 6 (2005) 253–259.

[54] J.D. Harrison, A. Phipps, Invited editorial: Gut transfer and doses from environmental technetium, J. Radiol. Prot. 21 (2001) 9–11.

[55] Disposal of technetium-99, http://large.stanford.edu/courses/2011/ph241/bhattacharyya2/.

[56] B. Lothenbach, K. Scrivener, R.D. Hooton, Supplementary cementitious materials, Cem. Concr. Res. 41 (2011) 1244–1256.

[57] K.L. Scrivener, A. Nonat, Hydration of cementitious materials, present and future, Cem.

Concr. Res. 41 (2011) 651–665.

[58]   I. Garcia-Lodeiro, A. Palomo, A. Fernández-Jiménez, D.E. MacPhee, Compatibility studies between N-A-S-H and C-A-S-H gels. Study in the ternary diagram Na2O-CaO-Al2O3-SiO2-H2O, Cem. Concr. Res. 41 (2011) 923–931.

[59]   H.F.W. Taylor, Cement chemistry, Cem. Concr. Compos. 20 (1998) 335.

[60]   L. Lam, Y.L. Wong, C.S. Poon, Degree of hydration and gel/space ratio of high-volume fly ash/cement systems, Cem. Concr. Res. 30 (2000) 747–756.

[61]   H.F.W. Taylor, Proposed structure for calcium silicate hydrate gel, J. Am. Ceram. Soc. 69 (1986) 464–467.

[62]   P. Hewlett, Lea's chemistry of cement and concrete, 4th ed., Elsevier, 2003.

[63]   J.J. Chen, J.J. Thomas, H.F.W. Taylor, H.M. Jennings, Solubility and structure of calcium silicate hydrate, Cem. Concr. Res. 34 (2004) 1499–1519.

[64]   P. Yu, R.J. Kirkpatrick, 35Cl NMR relaxation study of cement hydrate suspensions, Cem. Concr. Res. 31 (2001) 1479–1485.

[65]   P. Yu, R.J. Kirkpatrick, B. Poe, P.F. McMillan, X. Cong, Structure of calcium silicate hydrate (C-S-H): Near-, Mid-, and Far-infrared spectroscopy, J. Am. Ceram. Soc. 82 (2004) 742–748.

[66]   X. Cong, R.J. Kirkpatrick, 29Si MAS NMR study of the structure of calcium silicate hydrate, Adv. Cem. Based Mater. 3 (1996) 144–156.

[67]   X. Cong, R. James Kirkpatrick, 17O and29Si MAS NMR study of β-C2S hydration and the structure of calcium-silicate hydrates, Cem. Concr. Res. 23 (1993) 1065–1077.

[68]   I.G. Richardson, Nature of C-S-H in hardened cements, Cem. Concr. Res. 29 (1999) 1131–1147.

[69]   J.J. Thomas, H.M. Jennings, A.J. Allen, Relationships between composition and density of tobermorite, jennite, and nanoscale CaO-SiO2-H2O, J. Phys. Chem. C. 114 (2010) 7594–

7601.

[70] I.G. Richardson, The calcium silicate hydrates, Cem. Concr. Res. 38 (2008) 137–158.

[71] J.D. Bernal, J.W. Jeffery, H.F.W. Taylor, Crystallographic research on the hydration of Portland cement. A first report on investigations in progress, Mag. Concr. Res. 4 (1952) 49–54.

[72] H.D. Megaw, C.H. Kelsey, Crystal structure of tobermorite, Nature. 177 (1956) 390–391.

[73] H.F.W. Taylor, J.W. Howison, Relationships between calcium silicates and clay minerals, Clay Miner. Bull. 3 (1956) 98–111.

[74] D.L. Kantro, S. Brunauer, C.H. Weise, Development of surface in the hydration of calcium silicates. II. Extension of investigations to earlier and later stages of hydration, J. Phys. Chem. 66 (1962) 1804–1809.

[75] H.G. Kurczyk, H.E. Schwiete, Concerning the hydration products of C3S and β-C2S, Proc 4th Int. Symp. Chem. Cem. 1 (1962) 349–358.

[76] R.J. Kirkpatrick, J.L. Yarger, P.F. McMillan, Y. Ping, X. Cong, Raman spectroscopy of C-S-H, tobermorite, and jennite, Adv. Cem. Based Mater. 5 (1997) 93–99.

[77] A. V Girão, I.G. Richardson, C.B. Porteneuve, R.M.D. Brydson, Composition , morphology and nanostructure of C – S – H in white Portland cement pastes hydrated at 55 ° C, Cem. Concr. 37 (2007) 1571–1582.

[78] E. Bonaccorsi, S. Merlino, A.R. Kampf, The crystal structure of tobermorite 14 Å (plombierite), a C-S-H phase, J. Am. Ceram. Soc. 88 (2005) 505–512.

[79] E. Bonaccorsi, S. Merlino, H.F.W. Taylor, The crystal structure of jennite, Ca9Si6O18(OH)6·8H2O, Cem. Concr. Res. 34 (2004) 1481–1488.

[80] S. Merlino, E. Bonaccorsi, T. Armbruster, Tobermorites: Their real structure and order-disorder (OD) character, Am. Mineral. 84 (1999) 1613–1621.

[81] D.L. Cocke, The binding chemistry and leaching mechanisms of hazardous substances in

cementitious solidification/stabilization systems, J. Hazard. Mater. 24 (1990) 231–253.

[82] P.K. Mehta, Mechanism of sulfate attack on Portland cement, Cem. Concr. Res. 13 (1983) 401–406.

[83] P.K. Mehta, Concrete. Structure, properties and materials, 1986.

[84] A.E. Moore, H.F.W. Taylor, Crystal structure of ettringite, Acta Crystallogr. Sect. B Struct. Crystallogr. Cryst. Chem. 26 (1970) 386–393.

[85] S. V Mattigod, D.M. Wellman, C.C. Bovaird, K.E. Parker, K.P. Recknagle, L. Clayton, M.I. Wood, Diffusion of Radionuclides in Concrete and Soil, Radioact. Waste. 129 (2001) 20.

[86] C. Bucur, M. Olteanu, C. Cristache, M. Pavelescu, Radionuclide Transport through Cement Matrices, Rev. Chim. 61 (2010) 458–461.

[87] A.M. El-Kamash, A.M. El-Dakroury, H.F. Aly, Leaching kinetics of 137Cs and 60Co radionuclides fixed in cement and cement-based materials, Cem. Concr. Res. 32 (2002) 1797–1803.

[88] R.O. Abdel Rahman, A.A. Zaki, A.M. El-Kamash, Modeling the long-term leaching behavior of 137Cs, 60Co, and 152,154Eu radionuclides from cement-clay matrices, J. Hazard. Mater. 145 (2007) 372–380.

[89] A.M. El-Kamash, M.R. El-Naggar, M.I. El-Dessouky, Immobilization of cesium and strontium radionuclides in zeolite-cement blends, J. Hazard. Mater. 136 (2006) 310–316.

[90] R.O. Abdel Rahman, A.A. Zaki, Comparative study of leaching conceptual models: Cs leaching from different ILW cement based matrices, Chem. Eng. J. 173 (2011) 722–736.

[91] C.L. Kim, J.W. Park, J.Y. Kim, C.H. Chung, Improvement of nuclide leaching resistance of paraffin waste form with low density polyethylene, Waste Manag. 22 (2002) 625–630.

[92] American Nuclear Society Standards Committee, Measurement of the leachability of solidified low-level radioactive wastes by a short-term test procedure, American Nuclear Society La Grange Park, Illinois, USA, 1986.

[93] R.S. Iyer, J.A. Scott, Power station fly ash - A review of value-added utilization outside of the construction industry, Resour. Conserv. Recycl. 31 (2001) 217–228.

[94] D.M.R. Brew, F.P. Glasser, The magnesia-silica gel phase in slag cements: Alkali (K, Cs) sorption potential of synthetic gels, Cem. Concr. Res. 35 (2005) 77–83.

[95] C. Shi, A. Fernández-Jiménez, Stabilization/solidification of hazardous and radioactive wastes with alkali-activated cements, J. Hazard. Mater. 137 (2006) 1656–1663.

[96] P. Boch, M. Seiss, G. Vetter, M. Jacquin, High-alumina cements for cesium trapping, Cem. Concr. Res. 22 (1992) 369–374.

[97] X. Wu, S. Yen, X. Shen, M. Tang, Alkali-activated slag cement based radioactive waste forms, Cem. Concr. Res. 21 (1991) 16–20.

[98] S.L. Hoyle, M.W. Grutzeck, Incorporation of Cesium by Hydrating Calcium Aluminosilicates, J. Am. Ceram. Soc. 72 (1989) 1938–1947.

[99] G. Bar-Nes, A. Katz, Y. Peled, Y. Zeiri, The mechanism of cesium immobilization in densified silica-fume blended cement pastes, Cem. Concr. Res. 38 (2008) 667–674.

[100] P. Cronstrand, Assessment of uncertainty intervals for sorption coefficients, SKB Rapp. R-05-75. (2005).

[101] M.L.D. Gougar, B.E. Scheetz, D.M. Roy, Ettringite and C-S-H portland cement phases for waste ion immobilization: A review, Waste Manag. 16 (1996) 295–303.

[102] I.G. Richardson, G.W. Groves, The incorporation of minor and trace elements into calcium silicate hydrate (CSH) gel in hardened cement pastes, Cem. Concr. Res. 23 (1993) 131–138.

[103] B.I. Omel'yanenko, T.S. Livshits, S. V. Yudintsev, B.S. Nikonov, Natural and artificial minerals as matrices for immobilization of actinides, Geol. Ore Depos. 49 (2007) 173–193.

[104] Y. Kim, R. Kirkpatrick, 23Na and 133Cs NMR study of cation adsorption on mineral surfaces: Local environments, dynamics, and effects of mixed cations, Geochim. Cosmochim. Acta. 61 (1997) 5199–5208.

[105] O. Shrivastava, F. Glasser, Ion-exchange properties of 11-Å tobermorite, React. Solids. 2 (1986) 261–268.

[106] N. Labhsetwar, O. Shrivastava, Cation exchange studies on cement hydration phase: Ca5Si6O18H2· 4H2O, React. Solids. 7 (1989) 225–233.

[107] S. Komarneni, M. Tsuji, Selective cation exchange in substituted tobermorites, J. Am. Ceram. Soc. 72 (1989) 1668–1674.

[108] R. Guillaumont, T. Fanghanel, V. Neck, J. Fuger, D. a Palmer, I. Grenthe, M.H. Rand, Update on the chemical thermodynamics of uranium, neptunium, plutonium, americium and technetium, 2003.

[109] T.M. Gilliam, R.D. Spence, W.D. Bostick, J.L. Shoemaker, Solidification/stabilization of technetium in cement-based grouts, J. Hazard. Mater. 24 (1990) 189–197.

[110] L. De Windt, D. Pellegrini, J. van der Lee, Coupled modeling of cement/claystone interactions and radionuclide migration, J. Contam. Hydrol. 68 (2004) 165–182.

[111] F.P. Glasser, Mineralogical aspects of cement in radioactive waste disposal, Mineral. Mag. 65 (2001) 621–633.

[112] T. Gilliam, R. Spence, B. Evans-Brown, Performance testing of blast furnace slag for immobilization of technetium in grout, in: No. CONF-880903-17, Oak Ridge National Lab., TN (USA), 1988.

[113] S. V. Churakov, Structural position of H2O molecules and hydrogen bonding in anomalous 11Å tobermorite, Am. Mineral. 94 (2009) 156–165.

[114] P. Faucon, J.M. Delaye, J. Virlet, J.F. Jacquinot, F. Adenot, Study of the structural properties of the C-S-H(I) by molecular dynamics simulation, Cem. Concr. Res. 27 (1997) 1581–1590.

[115] P. Faucon, J.F. Jacquinot, J.M. Delaue, J. Virlet, Molecular dynamics simulation of Al3+ and Na+ substitutions in the tobermorite structure, Philos. Mag. Part B. 75 (1997) 769–783.

[116] P. Faucon, J.M. Delaye, J. Virlet, Molecular Dynamics Simulation of the Structure of

Calcium Silicate Hydrates: I. Ca4+xSi6O14+2x(OH)4−2x(H2O)2(0 ≤x≤ 1), J. Solid State Chem. 127 (1996) 92–97.

[117] M.J. Abdolhosseini Qomi, F.J. Ulm, R.J.-M. Pellenq, Evidence on the dual nature of aluminum in the calcium-silicate-hydrates based on atomistic simulations, J. Am. Ceram. Soc. 95 (2012) 1128–1137.

[118] H. Manzano, E. Masoero, I. Lopez-Arbeloa, H.M. Jennings, Shear deformations in calcium silicate hydrates, Soft Matter. 9 (2013) 7333.

[119] D. Hou, Z. Lu, T. Zhao, Q. Ding, Reactive molecular simulation on the ordered crystal and disordered glass of the calcium silicate hydrate gel, Ceram. Int. 42 (2016) 4333–4346.

[120] L. Liu, A. Jaramillo-Botero, W.A. Goddard, H. Sun, Development of a ReaxFF reactive force field for ettringite and study of its mechanical failure modes from reactive dynamics simulations, J. Phys. Chem. A. 116 (2012) 3918–3925.

[121] J.J. Thomas, H.M. Jennings, A.J. Allen, Relationships between composition and density of tobermorite, jennite, and nanoscale CaO-SiO2-H2O, J. Phys. Chem. C. 114 (2010) 7594–7601.

[122] D. Hou, T. Zhao, H. Ma, Z. Li, Reactive molecular simulation on water confined in the nanopores of the calcium silicate hydrate gel: Structure, Reactivity, and mechanical properties, J. Phys. Chem. C. 119 (2015) 1346–1358.

[123] J.P. Korb, P.J. McDonald, L. Monteilhet, A.G. Kalinichev, R.J. Kirkpatrick, Comparison of proton field-cycling relaxometry and molecular dynamics simulations for proton-water surface dynamics in cement-based materials, Cem. Concr. Res. 37 (2007) 348–350.

[124] D. Hou, Z. Li, Molecular dynamics study of water and ions transport in nano-pore of layered structure: A case study of tobermorite, Microporous Mesoporous Mater. 195 (2014) 9–20.

[125] A. Al-Ostaz, W. Wu, A.H.-D. Cheng, C.R. Song, A molecular dynamics and microporomechanics study on the mechanical properties of major constituents of hydrated cement, Compos. Part B Eng. 41 (2010) 543–549.

[126] R.T. Cygan, J.-J. Liang, A.G. Kalinichev, Molecular models of hydroxide, oxyhydroxide, and clay phases and the development of a general force field, J. Phys. Chem. B. 108 (2004) 1255–1266.

[127] L.N. Lammers, I.C. Bourg, M. Okumura, K. Kolluri, G. Sposito, M. Machida, Molecular dynamics simulations of cesium adsorption on illite nanoparticles, J. Colloid Interface Sci. 490 (2017) 608–620.

[128] V. Marry, B. Rotenberg, P. Turq, Structure and dynamics of water at a clay surface from molecular dynamics simulation, Phys. Chem. Chem. Phys. (2008).

[129] S.S. Lee, P. Fenter, K.L. Nagy, N.C. Sturchio, Monovalent ion adsorption at the muscovite (001)-solution interface: Relationships among ion coverage and speciation, interfacial water structure, and substrate relaxation, Langmuir. 28 (2012) 8637–8650.

[130] S. Hiroshi, Structure and dynamics of water on Li+ -, Na+ -, K+ -, Cs+ -, H3O+ -exchanged muscovite surfaces: A molecular dynamics study, Geochim. Cosmochim. Acta. 75 (2011) 63–81.

[131] S. Hajilar, B. Shafei, Mechanical failure mechanisms of hydrated products of tricalcium aluminate: A reactive molecular dynamics study, Mater. Des. 90 (2016) 165–176.

[132] P. V. Coveney, W. Humphries, Molecular modelling of the mechanism of action of phosphonate retarders on hydrating cements, J. Chem. Soc. Faraday Trans. 92 (1996) 831.

[133] M. Buhl, V. Golubnychiy, Binding of pertechnetate to uranyl(VI) in aqueous solution. A density functional theory molecular dynamics study, Inorg. Chem. 46 (2007) 8129–8131.

[134] R. Schurhammer, G. Wipff, Liquid-Liquid Extraction of Pertechnetic Acid (Tc VII) by Tri-n-butyl Phosphate: Where Is the Proton? A Molecular Dynamics Investigation, J. Phys. Chem. B. 115 (2011) 2338–2348.

[135] H. Cho, W.A. De Jong, B.K. McNamara, B.M. Rapko, I.E. Burgeson, Temperature and isotope substitution effects on the structure and NMR properties of the pertechnetate ion in water, J. Am. Chem. Soc. 126 (2004) 11583–11588.

[136] C.D. Williams, Simulating the Selective Adsorption of Pertechnetate to Oxyanion-SAMMS, University of Sheffield, 2014.

[137] Y. Marcus, The Properties of Solvents, Wiley, 1999.

[138] J. Wang, A.G. Kalinichev, R.J. Kirkpatrick, Effects of substrate structure and composition on the structure, dynamics, and energetics of water at mineral surfaces: A molecular dynamics modeling study, Geochim. Cosmochim. Acta. 70 (2006) 562–582.

[139] J. Wang, A.G. Kalinichev, R.J. Kirkpatrick, R.T. Cygan, Structure, energetics, and dynamics of water adsorbed on the muscovite (001) surface: A molecular dynamics simulation, J. Phys. Chem. B. 109 (2005) 15893–15905.

[140] J. Wang, A.G. Kalinichev, R.J. Kirkpatrick, Asymmetrie hydrogen bonding and orientational ordering of water at hydrophobic and hydrophilic surfaces: A comparison of water/vapor, water/talc, and water/mica interfaces, J. Phys. Chem. C. 113 (2009) 11077–11085.

[141] O. Söhnel, P. Novotný, Densities of aqueous solutions of inorganic substances, Elsevier Publishing Company, 1985.

[142] A. Grossfield, D.M. Zuckerman, Chapter 2 Quantifying Uncertainty and Sampling Quality in Biomolecular Simulations, Annu. Rep. Comput. Chem. 5 (2009) 23–48.

[143] L.J. Smith, X. Daura, W.F. van Gunsteren, Assessing equilibration and convergence in biomolecular simulations, Proteins Struct. Funct. Genet. 48 (2002) 487–496.

[144] E. Lyman, D.M. Zuckerman, Ensemble-Based Convergence Analysis of Biomolecular Trajectories, Biophys. J. 91 (2006) 164–172.

[145] B. Hess, Convergence of sampling in protein simulations, Phys. Rev. E - Stat. Physics, Plasmas, Fluids, Relat. Interdiscip. Top. 65 (2002) 31910.

[146] D. Peredo-Mancilla, H. Dominguez, Adsorption of phenol molecules by sodium dodecyl sulfate (SDS) surfactants deposited on solid surfaces: A computer simulation study, J. Mol. Graph. Model. 65 (2016) 108–112.

[147] M.H. Ghatee, M.M. Koleini, S. Ayatollahi, Molecular dynamics simulation investigation of hexanoic acid adsorption onto calcite (1014)surface, Fluid Phase Equilib. 387 (2015) 24–31.

[148] T. Le, A. Striolo, D.R. Cole, Propane simulated in silica pores: Adsorption isotherms, molecular structure, and mobility, Chem. Eng. Sci. 121 (2015) 292–299.

[149] R. Yaneva, S. Springer, M. Zacharias, Flexibility of the MHC class II peptide binding cleft in the bound, partially filled, and empty states: A molecular dynamics simulation study, Biopolymers. 91 (2009) 14–27.

[150] D. Garzón, P.J. Bond, J.D. Faraldo-Gómez, Predicted structural basis for CD1c presentation of mycobacterial branched polyketides and long lipopeptide antigens, Mol. Immunol. 47 (2009) 253–260.

[151] S.K. Sharma, G.D. Ko, K.J. Kang, High temperature creep and tensile properties of alumina formed on Fecralloy foils doped with yttrium, J. Eur. Ceram. Soc. 29 (2009) 355–362.

[152] G.A. Wells, I.B. Müller, C. Wrenger, A.I. Louw, The activity of Plasmodium falciparum arginase is mediated by a novel inter-monomer salt-bridge between Glu295-Arg404, FEBS J. 276 (2009) 3517–3530.

[153] E. Bismuto, E. Di Maggio, S. Pleus, M. Sikor, C. Rocker, G.U. Nienhaus, D.C. Lamb, Molecular dynamics simulation of the acidic compact state of apomyoglobin from yellowfin tuna, Proteins Struct. Funct. Bioinforma. 74 (2009) 273–290.

[154] J.A. Davis, D.B. Kent, Surface complexation modeling in aqueous geochemistry, Rev. Mineral. Geochemistry. 23 (1990) 177–260.

[155] J.F. Boily, P. Persson, S. Sjöberg, Benzenecarboxylate surface complexation at the goethite (α-FeOOH)/water interface: II. Linking IR spectroscopic observations to mechanistic surface complexation models for phthalate, trimellitate, and pyromellitate, Geochim. Cosmochim. Acta. 64 (2000) 3453–3470.

[156] R. Rahnemaie, T. Hiemstra, W.H. van Riemsdijk, Inner- and outer-sphere complexation of ions at the goethite-solution interface, J. Colloid Interface Sci. 297 (2006) 379–388.

[157] C.D. Lorenz, A. Travesset, Charge inversion of divalent ionic solutions in silica channels, Phys. Rev. E - Stat. Nonlinear, Soft Matter Phys. 75 (2007) 61202.

[158] I.C. Bourg, G. Sposito, Molecular dynamics simulations of the electrical double layer on smectite surfaces contacting concentrated mixed electrolyte (NaCl-CaCl2) solutions, J. Colloid Interface Sci. 360 (2011) 701–715.

[159] R.B. Schoch, J. Han, P. Renaud, Transport phenomena in nanofluidics, Rev. Mod. Phys. 80 (2008) 839–883.

[160] A.W. Adamson, Physical Chemistry of Surfaces, J. Electrochem. Soc. 124 (1977) 192C.

[161] M.H. Blees, Foundations of Colloid Science, Oxford University Press, 2002.

[162] J.O.M. Bockris, A.K. Reddy, Modern electrochemistry 2B: electrodics in chemistry, engineering, biology and environmental science, Springer Science & Business Media, 2001.

[163] A. Sridharan, P. V Satyamurty, Potential-distance relationships of clay-water systems considering the stern theory, Clays Clay Miner. 44 (1996) 479–484.

[164] H. Zhang, A.A. Hassanali, Y.K. Shin, C. Knight, S.J. Singer, The water-amorphous silica interface: Analysis of the Stern layer and surface conduction, J. Chem. Phys. 134 (2011) 24705.

[165] B. Rotenberg, V. Marry, N. Malikova, P. Turq, Molecular simulation of aqueous solutions at clay surfaces, J. Phys. Condens. Matter. 22 (2010) 284114.

[166] J.B. Hasted, D.M. Ritson, C.H. Collie, Dielectric properties of aqueous ionic solutions. Parts I and II, J. Chem. Phys. 16 (1948) 1–21.

[167] K. Nörtemann, J. Hilland, U. Kaatze, Dielectric properties of aqueous NaCl solutions at microwave frequencies, J. Phys. Chem. A. 101 (1997) 6864–6869.

[168] D.A. Sverjensky, Interpretation and prediction of triple-layer model capacitances and the structure of the oxide-electrolyte-water interface, Geochim. Cosmochim. Acta. 65 (2001) 3643–3655.

[169] I.F. Vasconcelos, B.A. Bunker, R.T. Cygan, Molecular Dynamics Modeling of Ion Adsorption to the Basal Surfaces of Kaolinite, J. Phys. Chem. C. 111 (2007) 6753–6762.

[170] F.P. Glasser, Progress in the immobilization of radioactive wastes in cement, Cem. Concr. Res. 22 (1992) 201–216.

[171] J.J. Beaudoin, L. Raki, R. Alizadeh, A 29Si MAS NMR study of modified C-S-H nanostructures, Cem. Concr. Compos. 31 (2009) 585–590.

[172] A.R. Brough, C.M. Dobson, I.G. Richardson, G.W. Groves, In situ solid-state NMR studies of Ca3SiO5: hydration at room temperature and at elevated temperatures using 29Si enrichment, J. Mater. Sci. 29 (1994) 3926–3940.

[173] X. Cong, R.J. Kirkpatrick, 17O MAS NMR investigation of the structure of calcium silicate hydrate gel, J. Am. Ceram. Soc. 79 (1996) 1585–1592.

[174] D. Hou, Z. Li, T. Zhao, P. Zhang, Water transport in the nano-pore of the calcium silicate phase: reactivity, structure and dynamics, Phys. Chem. Chem. Phys. 17 (2015) 1411–1423.

[175] P.A. Bonnaud, B. Coasne, R.J.-M. Pellenq, Molecular simulation of water confined in nanoporous silica, J. Phys. Condens. Matter. 22 (2010) 284110.

[176] B. Rotenberg, V. Marry, R. Vuilleumier, N. Malikova, C. Simon, P. Turq, Water and ions in clays: Unraveling the interlayer/micropore exchange using molecular dynamics, Geochim. Cosmochim. Acta. 71 (2007) 5089–5101.

[177] H. Ohtaki, T. Radnai, Structure and Dynamics of Hydrated Ions, Chem. Rev. 93 (1993) 1157–1204.

[178] H. Sato, M. Yui, H. Yoshikawa, Ionic Diffusion Coefficients of Cs+, Pb2+, Sm3+, Ni2+, SeO2-4and TcO−4in Free Water Determined from Conductivity Measurements, J. Nucl. Sci. Technol. 33 (1996) 950–955.

[179] J. Icenhower, N. Qafoku, W. Martin, J.M. Zachara, The Geochemistry of Technetium: a summary of the Behavior of an Artificial Element in the Natural Environment, Pacific Northwest National Laboratory (PNNL), Richland, WA (US), 2008.

[180] G.S. Barger, J. Bayles, B. Blair, D. Brown, H. Chen, T. Conway, P. Hawkins, Ettringite formation and the performance of concrete, Portl. Cem. Assoc. (2001) 1–16.

[181] F.N. Skomurski, K.M. Rosso, K.M. Krupka, B.P. McGrail, Technetium incorporation into hematite (α-Fe2O3), Environ. Sci. Technol. 44 (2010) 5855–5861.

[182] H. Vinsova, R. Konirova, M. Koudelkova, V. Jedinakova-Krizova, Sorption of technetium and rhenium on natural sorbents under aerobic conditions, J. Radioanal. Nucl. Chem. 261 (2004) 407–413.

[183] J.J. Westsik, K. Cantrell, R. Serne, N. Qafoku, Technetium Immobilization Forms Literature Survey, (2014) PNNL-23329.

[184] J.Y. Li, W. Dai, G.P. Xiao, H. Wang, Z.T. Zhang, T. Wu, Pertechnetate diffusion in GMZ bentonite, J. Radioanal. Nucl. Chem. 293 (2012) 763–767.

[185] D. Cui, T.E. Eriksen, Reduction of pertechnetate in solution by heterogeneous electron transfer from Fe(II)-containing geological material, Environ. Sci. Technol. 30 (1996) 2263–2269.

[186] C.L. Thorpe, C. Boothman, J.R. Lloyd, G.T.W. Law, N.D. Bryan, N. Atherton, F.R. Livens, K. Morris, The interactions of strontium and technetium with Fe(II) bearing biominerals: Implications for bioremediation of radioactively contaminated land, Appl. Geochemistry. 40 (2014) 135–143.

[187] D. Fan, R.P. Anitori, B.M. Tebo, P.G. Tratnyek, J.S.L. Pacheco, R.K. Kukkadapu, M.H. Engelhard, M.E. Bowden, L. Kovarik, B.W. Arey, Reductive sequestration of pertechnetate (99TcO4-) by nano zerovalent iron (nZVI) transformed by abiotic sulfide, Environ. Sci. Technol. 47 (2013) 5302–5310.

[188] S. Mindess, J.F. Young, D. Darwin, Concrete, Prentice Hall, 2003.

[189] X. Xu, A.G. Kalinichev, R. James Kirkpatrick, 133Cs and 35Cl NMR spectroscopy and molecular dynamics modeling of Cs+ and Cl- complexation with natural organic matter, Geochim. Cosmochim. Acta. 70 (2006) 4319–4331.

[190] C.D. Williams, N. a Burton, K.P. Travis, J.H. Harding, The development of a classical force field to determine the selectivity of an aqueous Fe3+-EDA complex for TcO4- and SO42-, J. Chem. Theory Comput. 10 (2014) 3345–3353.

[191] C.J.M. Huige, C. Altona, Force field parameters for sulfates and sulfamates based on ab initio calculations: Extensions of AMBER and CHARMm fields, J. Comput. Chem. 16 (1995) 56–79.

[192] Y. Marcus, Concentration dependence of ionic hydration numbers, J. Phys. Chem. B. 118 (2014) 10471–10476.

[193] C.D. Williams, P. Carbone, A classical force field for tetrahedral oxyanions developed using hydration properties: The examples of pertechnetate (TcO4-) and sulfate (SO42-), J. Chem. Phys. 143 (2015) 174502–174502.

[194] H. SATO, M. YUI, H. YOSHIKAWA, Ionic Diffusion Coefficients of Cs + , Pb 2+ , Sm 3+ , Ni 2+ , SeO 2- 4 and TcO − 4 in Free Water Determined from Conductivity Measurements, J. Nucl. Sci. Technol. 33 (1996) 950–955.

[195] R.J.-M. Pellenq, A. Kushima, R. Shahsavari, K.J. Van Vliet, M.J. Buehler, S. Yip, F.-J. Ulm, A realistic molecular model of cement hydrates, Proc. Natl. Acad. Sci. 106 (2009) 16102–16107.

[196] R. Shahsavari, R.J.-M. Pellenq, F.-J. Ulm, Empirical force fields for complex hydrated calcio-silicate layered materials, Phys. Chem. Chem. Phys. 13 (2011) 1002–1011.

[197] K. Andersson, B. Allard, M. Bengtsson, B. Magnusson, Chemical composition of cement pore solutions, Cem. Concr. Res. 19 (1989) 327–332.

[198] H. Cui, W. Tang, W. Liu, Z. Dong, F. Xing, Experimental study on effects of CO2 concentrations on concrete carbonation and diffusion mechanisms, Constr. Build. Mater. 93 (2015) 522–527.

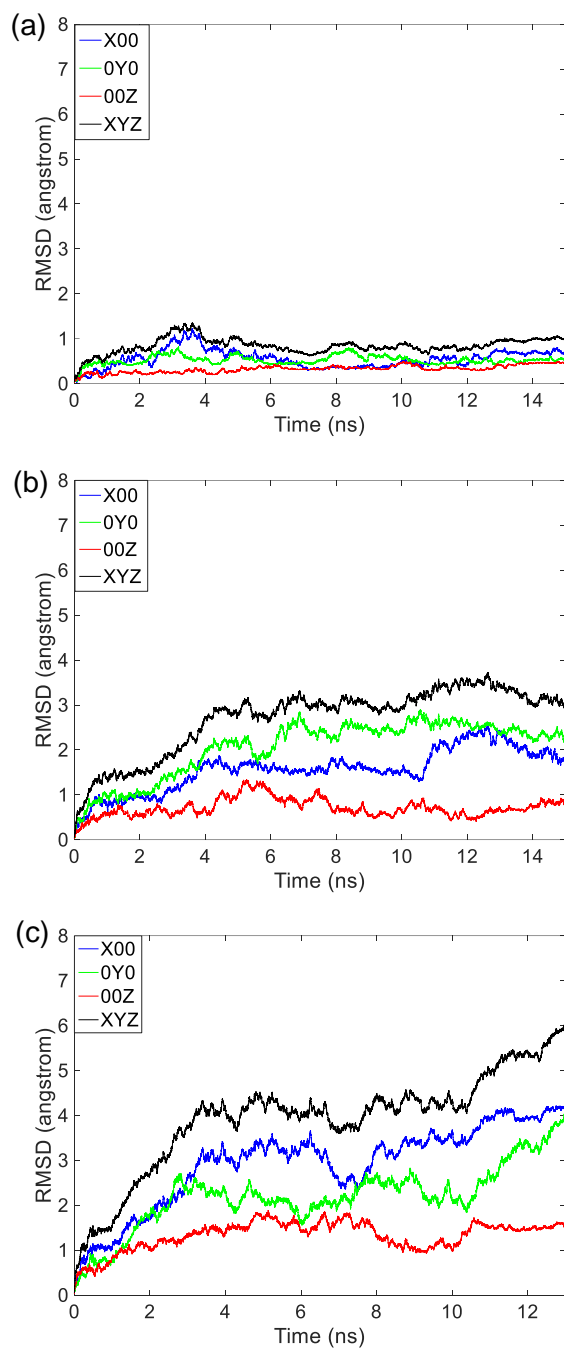SUPPLEMENTARY MATERIALS FOR CHAPTER 3

Figure A.1. RMSD of Cl$^-$ ions and the atoms of first layer on the octahedral CaO$_6$ surfaces of: (a) 9Å tobermorite, (b) 14Å tobermorite, and (c) jennite.

Table A.1. The duration when Cs^+ ions adsorbed as stable inner-sphere complexes and outer-sphere complexes on the tetrahedral SiO_4 surface of 14Å tobermorite and diffuse ions in the bulk solution.

Cs^+ ions index	Inner-sphere period (frame number, >5000 frames)	Outer-sphere period (frame number, ~2500 frames)	Diffuse ion (frame number, >5000 frames)
Z1	77544-83894(0.6ns), 83899-91226(0.7ns), 140052-150001(0.9ns)	120000-123000(~0.3ns), 132000-135000(~0.3ns)	N/A
Z2	N/A	N/A	143062-150001(0.6ns)
Z3	109014-143452(3.4ns)	91000-93500(~0.25ns), 96000-99000(~0.30ns)	70000-80456(1.0ns)
Z4	78318-85558(0.7ns), 85717-91122(0.5ns), 91124-110523(1.9ns), 110527-118162(0.7ns)	136000-138500(~0.25ns), 139500-142000(~0.25ns)	N/A
Z5	130082-135102(0.5ns), 135963-141240(0.5ns)	N/A	70000-75763(0.5ns), 85109-128290(4.3ns)
Z6	80690-85240(0.5ns), 89067-94929(0.5ns)	N/A	139562-150001(1.0ns)
Z7	N/A	104000-107000(~0.30ns), 119500-122000(~0.25ns)	131250-145920(1.4ns)
Z8	N/A	70000-73000(~0.30ns), 127000-130500(~0.25ns)	73189-79523(0.6ns), 98886-110083(1.1ns)
Z9	109763-116616(0.6ns), 118659-129852(1.1ns)	131000-134000(~0.30ns) 145000-148000(~0.30ns)	76532-89051(1.2ns)

N/A: not available

Table A.2. The duration when TcO_4^- ions adsorbed as stable inner-sphere complexes and outer-sphere complexes on the surface of 14Å tobermorite and diffuse ions in the bulk solution.

TcO_4^- ions index	Inner-sphere period (frame number, >5000 frames)	Outer-sphere period (frame number, ~2500 frames)	Diffuse ion (frame number, >5000 frames)
Z1	140000-200001 (6ns)	N/A	N/A
Z2	N/A	174958-200001 (2.5ns)	140000-174563 (3.4ns)
Z3	N/A	N/A	140000-147634 (0.7ns), 149563-200001 (5ns)
Z4	N/A	140000-156109 (1.6ns), 163157-200001 (3.6ns)	N/A

Table A.3. The duration when TcO$_4^-$ ions adsorbed as stable inner-sphere complexes and outer-sphere complexes on the surface of 14Å tobermorite and diffuse ions in the bulk solution.

| TcO$_4^-$ ions index	Inner-sphere period (frame number, >5000 frames)	Outer-sphere period (frame number, ~2500 frames)	Diffuse ion (frame number, >5000 frames)
Z1	N/A	140000-147956 (0.7ns), 148069-200001 (5.2ns)	N/A
Z2	N/A	140000-174869 (3.4ns), 183769-193241 (0.9ns), 193267-200001 (0.6ns)	N/A
Z3	N/A	140000-148921 (0.8ns), 162014-200001 (3.7ns)	N/A
Z4	N/A	140000-200001 (6ns)	N/A
Z5	N/A	140000-200001 (6ns)	N/A

SUPPLEMENTARY MATERIALS FOR CHAPTER 4
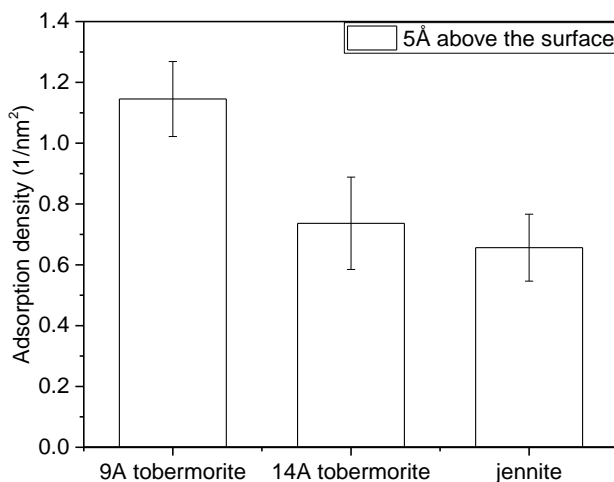
Figure B.1. Adsorption density of Cl^- ion up to 5Å above the octahedral CaO_6 surfaces.

Table B.1. The adsorption density of Cl^- and Cs^+ ions 5Å above the octahedral CaO_6 surfaces.

		Total adsorbed Cl			Total adsorbed Cs		
	Ntot	Nad	ρ $(1/nm^2)$	Xad (%)	Nad	ρ $(1/nm^2)$	Xad
9Å tobermorite	12	7.43	1.15	61.9	1.26	0.19	10.54
14Å tobermorite	9	3.63	0.74	40.3	0.48	0.10	5.28
jennite	11	4.33	0.66	39.4	0.65	0.10	5.93

Ntot: total number of Cs^+ or Cl^- ions in the system. Nad: total number of Cs^+ or Cl^- ions adsorbed in the inner-sphere region. Xad: percentage of the Cs^+ or Cl^- ions adsorbed. ρ: adsorption density.